HAL
open science

Design of magnetic probes for near field measurements and the development of algorithms for the prediction of EMC

Nimisha Sivaraman

To cite this version:

Nimisha Sivaraman. Design of magnetic probes for near field measurements and the development of algorithms for the prediction of EMC. Optics / Photonic. Université Grenoble Alpes, 2017. English. NNT : 2017GREAT082 . tel-01757038

HAL Id: tel-01757038

https://theses.hal.science/tel-01757038v1

Submitted on 3 Apr 2018

HAL is a multi-disciplinary open access archive for the deposit and dissemination of scientific research documents, whether they are published or not. The documents may come from teaching and research institutions in France or abroad, or from public or private research centers.

L'archive ouverte pluridisciplinaire **HAL**, est destinée au dépôt et à la diffusion de documents scientifiques de niveau recherche, publiés ou non, émanant des établissements d'enseignement et de recherche français ou étrangers, des laboratoires publics ou privés.

Communauté UNIVERSITÉ Grenoble Alpes

THÈSE

Pour obtenir le grade de

DOCTEUR DE LA COMMUNAUTÉ UNIVERSITÉ GRENOBLE ALPES

Spécialité : **Optique et Radiofréquences**

Arrêté ministériel : 7 août 2006

Présentée par

Nimisha SIVARAMAN

Thèse dirigée par **Fabien NDAGIJIMANA, Professeur, Université Grenoble Alpes**

préparée au sein du **Laboratoire IMEP-LAHC**
dans**l'École Doctorale Électronique, Électrotechnique, Automatique et Traitement du signal (EEATS)**

Design of magnetic probes for near-field measurements and the development of algorithms for the prediction of EMC

Thèse soutenue publiquement le **5 décembre 2017**,devant le jury composé de :

Mme. Daniela DRAGOMIRESCU
Professeur,INSA Toulouse, Rapporteur
M. Eduardo MOTTA CRUZ
Professeur, Ecole polytechnique de Nantes, Rapporteur
M. Christian VOLLAIRE
Professeur, Ecole Centrale de Lyon, Président
M. Sébastien SERPAUD
Ingénieur, Toulouse, Examinateur
M. Leonce MUTEL
Ingénieur, Valence, Examinateur
M. Fabien NDAGIJIMANA
Professeur, Université Grenoble Alpes, Directeur de thèse
M. Zouheir RIAH
Enseignant-chercheur,IRSEEM-ESIGELEC, Rouen, Invité

Abstract

As the number of components in a confined volume is increasing, there is a strong demand for identifying the sources of radiation in PCBs and the prediction of EMC of electronic circuits. Electromagnetic near field scanning is a general method of identifying the radiating sources in a PCB. The first part of the thesis consists of the design and characterization of printed circuit magnetic probes with high sensitivity and high spatial resolution. Conventional probes based on microstrip and coplanar configuration is studied. As the length of the transmission line connected to the probe increases, the probe output contains noise due to common mode voltages which is many induced by the electric field. In order to suppress the voltage induced due to the electric field, a shielded magnetic probe is designed and fabricated using low cost printed circuit board (PCB) technology. The performance of the passive probe is calibrated and validated from 1MHz – 1GHz. The shielded probe is fabricated on an FR4 substrate of thickness 0.8mm and consists of 3 layers with the signal in the middle layer and top and bottom layers dedicated to ground planes. The aperture size of the loop is 800µm x 800µm, with an expected spatial resolution of 400 µm. The high sensitivity of the probe is achieved by integrating a low noise amplifier at the output of the probe, hence making an active probe. The performance of the shielded probe with a different length of transmission lines is made to study. When the probe has to be operated above 100MHz, it is found that the transmission lines connected to the probe should be short (around 1.5cm). For frequencies below 100MH, the length of the lines can be up to 12cm. A three-axis probe which is able to measure the three components of the magnetic field is also designed and validated by near field scanning above a standard wire over the ground structure.

In The second part, the inverse transmission line matrix method (Inv-TLM) method is used reconstruct the source distribution from the near field scan (NFS) data above a single in plane on the PCB. Even though the resolution of reconstruction depends on the wavelength and the mesh parameter, the inverse propagation increases the width of the reconstructed wave. As this method is found to be ill posed and results in multiple solutions, we have developed a new method based on the two-dimensional cross-correlation, which represents the near field scan data in terms of the equivalent electric currents of the dipole. With the new method, we are able to identify and locate the current sources in the PCB and are represented by an equivalent source. The method is validated for the current sources with different orientations. The simulated near field data using CST microwave studio is used to validate both the methods. The radiated far field from these equivalent sources is compared with the simulated fields.

Keywords: *2-D cross-correlation method, Electromagnetic compatibility, near field scanning, shielded magnetic probe, source reconstruction, Transmission line matrix method*

List of abbreviations

EMC	Electromagnetic compatibility
DUT	Device Under Test
PCB	Printed Circuit Board
AF	Antenna Factor
TLM	Transmission Line Matrix
EMI	Electromagnetic Interference
RFI	Radio frequency Interference
EMP	Electro Magnetic Pulse
NFS	Near Field Scan
NFPs	Near Field Probe
EO	Electro optical
FDTD	Finite Difference Time Domain Method
MoM	Method of Moments
UCSA	Uniform Circular Scatterer Array
ESD	Electro static Discharge
IC	Integrated Circuit
MST	Modulated Scattering Technique
LTCC	Low Temperature Co fired Ceramic
CMOS	Complementary metal oxide semi-conductor
SoI	Silicon on Insulator
LNA	Low Noise Amplifier
SWE	Spherical Wave Expansion
NF	Near field
FF	Far Field
AUT	Antenna Under Test
TRM	Time Reversal Mirror

Contents

Abstract iii

List of abbreviations iv

1. Introduction 9

1.1 Need of EMC in electronic components 9

1.2 Measurement methods of PCB emissions 12

1.3 Near field measurements 16

1.3.1 Near field and far field 16

1.3.2 Why near field measurements? 16

1.4 Objective of the thesis 17

1.5 References 19

2. State of the art 21

2.1 Near Field Probes 21

2.1.1 Electro-optical probes 21

2.1.2 Electromagnetic probes 22

2.2 Synthesis of radiating sources 28

2.3 Conclusion 31

2.4 References 33

3. Design and characterization of printed circuit magnetic probes 36

3.1 Introduction 36

3.2 Parameters of the probe 36

3.3 The near field test bench 37

Reference circuit 39

3.4 Printed magnetic field probes 41

3.5 Printed circuit probes type 1 (with microstrip line) 42

3.5.1 Simulation model 43

3.5.2 Simulated results 44

3.5.3 Effect of the structure of loop 45

3.5.4 Effect of the transmission line 47

3.5.5 Characterization of microstrip probes 49

3.6 Printed circuit probes type 2 (with CPW line) 50
3.6.1 Coplanar waveguide (CPW) design 50
3.6.2 Grounded coplanar waveguide (GCPW) design 51
3.6.3 Design of coplanar probes 52
3.6.4 Characterization 53
3.7 Response of the loop to currents and voltages on the trace 54
3.8 Miniaturized Shielded magnetic probe 56
3.8.1 Design of the shielded probe 56
3.8.2 Equivalent circuit model 59
3.8.3 Characterization 60
3.8.4 Effect of the length of the probe and arm of the measurement system 66
3.9 Design and characterization of 3 axis magnetic field probes 69
3.9.1 Design and characterization 69
3.10 Active magnetic probes 73
3.10.1 Design of active probe 74
3.10.2 Characterization 75
3.10.3 Positioning of the amplifier on the active probe 76
3.11 Conclusion 79
3.12 References 80
4. Source reconstruction methods for the prediction of EMC 83
4.1 Introduction 83
4.2 EM source reconstruction using inverse- TLM method 83
4.2.1 Time reversal- an overview 83
4.2.2 Transmission line matrix (TLM) method 85
4.2.3 Inverse TLM method 88
4.2.4 EM source synthesis with reverse TLM method- state of the art 90
4.3 Equivalent source from near field data using Inverse TLM Method 93
4.3.1 Excitation signal 93
4.3.2 Reconstruction of ideal sources 94
4.3.3 Effect of near field scanning height on source reconstruction 101
4.3.4 Spatial resolution 102
4.3.5 Application of frequency domain NFS data to time domain TLM method 104
4.3.6 Calculation of equivalent source 106
4.3.7 Limitations of source reconstruction using Inverse TLM method 109
4.4 Equivalent source by 2D cross-correlation method 110
4.4.1 2 D cross-correlation method 110
4.4.2 Formulation of the equations 111
4.4.3 Algorithm for finding the equivalent source 113

4.4.4 Validation by application to elementary currents 114
4.4.5 Application to PCBs on air 123
4.5 Prediction of the radiated field 125
4.5.1 Far field integral 125
4.5.2 Radiation from monopole 127
4.5.3 Predicted field of bend monopole 128
4.6 Conclusions 128
4.7 References 130
5. Conclusions and perspectives 133
APPENDIX 137
References 140
List of publications 141
Résumé 143

1. Introduction

1.1 Need of EMC in electronic components

The widespread use of electronic circuits for communication, computation, automation etc. makes it necessary for different electronic circuits to operate in close proximity to each other. Quite often, these circuits affect each other adversely. Electromagnetic interference (EMI) has become a major problem for circuit designers, and it is likely to become even more severe in the future. A large number of electronic devices in common use is partly responsible for this trend. In addition, the use of integrated circuits and largescale integration has reduced the size of electronic equipment. As electronic circuits have become smaller and more sophisticated, more circuits are being confined into less space, which increases the probability of interference. The products must be designed to work in the ‘‘real world,’’ with other equipment nearby, and to comply with the electromagnetic compatibility (EMC) regulations. On the other hand, the equipment should not be affected by external electromagnetic sources and should not itself be a source of electromagnetic noise that can pollute the environment. In an electronic system the most common sources of radio frequency interference (RFI) can be listed as below:

(1) The electromagnetic spectrum that is used extensively by radio transmitters for communications

(2) High frequency pulses trains in digital systems

(3) Intended high frequency oscillator circuits used in sub-systems

(4) Circuit transients caused by simple switching operations

In digital circuit design, EMC gathers attention because of the three different technological trends. First, in the process of achieving higher processing speeds, shorter pulse rise-times are used, contributing a significant amount of energy at high frequencies, which is capable of propagating by radiative mechanisms over long distances. Second, the modern physical design of equipment is based increasingly on the use of plastics in preference to metals. This significantly reduces the electromagnetic shielding inherent to the all-metal cabinet. The third one is due to the trend for compact design as a result of miniaturization, which in turn contributes to EMC problems.

Electromagnetic compatibility (EMC) is the ability of an electronic system to (1) function properly in its intended electromagnetic environment and (2) not be a source of pollution to that electromagnetic environment. The electromagnetic environment is composed of both radiated and conducted energy. EMC, therefore, has two aspects, emission, and susceptibility. Susceptibility is the capability of a device or circuit to respond to unwanted electromagnetic energy (i.e., noise). The opposite of susceptibility is radiation. The immunity level of a circuit or device is the electromagnetic environment in which the equipment can operate satisfactorily, without degradation, and with a defined margin of safety. One difficulty in determining immunity (or susceptibility) levels is defining what constitutes performance degradation. Emission pertains to the interference-causing potential of a product. The purpose of controlling emissions is to limit the electromagnetic energy emitted and thereby to control the electromagnetic environment in which other products must operate. The three aspects, which forms the basic framework of EMC design is the generation, transmission, and reception of electromagnetic energy (shown in Figure 1-1). Whether the source or receptor is intended or unintended depends on the type of the coupling path and the source or receiver.

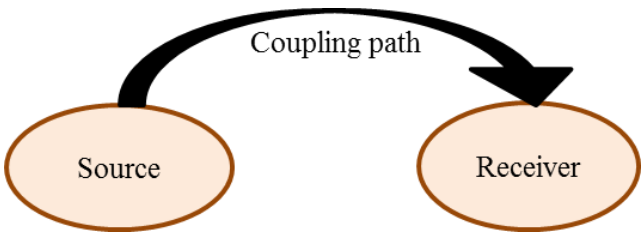

Figure 1-1 Universal interference model

The transfer of electromagnetic energy can be divided into four subgroups, radiated emissions, radiated susceptibility, conducted emissions and conducted susceptibility. These four aspects are shown in Figure 1-2[1]. An electronic system normally consists of one or more subsystems that communicate each other via cables. These cables have the potential in emitting or picking up the electromagnetic energy. Longer the length of the cable, the more efficient it is in picking up or emitting the electromagnetic radiations. The factor that produces intended or unintended radiation is the currents on the cables or traces. Electromagnetic emission or susceptibility to emission not only occurs by radiation through the air, but also interference signals passes between the subsystems directly via conduction. There are also some other factors concerned with the EMC. Some of them are depicted in Figure 1-3[2]. There is significant interest in the military in hardening the communication against the electromagnetic pulse (EMP). The electromagnetic interference from the intense current caused by lightning couples to the electronic power systems and subsequently it is conducted into the device through the ac power cord. There are instances of direct interception with

the radiated emissions from which the content of the communication can be determined. This problem is called TEMPSET and is imperative for the military.

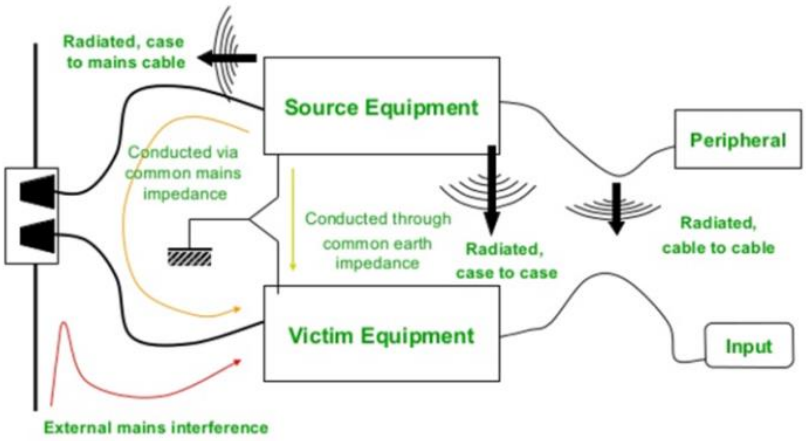

Figure 1-2 Emission and susceptibility in an electronic system[1]

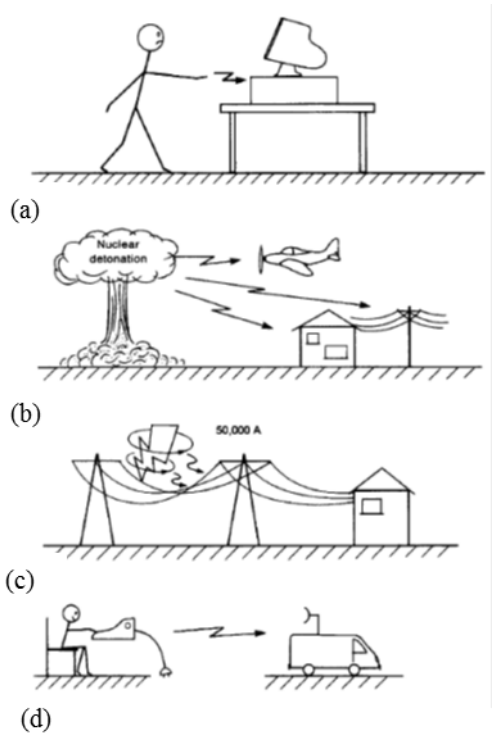

Figure 1-3 Some other aspects of EMC (a) Electro Static Discharge , ESD (b) electromagnetic pulse, EMP (c) lightning (d) TEMPEST (secure communication and data processing) [2]

Controlling the emission from one product may eliminate an interference problem for many other products. Therefore, it is desirable to control emission in an attempt to produce an electromagnetically compatible environment.

There are two different approaches to predict the emission or immunity of an electronic circuit, analytical and numerical methods. However the analytical methods can be applied only to very simplified structure, they are still important as they provide insight into the significance of various

parameters and also benchmarks against which numerical methods can be checked and evaluated. For more complex configurations, numerical computer-based methods are suitable for studying the behavior of the system. The numerical methods are mainly classified into two groups:

(1) Frequency-domain methods such as the finite element method (FEM) and the method of moments (MOM).
(2) Time-domain methods such as the finite-difference-time-domain (FD-TD) method and the transmission line matrix (TLM) method.

In another classification the numerical methods are divided into following groups:

(1) Integral equation methods and
(2) Differential equation methods

1.2 Measurement methods of PCB emissions

The electromagnetic emissions from a PCB can be classified as conducted emissions and radiated emissions or common mode and differential mode emissions. The conducted emission measurements are either a voltage-capacitive-tap type of measurement or they are a current-clamp type of measurement. On the other hand, the radiated emission measurements are unique in that they must always state "the horizontal distance from the Device-under-Test (DUT) to the receiving antenna." This horizontal distance can be 1.5,5,10 or 30 meters[3].

TEM cell method: The radiation level of a device under test can be measured using a TEM cell as shown in Figure 1-4[4]. The DUT faces the interior of the cell while the support circuitry is maintained outside the cell. The RF voltage appearing at the input of the connected spectrum analyzer is related to the electromagnetic potential of the DUT. The measurements are repeated for at least two orientations of the DUT in order to capture all the radiations.

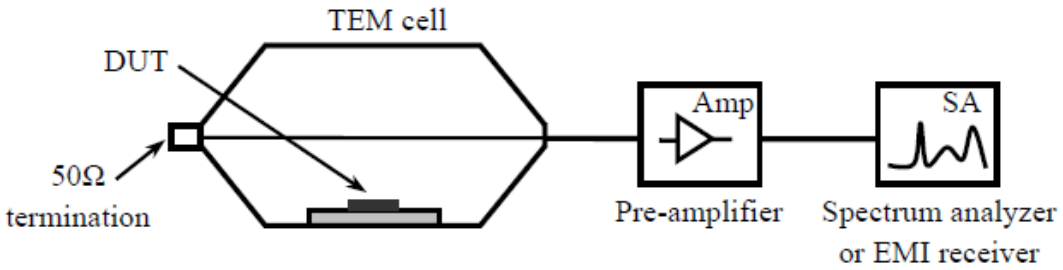

Figure 1-4 Setup of TEM cell method for measuring radiated emissions[4]

Surface scan method: the radiated emissions from the DUT can be measured by scanning with a probe above the DUT, as shown in Figure 1-5. The measurement result of the surface scan method provides not only the electromagnetic fields from the DUT but also the relative strength of the

sources. A variety of probes such as electric, magnetic and optic probes are used for surface scanning.

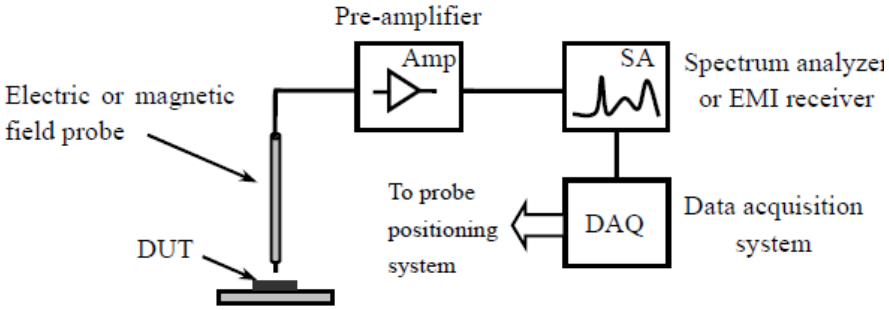

Figure 1-5 Surface scan method [4]

Method of measurement the radiation pattern: the radiation pattern of a DUT in far field can be measured using a receiving antenna.

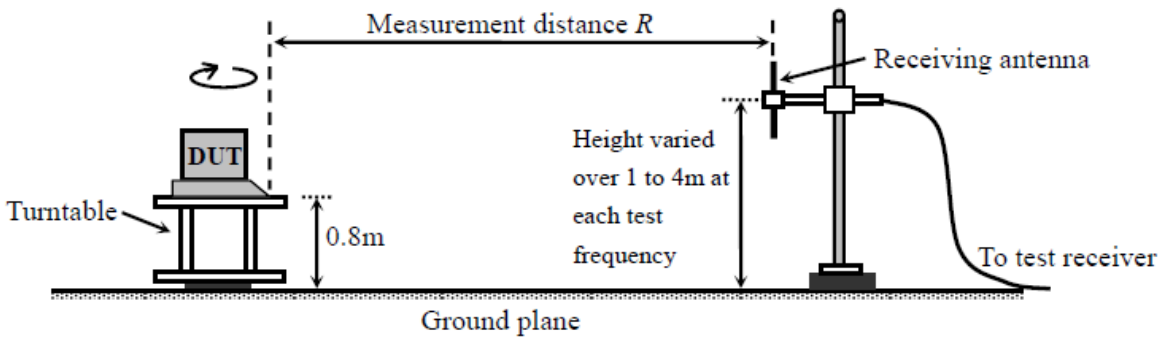

Figure 1-6 Radiation pattern measurement method[4]

The DUT is mounted on a turntable and rotated through 360° to find the maximum emission direction as shown in Figure 1-6. The receiving antenna is scanned in height from 1 to 4m to find the maximum level. The DUT-to-antenna azimuth and polarization are varied through 360° during the measurement to record the radiation pattern of the DUT. The standard test procedure requires that the measurements are to be done on an open area test site or semi-anechoic chamber. A balanced dipole is used as the receiving antenna below 1 GHz, and a log-periodical antenna or a horn antenna should be used for tests above 1 GHz.

Reverberation chamber measurements: A reverberation chamber is an electrically large, highly conductive enclosed cavity equipped with one or more metallic tuners/stirrers whose dimensions are a significant fraction of the chamber dimensions. A typical measurement setup using reverberation chamber is illustrated in Figure 1-7. It is used to measure the total radiated power of a DUT. The DUT should be at least λ/4 from the chamber walls. The stirrers are rotated very slowly compared to the sweep time of the EMI receiver in order to obtain a sufficient number of samples. The mechanical tuners/stirrers can “stir” the multi-mode field in the chamber to achieve a statistically

uniform and statistically isotropic electromagnetic environment. The receiving antenna measure either the maximum received power or averaged received power during a cycle of the stirrers. The recorded signals are then converted to the total radiated power and the free space field strength. The advantage of the reverberation chamber method is that it is able to measure the total field on all sides of a DUT without multiple test positions and orientations.

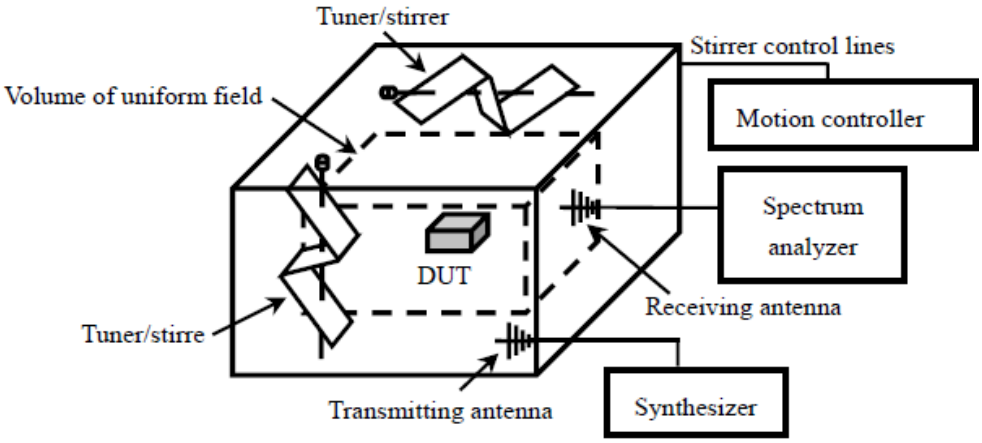

Figure 1-7 Reverberation chamber method[4]

Direct coupling method: The simplified configuration of the 1Ω method for measuring the sum current in the common ground path is shown in Figure 1-8. The direct coupling method determines the conducted emissions from power and signal ports of a small electronic module especially an IC. RF currents developed across a standardized load is measured to allow indirect estimation of the emission level

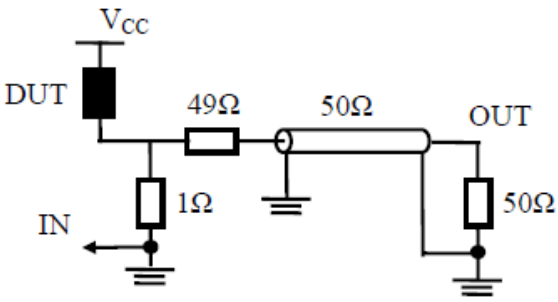

Figure 1-8 1Ω Direct coupling measurement for conducted emissions[4]

Workbench Faraday Cage (WBFC) method: IEC 61967-5 defines a method of measuring the conducted electromagnetic emissions at defined common-mode points in order to estimate the emissions radiated by connected cables. The Faraday cage is typically a metallic box of 500mm x 300mm x 150 mm. A typical workbench of Faraday cage method is shown in Figure 1-9. DUT is mounted on either an IC EMC test board or an application board if it fits inside the WBFC. With all input, output, and power connections to the test board filtered and connected to common-mode chokes, the conducted noise is measured at PCB locations specified by the standard.

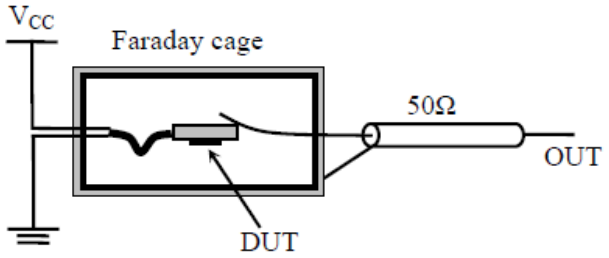

Figure 1-9 Setup of Faraday cage measurement for conducted emissions[4]

Magnetic probe method: IEC 61967-6 defines a method for calculating the conducted emissions from an IC pin using a magnetic field probe to measure the magnetic field associated with a connected PCB trace. The schematic of the measurement setup is shown in Figure 1-10.

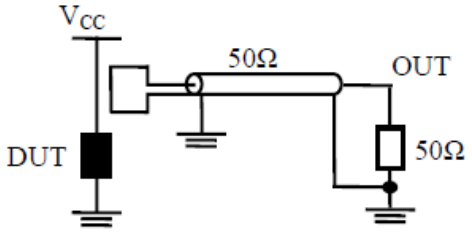

Figure 1-10 Schematic of magnetic probe method for conducted emissions[4]

Standard and method	Measurement	Frequency	Speed	Accuracy	complexity
IEC-61967-2 TEM cell	Radiated emissions	150kHz-1GHz	Fast	Medium	Low
IEC-61967-3 Surface scan	Radiated emissions	10 MHz-1GHz	Slow	High	High
IEC-61967-4 Direct coupling	Conducted CM and DM emissions	150kHz-1GHz	Medium	Medium	Medium
IEC-61967-5 Faraday cage	Conducted CM emissions	150kHz-1GHz	Medium	Medium	Medium
IEC-61967-6 Magnetic probe	Conducted CM and DM emissions	150kHz-1GHz	Medium	Medium	Low
EN-55022 Radiation pattern	Radiated emissions	>30M Hz	Medium	Low	High
EN-61000-4-21 Reverberation chamber	Radiated emissions	>LUF	Medium	Medium	High

Table 1-1 comparison of emission measurements IEC-61967

A magnetic probe is used to measure the magnetic field associated with a connected PCB trace, and the RF currents inside the circuit are then calculated. The preferred test configuration is with the DUT mounted on a standard EMC test board to maximize repeatability and minimize probe

coupling to other circuits. The features of all these PCB emission measurement methods are summarized in Table 1-1[4].

1.3 Near field measurements

Methods such as modulated scattering technique, electro-optic sampling, electron beam probing (modified scanning electron microscope), and perturbation method are already available for the identification and localization of sources. [5], [6] proposes source location estimation technique with the modulated scattering technique (MST) for indoor wireless environments. The uniform circular scatterer array (UCSA) that consist of five optically modulated stutterers as array elements and a dipole antenna at the center of the UCSA is employed for estimating a source location from the impinging signal, but these techniques require expensive components, complicated configuration and low signal to noise ratio.

Electromagnetic near field scanning is a general method for identifying the source of electromagnetic interference (EMI) in electronic circuits. Various methods have been developed by many authors for the calculation of far field pattern leading to the source identification from the near field measurements [7]–[11]. Thus, it is necessary to know the electromagnetic fields in their close environment.

1.3.1 Near field and far field

The space surrounding an antenna is divided into three (1) reactive near field (2) radiative near field and (3) far field. Reactive near field is that portion of the near field region immediately surrounding the antenna whereas in the reactive near field predominates. For most antennas, the outer boundary of this region is taken into exist as at a distance $R<0.62D3/\lambda$.

Radiating near field region is defined as that region of the field of an antenna between the reactive near field region and the far field region where the radiative field predominates and the angular field distribution is dependent upon the distance from the antenna.

Far field region is defined as that region of the field of an antenna where the angular distribution is independent of the distance from the antenna. If D is the maximum overall dimension of the antenna, the far field region is at a distance greater than $2D2/\lambda$, where λ is the wavelength [12].

1.3.2 Why near field measurements?

The electromagnetic emissions can be measured in either near field or far field. The near field measurements have advantages in accuracy, reliability, cost and application range compared with that of the far field measurements. The effect of some uncertain factors such as weather, scattering,

electromagnetic interference has less influence on the measurement because the probe and the DUT are very close to each other and hence it gives a more accurate measurement[13][14].

- The near field measurement is less dependent on test conditions. It can be conducted in normal lab environments rather than an OATS or an anechoic chamber. This makes the technique highly feasible.
- Unlike the far field measurements, which give the radiation in far field, near field measurements can be used not only to obtain electromagnetic fields, but also to provide the emission tests and source diagnostics in EMC studies of PCBs and ICs. It can be used to estimate the current on the microstrip trace of a PCB or to locate the fault in the high frequency chip[15].
- Near field-far field transformation methods and equivalent source methods enhances the application and popularity of the near field measurement method.

Depending on the applications, the near field measurements can be classified into antenna near field measurements and EMC/EMI near field measurements. Antenna near field measurements are performed in the radiating near field range, typically in the range 3λ to 5λ and are focused on the determination of far field pattern from near field. EMC near field measurements are performed in the highly reactive region (typically <λ/6) and are focused on the determination of real or equivalent radiating sources in the DUT.

1.4 Objective of the thesis

The major objective of this thesis is to predict the radiated emissions from a PCB from the near field scan measurements. The steps toward this can be divided into two main tasks.

1) Design of a high resolution and high sensitivity printed circuit magnetic probe for the near field scan measurements.
2) Development of the inverse algorithm for equivalent source representation and prediction of the electromagnetic compatibility.

The state of the art about the near field probes and source reconstruction methods is described in the next chapter (chapter 2) of this thesis.

Chapter 3 of this thesis deals with the design and characterization of printed circuit magnetic field probes for near field measurements. The main goal is the design of the low cost shielded magnetic probes in the printed circuit technology towards the achievement high spatial resolution (of the

order of 100µm). The thesis describes the problems encountered while miniaturization and the solutions we put forward towards the goal. The required frequency band of operation is from 1 MHz – 1 GHz, which is set by the definitions of the project (LOCRAY). The thesis also focuses on the design and characterization of active probes in order to achieve high sensitivity. The effect of the position of the LNA on the probe and the effect of the gain of the LNA are also made under study. The performance of a 3 axis probe which can measure the 3 components of the magnetic field is also analyzed.

Chapter 4 describes the source reconstruction methods from near field scan data for the prediction of radiated emissions from the PCB. The inverse transmission line based on the inverse propagation of electromagnetic probes is used to find the field distribution at the plane of the source. The inverse algorithm is meant to use the near field scanned data measured by the designed probe. This chapter also describes a new method based on the 2D cross-correlation. This method represents the current sources on the PCB by an equivalent current. This chapter contains the validation for elementary current sources and simple PCBs on air. Finally, the radiated far field of the circuit is predicted using the equivalent current. In this, we use the time reversal property of the TLM matrix in order to reverse propagate the electromagnetic waves and reconstruct the radiating source.

Chapter 5 concludes the work of the thesis and also gives the directions for future developments.

1.5 References

[1] "Practical Shielding, EMC/EMI, Noise Reduction, Earthing and Circuit B…." [Online]. Available: https://www.slideshare.net/idctechnologies/practical-shielding-emcemi-noise-reduction-earthing-and-circuit-board-layout..

[2] C. R. Paul, *Introduction to electromagnetic compatibility*. Wiley-Interscience, 2006.

[3] D. D. Hoolihan, "Radiated Emission Measurements at 1/3/10/30 meters," 2010. [Online]. Available: https://interferencetechnology.com/radiated-emission-measurements-at-1351030-meters/. [Accessed: 02-Oct-2017].

[4] X. Tong, "Simplified equivalent modelling of electromagnetic emissions from printed circuit boards," 2010.

[5] "Source Location Estimation Using Phaseless," *Electromagnetics*, vol. 14, pp. 197–212, 2010.

[6] R. Schmitt, D. Winkler, M. Brunner, and B. Lischke, "Electron beam sampling of IC-internal GHz signals," *Electron. Lett.*, vol. 24, no. 4, p. 235, 1988.

[7] Y. Vives-Gilabert, C. Arcambal, A. Louis, F. de Daran, P. Eudeline, and B. Mazari, "Modeling Magnetic Radiations of Electronic Circuits Using Near-Field Scanning Method," *IEEE Trans. Electromagn. Compat.*, vol. 49, no. 2, pp. 391–400, May 2007.

[8] Institute of Electrical and Electronics Engineers. and Institution of Engineering and Technology., *EMC Europe 2011 : proceedings of EMC Europe 2011 York : York, UK, September 26-30, 2011 : 10th International Symposium on Electromagnetic Compatibility.* IEEE, 2011.

[9] H. Weng, D. G. Beetner, and R. E. Dubroff, "Prediction of radiated emissions using near-field measurements," *IEEE Trans. Electromagn. Compat.*, vol. 53, no. 4, pp. 891–899, Nov. 2011.

[10] W. Abdelli, A. Frikha, X. Mininger, L. Pichon, and H. Trabelsi, "Prediction of radiation from shielding enclosures using equivalent 3-D high-frequency models," *IEEE Trans. Magn.*, vol. 51, no. 3, pp. 1–4, Mar. 2015.

[11] Y. Zhang, M. H. Bakr, and N. K. Nikolova, "The solution of transient electromagnetic inverse source problems using time-domain TLM method," *IEEE Trans. Antennas Propag.*, vol. 60, no. 9, pp. 4326–4335, Sep. 2012.

[12] C. Balanis, *Antenna Theory - Analysis and Design*. 1997.

[13] D. Slater, *Near-field antenna measurements*. Artech House, 1991.

[14] G. P. Rodrigue and C. P. Burns, “Cost comparison of near-field measurements and far-field measurements for far-field patterns,” in *1974 Antennas and Propagation Society International Symposium*, 1974, vol. 12, pp. 165–168.

[15] Q. Chen, S. Kato, and K. Sawaya, “Estimation of current distribution on multilayer printed circuit board by near-field measurement,” *IEEE Trans. Electromagn. Compat.*, vol. 50, no. 2, pp. 399–405, May 2008.

2. State of the art

2.1 Near Field Probes

Based on the configuration of the probe, there are two near field measurement setups as shown in Figure 2-1[1]. In the first configuration, the measurements done with a single probe controlled by a precise positioning system. The second one uses a planar array of probes terminated with 50 Ohm impedance. With this probe array, the DUT can be scanned in a single measurement or in a few numbers of measurements depending on the area of the DUT and the probe array. In this setup, the presence of a large number of probes induces first order disturbances to the measured field. The former one, which uses single probe is the widely used method for near field scanning[2][3].

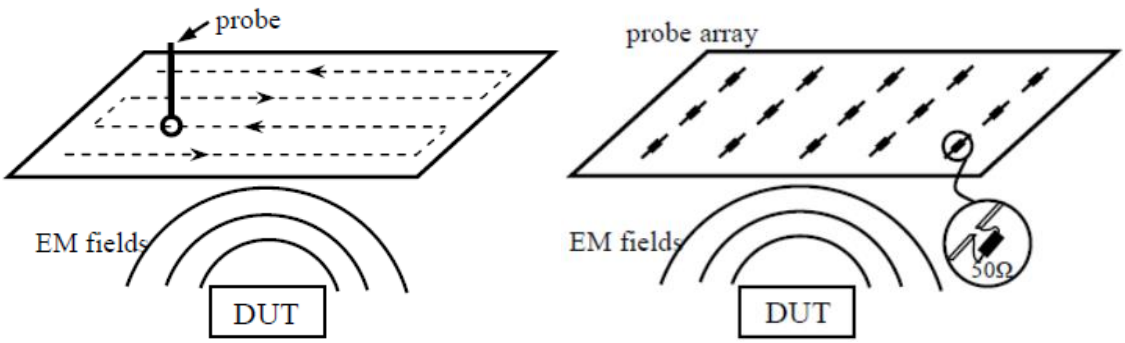

(a) scanning with a single probe (b) Measurement with a probe array

Figure 2-1 Probe setup in near field measurement[1]

The near-field probes (NFPs) have been widely studied recent years because of their ability to quantify the near-field (optical, electrical or magnetic field) strength in the space close to the noise sources. Most of the studies about the NFPs focused on the improvement of spatial resolution, available bandwidth, and suppressing the coupled field in an orthogonal direction or adverse field.

2.1.1 Electro-optical probes

Optical magnetic field probe which has a loop antenna element and an optoelectronic crystal is presented in [4]–[7]. The study in [4] analyzes the invasiveness of the optical magnetic field probes quantitatively by experiment and finite difference time domain (FDTD) method simulation. The

metallic cables in the shielded loop coils introduce disturbance to the original magnetic field, this can be eliminated by replacing the metallic cables by optical fiber cable.

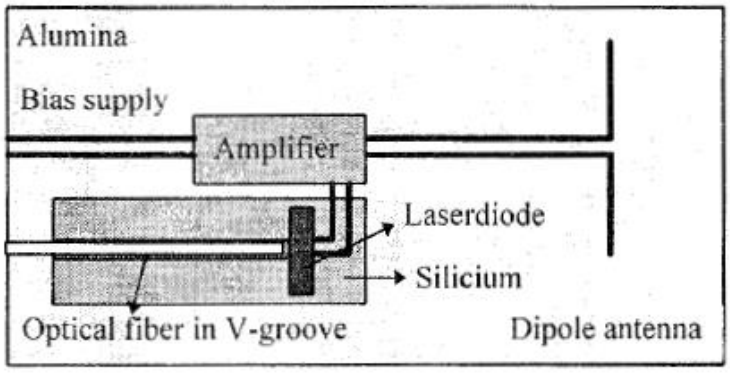

Figure 2-2 Schematic layout of active electro-optical dipole antenna [6]

Figure 2-3 A commercial electro-optical probe [8]

An optical probe for simultaneous measurements of electric and magnetic near fields as shown in Figure 2-2 is presented in [6]. The probe consists of a loop antenna element doubly loaded with LiNbO EO crystals. One of the LiNbO has two domains where -axes (optical axes) in each domain are directly opposite to each other. Using optical technology, the probe can work as a conventional double-loaded loop probe without metallic cables and electrical hybrid junctions. An electro-optical probe which uses an electro-optical crystal (shown in Figure 2-3) is available commercially from Kapteos[8]. The spatial resolution of these probes are around (<=) 1mm.

2.1.2 Electromagnetic probes

An electromagnetic probe consists of a loop or a dipole and a transmission line which carries the signal induced at the loop terminals. An electric probe consists of a dipole and a magnetic probe consists of a loop as detecting element. Various standard antennas for measuring radio-frequency electric and magnetic fields are developed. The standard probes described are an electrically short dipole, a resistively-loaded dipole, a half-wave dipole, an electrically small loop, and a resistively-loaded loop. A single-turn loop designed for simultaneous measurement of the electric and magnetic components of near-fields and other complex electromagnetic environments is described

in[9]. Each type of antenna demonstrates a different compromise between broadband frequency response and sensitivity.

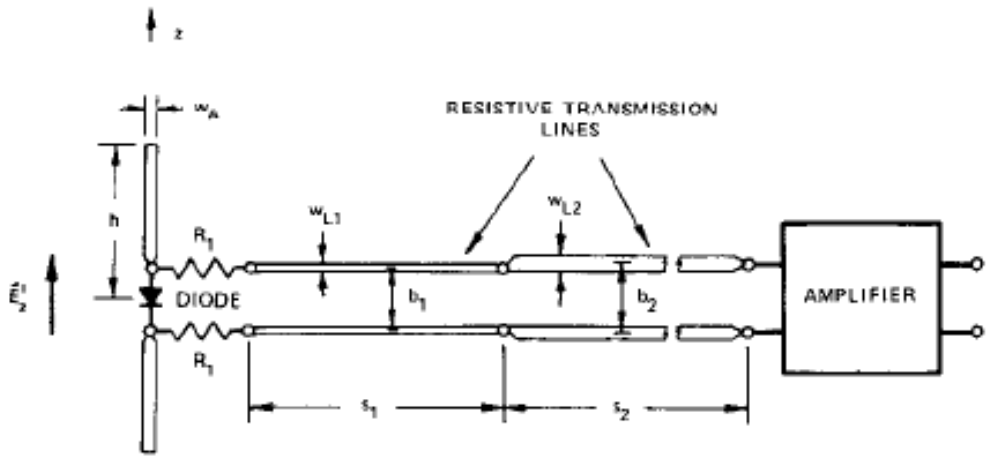

(a)

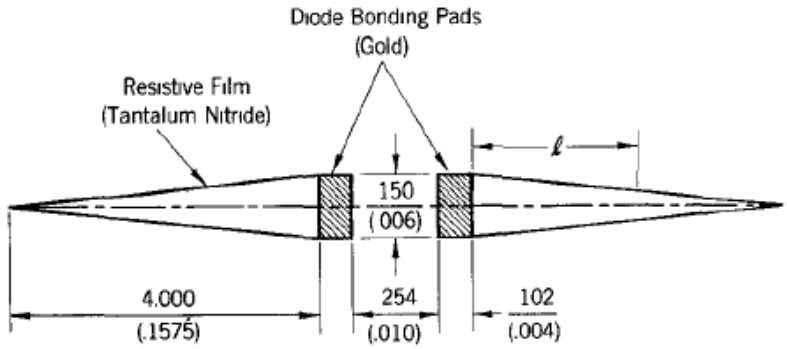

(b)

Figure 2-4 Model for dipole receiving probe[10][11]

A common design for an electric probe consists of an electrically-short antenna with a diode across its terminals a resistive; parallel-wire transmission line transmits the detected signal from the diode to the monitoring instrumentation (Figure 2-4 (a)). Small dipoles are desirable because they provide high spatial resolution of the field, and because they permit a frequency-independent response at higher microwave frequencies [10]. The important problem associated with the electric dipole probes is the disturbance offered to the device under test by the probe itself. The use of resistive tapering, by means of thin-film deposition and photoetching techniques, has been shown to yield significant improvements over conventional dipole elements (Figure 2-4 (b)). These include broader bandwidth, flatter frequency response, wider dynamic range, smaller size, reduced EM-field perturbation and distortion, and complete absence of in-band resonances[11]. Waveguide probes are also used for near field measurements (shown in Figure 2-5)[12]. Open-ended waveguides measure the E field component.

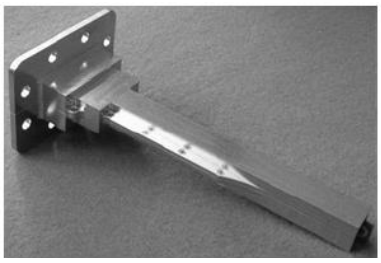

Figure 2-5 Waveguide probe[13]

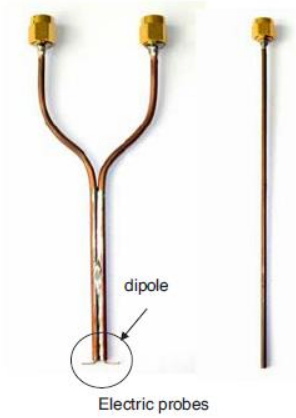

Figure 2-6 Electric probes[14]

The electric probe fabricated by [14] in an open-ended coaxial cable is shown inFigure 2-6. In the case of an electric dipole probe, the current induced can be calculated based on the capacitive model as

$$i = j\omega\varepsilon_0 E_z \qquad 2\text{-}1$$

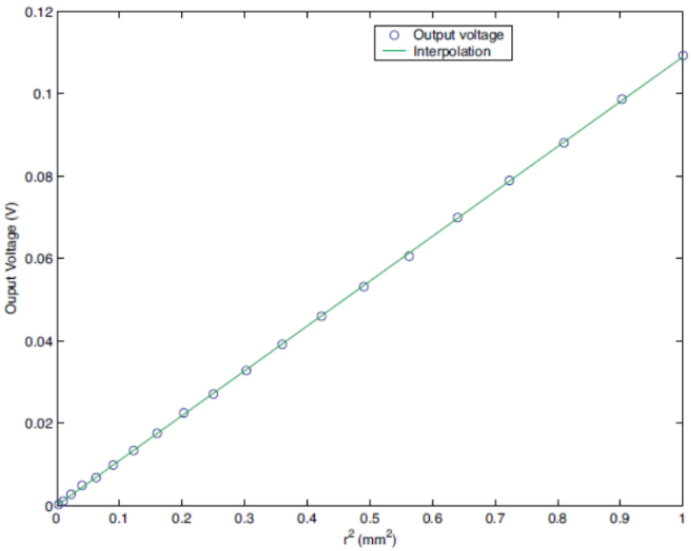

Figure 2-7Output voltage for different diameters of probe microstrip line configuration [14]

The capacitive model does not take into account coupling with external conductors. The simulated output voltage of the probe for different diameters of the inner conductor, by inserting it into a rectangular waveguide to avoid coupling with external conductors is shown in Figure 2-7. The output voltage increases when the dimensions of the probe increase.

A loop operates according to Faraday's law. A voltage is induced at the terminals of the loop when the magnetic flux through the loop changes [15].

$$V_{emf} = -\frac{d\phi}{dt} = -\frac{d}{dt}\iint_S \vec{B}.d\vec{S} \qquad 2\text{-}2$$

As it is obvious from equation 2-2, the voltage induced on the probe depends on the size of the loop; hence the sensitivity of the loop is directly proportional to the size of the loop. The finite loop probe contains not only the usual circulating current which is proportional to the magnetic field but also certain currents which do not depend on the component of magnetic field, but rather on the average electric field in the plane of the loop. Very large errors are possible when a singly-loaded loop is used to measure magnetic fields unless its diameter is less than 0.01λ. The doubly-loaded probe may be used with comparable accuracy when its diameter is as large as 0.15λ [16].

Electromagnetic probes are fabricated using different technologies such as CMOS integration technology LTCC, thin film technology and PCB technology. The very classic magnetic probes is a circular or elliptical loop fabricated by hand and connected to the ground and signal lines of a semi-rigid coaxial cable as shown in Figure 2-8(a) [17]. These probes are not suitable when there is a requirement for high spatial resolution because they are difficult to fabricate manually. Different miniaturized probes are fabricated using the thin film technology. A miniaturized thin film magnetic probes for LSI measurement proposed by [18] is shown in Figure 2-8 (b). . Figure 2-8(c) shows an LTCC probe fabricated by [19]. To miniaturize further and improve the frequency band, integrated probes and probes on LTCC (Low temperature Co fired Ceramics) are used [18]–[22]. A silicon integrated RF magnetic field probe presented by [19] is shown in Figure 2-8(d). It is micro fabricated using CMOS–silicon-on-insulator (SOI) technology with a 0.15 µm design rule on a high-resistivity silicon substrate.

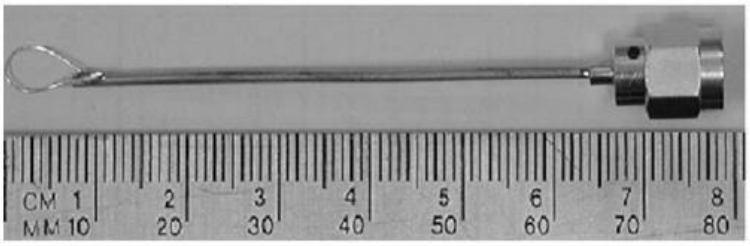

(a)

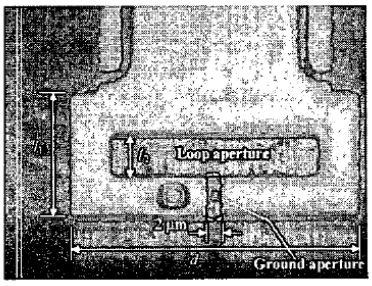

(b)

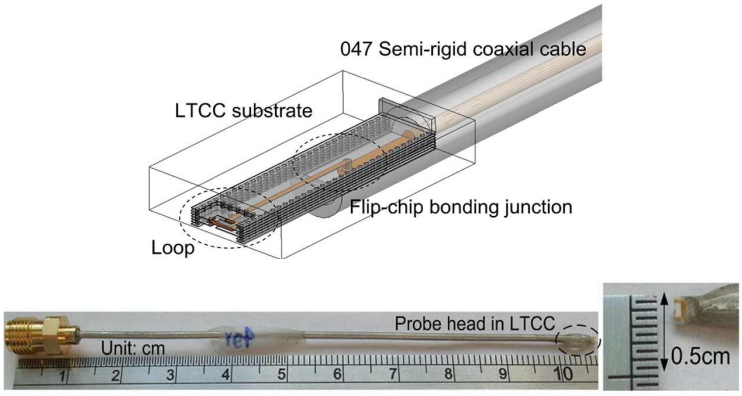

(c)

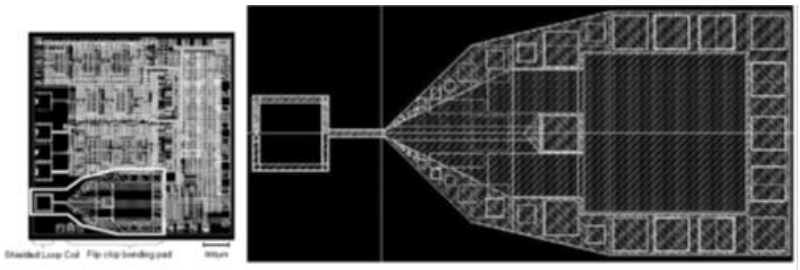

(d)

Figure 2-8 Magnetic probes fabricated on different technologies (a) coaxial probe with elliptical aperture [17] (b) thin film[18] (c)- LTCC probe [19] (d) CMOS SOI probe [20]

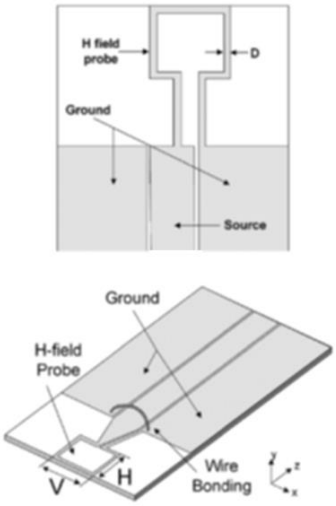

(a)

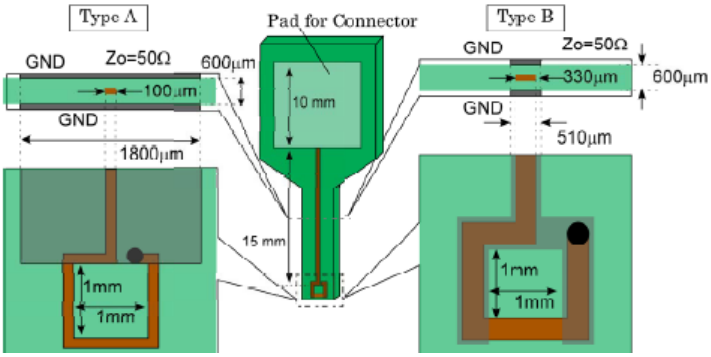

(b)

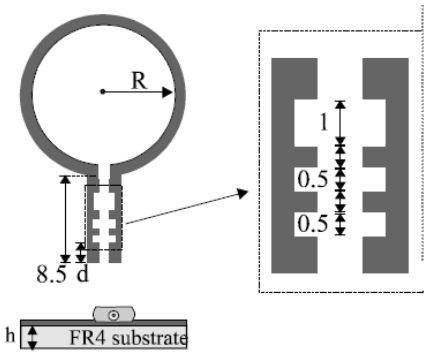

(c)

Figure 2-9 Different printed circuit probes: (a) loop with a tapered CPW transmission line [23] (b) probe with a bare loop and stripline loop [24] (c) loop with microstrip filter [25]

There is quite a little literature on the printed circuit magnetic field probes. Since the LTCC, thin film and integrated technologies are quite expensive; this work focuses on probes based on the printed circuit technology. A rectangular loop probe with CPW fed line is proposed in [23]. The length and width of the loop are 5mm x 5mm with the conductor width of 0.5mm. A tapered

transition is adapted in this paper in addition to the air bridge between the two ground planes (Figure 2-9 (a)). The probe is fabricated on a Teflon substrate with permittivity 2.5 and height 0.508mm. The authors claim that the proposed probe miniaturizes the spurious radiation and resonances by connecting the ground planes together and adapting a tapered transition. The probe works from 1 GHz-7 GHz. Two types of printed circuit magnetic probe for GHz band is proposed in [24], shown in Figure 2-9 (b). Type A is a bare loop and Type B is a strip line loop. The loop aperture has an area of 1 square millimeter and is fabricated on FR4 substrate. Later in 2009, a printed circuit magnetic probe shown in Figure 2-9(c), with a set of quasi periodic notches which acts as microstrip filters were proposed in [25]. This probe was fabricated on an FR4 substrate with a 0.8mm thickness, the aperture of the loop is 8mm (R=4mm).

The sensitivity of the probe is improved by using carrier suppression technique in [26]. An array of active magnetic probes is designed by M. Yamaguchi, using CMOS integration technology [3]. An active electro-optical probe for medical MRI is proposed by [5]. These researches don't provide any information about the amplifier characteristics or the influence of the integrated amplifier on the measurement result.

The measurements in near fields and far field requires separate probes [27]. The disturbance of the probe in the far field is negligible when a probe with maximal sensitivity is used. This is not the case with the near field. The smaller the dimensions of the probe, the smaller will be the disturbances to the device under test and the higher the spatial resolution.

2.2 Synthesis of radiating sources

At present, inverse problems arise in many branches of applied sciences, such as medical diagnostics, atmospheric sounding, radar and sonar target estimation, seismology, radio astronomy, and microscopy. In a general context, an inverse problem can be broadly described as a problem of determining the internal structure or past state of a system from external measurements, which corresponds to the inverse of the usual cause-effect sequence of events. In the domain of electromagnetism, inverse problems are divided into two categories:

(1) Inverse scattering problems (inverse medium problems), which obtain the characteristics of a scattering object from its scattered wave due to external illumination, and

(2) Inverse source problems, which determine the constitution of a source from measured values of its emitted radiation.

Other common applications of inverse source problems are concealed weapon detection, non-destructive evaluation or testing, and remote sensing [28][29][30]. The inverse source problems, in

contrast, have received little attention, partially because of the severe non-unique nature in the solutions. Despite this ill-posedness, inverse source problems are still applied directly in antenna design [31]and holographic imaging [32]. Inverse source problems have already been studied in the frequency domain [29] and in time domain [30].

The earliest works on modelling the far field emissions were direct near-field to far-field transformation based on modal expansion methods as shown in Figure 2-10(a) [33][34]. The fields radiated by a DUT are expanded in terms of planar, cylindrical, or spherical wave functions in order to obtain the far field, and the measured near-field data are used to determine the coefficients of the wave functions. An equivalent source representation composed of both magnetic and electric dipoles placed over a fictitious sphere surrounding the AUT is obtained in [34]. A linear relation between the transmission coefficients of the AUT and the transmission coefficients of each dipole derived by a spherical wave expansion (SWE) of the NF measurements. Dipole transmission coefficients are determined using the translational and rotational addition theorems, and a least square method is employed to compute the excitation of each current source.The equivalent currents are placed in the aperture in front of the antenna so these methods do not apply to emissions in the other half space behind the antenna.

The equivalent source reconstruction from the radiated field is applied in antenna synthesis to reconstruct the equivalent source of antennas from its radiated near field as illustrated in Figure 2-10 (b). A method for computing the far field of an antenna from the near field measurements taken over an arbitrary geometry is presented in [35]. An integral equation is used to relate the near field data to the equivalent current and the MOM method is used to solve the equation by transforming it into a matrix equation. The authors in [36] present a method that reconstructs directly the sources from the knowledge of the electric field amplitude data over some region. The sources are reconstructed in terms of an equivalent magnetic current density and the equivalence principle has been used to represent the Antenna under test. With these methods, the correct far field in front of the antenna can be produced regardless of the geometry of the near-field measurement. Another way is to identify the real or equivalent sources bound to the actual DUT surface in order to locate the radiating source as shown in Figure 2-10 (c). As the near-field data must fully reflect the characteristics of the source, scans are performed in very close proximity of the DUT. After the real or equivalent sources are identified, the near and far fields can be then calculated either analytically or numerically.

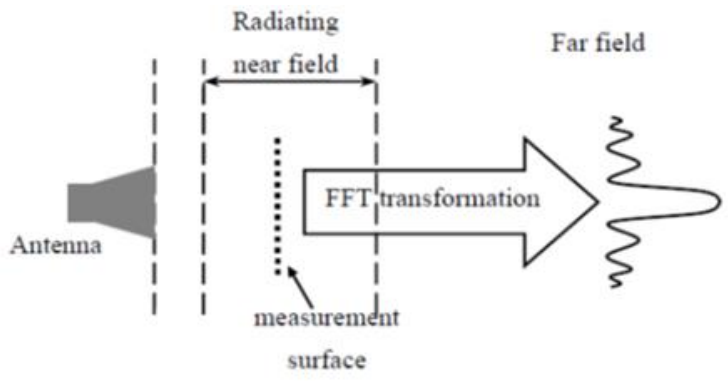

(a)

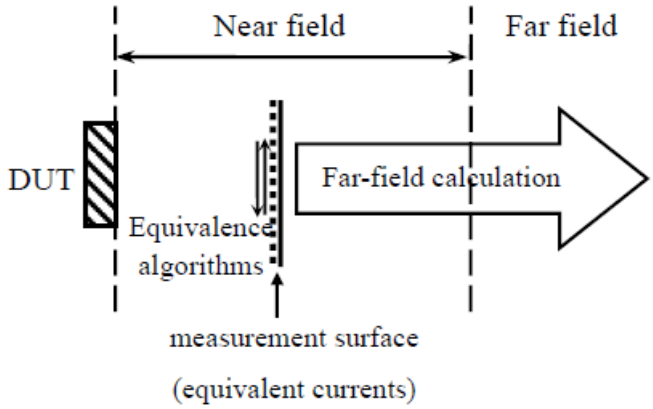

(b)

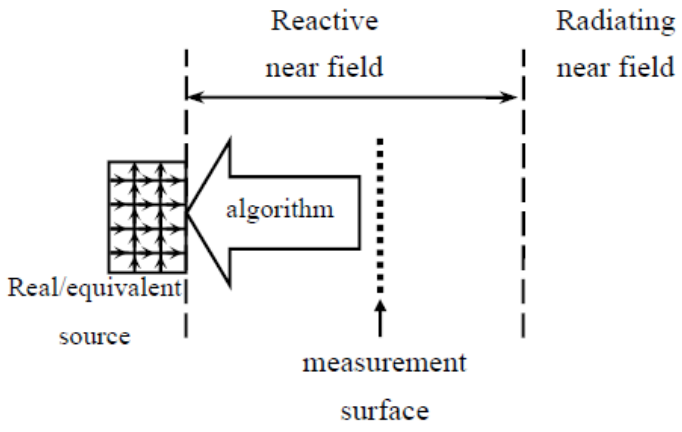

(c)

Figure 2-10 Different ways of modelling emissions from near field measurement[1]

The approach of source reconstruction is harnessed to model the radiated emissions from PCBsand electronic devices. The equivalent source of the source distribution is obtained by numerical methods. After obtaining this equivalent source, it is quite easy to conduct source diagnostics, near-field prediction, evaluation of the radiation performance regularized by the EMC standards like the

radiated emission limitation at 3 m, 10 m even 30 m away from the DUT, and investigation of interactions between the PCBs and the shielding cavities [37][38]. The recent development in source reconstruction for EMC is done by Ping Li and Li Jun Jiang [38], in which the near field scan data from two planes, one above and one below the PCB as shown inFigure 2-11 are used to reconstruct the sources in terms of equivalent electric and magnetic currents which are represented by a set of Rao–Wilton–Glisson basis functions.

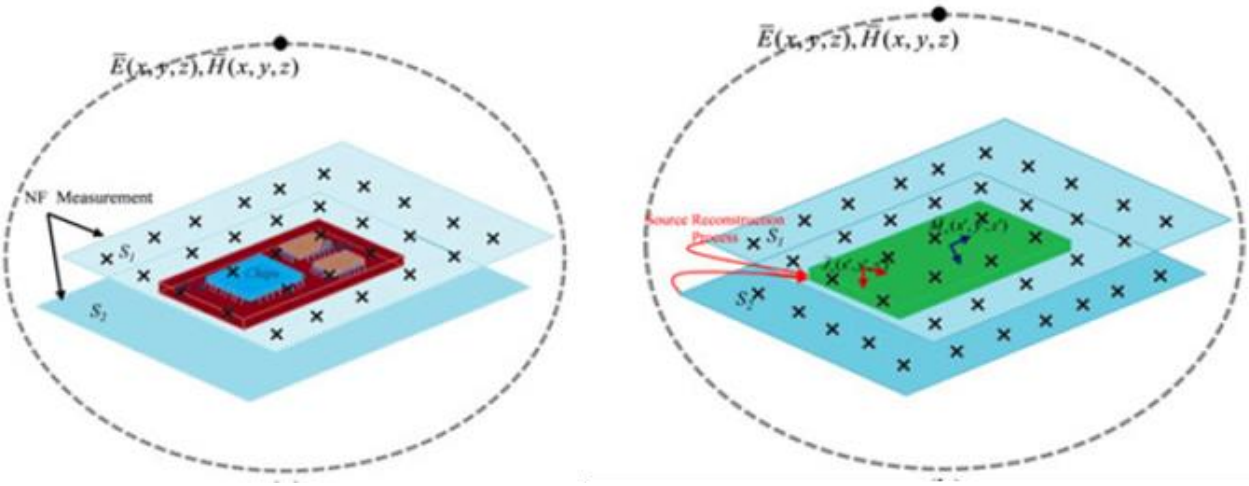

(a) (b)

Figure 2-11 Equivalent source reconstruction problem (a) measurement schematic (b) the equivalent current source domain is the whole surface of the original PCB and it is solved by matching the measured tangential magnetic fields over two planes S1 and S2. [38]

TLM method has been a powerful numerical technique for solving electromagnetic structure problems including high-speed RF/microwave circuits, antennas [39][40]The time-reversal property of the TLM method was utilized for the localization of scattering objects from external field measurement in the time domain. In [41] non-uniqueness of the inverse source problem is addressed by additionally imposing smoothness constraints. Both the source solution and the field measurements are performed in the time domain. The inverse problem in their paper deals with the reconstruction of a transient source distribution inside a closed region in free space.

2.3 Conclusion

The near field scanning probes in the literature is for frequencies above 1 GHz. The higher resolution probes is said to operate in the frequencies above 3 GHz. The probes with high spatial resolution in the range of micrometers (µm) were always achieved with expensive CMOS, LTCC or thin film technologies. There was no information in the literature about the near field probes which operates in the frequencies below 1 GHz with spatial resolution below 1 mmusing the printed

circuit technology. The influence of the amplifier factors such as gain, noise figure and position on the probe on the performance of the active probe has to analyze.

The source reconstruction incorporates the electric or magnetic field integral equations with the numerical methods such as MoM. Most of these methods needs to have information about the device under test in order to predict the radiated field and requires large computational time and memory. Use of the near field data from two planes above and below the device under test requires large scanning time. So, it is required to have a method for the reconstruction of sources with near field scan data from single plane to reduce the scanning time and the memory of computation.

2.4 References

[1] X. Tong, "Simplified equivalent modelling of electromagnetic emissions from printed circuit boards," 2010.

[2] K. Sugawara, C. P. Chen, Z. Ma, T. Anada, and D. W. P. Thomas, "Non-contacting electric and magnetic field probe for measuring EM fields on microwave planar circuits," in *Asia-Pacific Microwave Conference Proceedings, APMC*, 2007, pp. 1–4.

[3] S. Aoyama, S. Kawahito, and M. Yamaguchi, "An active magnetic probe array for the multiple-point concurrent measurement of electromagnetic emissions," *IEEE Trans. Magn.*, vol. 42, no. 10, pp. 3303–3305, 2006.

[4] I. Of, O. Magnetic, F. Probes, W. A. Loop, and A. Element, "INVASIVENESS OF OPTICAL MAGNETIC FIELD PROBES," pp. 4–7.

[5] K. Sven, S. Kuhn, N. Kuster, and B. Kochali, "Active electro-optical probe system for B1-field polarization mapping in magnetic resonance imaging systems," *Electromagn. Compat. Tokyo (EMC'14/Tokyo), 2014 Int. Symp.*, pp. 666–669, 2014.

[6] K. Haelvoet, L. Vanwassenhove, L. Martens, P. Vandaele, and and P. V. K. Haelvoet, L. Vanwassenhove, L. Martens, "An active electro-optical loop and dipole probe for electromagnetic near-field measurements," *Proc. 20th Bienn. Conf. Precis. Electromagn. Meas.*, pp. 421–422, 1996.

[7] E. Suzuki, S. Arakawa, H. Ota, K. I. Arai, R. Sato, and K. Nakamura, "EO probe for simultaneous electric and magnetic near-field measurements using LiNbO3 with inverted domain," *IEEE Trans. Microw. Theory Tech.*, vol. 53, no. 2, pp. 696–701, 2005.

[8] "Your key partner for electromagnetism in harsh environment - Kapteos." [Online]. Available: http://www.kapteos.com/en/welcome/. [Accessed: 02-Oct-2017].

[9] M. Kanda, "Standard Probes for Electromagnetic Field Measurements," *IEEE Trans. Antennas Propag.*, vol. 41, no. 10, pp. 1349–1364, 1993.

[10] G. S. Smith, "Limitations on the Size of Miniature Electric-Field Probes," *IEEE Trans. Microw. Theory Tech.*, vol. 32, no. 6, pp. 594–600, 1984.

[11] M. Kanda and L. D. Driver, "An Isotropic Electric-Field Probe with Tapered Resistive Dipoles for Broad-Band Use, 100 kHz to 18 GHz," *IEEE Trans. Microw. Theory Tech.*, vol. 35, no. 2, pp. 124–130, Feb. 1987.

[12] W. K. Park, S. S. Oh, S. Y. Kang, P. Roblin, and H. D. Park, "Waveguide probe with size-reduced aperture using split-ring resonator array for near-field measurements," *Electron. Lett.*, vol. 45, no. 6, p. 297, 2009.

[13] W. K. Park, S. S. Oh, S. Y. Kang, P. Roblin, and H. D. Park, "Waveguide probe with size-reduced aperture using split-ring resonator array for near-field measurements," *Electron. Lett.*, vol. 45, no. 6, p. 297, 2009.

[14] D. Baudry, a. Louis, and B. Mazari, "Characterization of the Open-Ended Coaxial Probe Used for Near-Field Measurements in Emc Applications," *Prog. Electromagn. Res.*, vol. 60, pp. 311–333,

2006.

[15] E. Jordan, “Electromagnetic waves and radiating systems,” *Prentice-Hall Englewood Cliffs*. p. 753, 1968.

[16] H. Whiteside and R. W. P. King, “The Loop Antenna as a Probe,” *IEEE Trans. Antennas Propag.*, vol. 12, no. 3, pp. 291–297, May 1964.

[17] J. Shi, M. A. Cracraft, K. P. Slattery, M. Yamaguchi, and R. E. DuBroff, “Calibration and compensation of near-field scan measurements,” *IEEE Trans. Electromagn. Compat.*, vol. 47, no. 3, pp. 642–650, 2005.

[18] N. Ando *et al.*, “Miniaturized thin-film magnetic field probe with high spatial resolution for LSI chip measurement,” *2004 Int. Symp. Electromagn. Compat. (IEEE Cat. No.04CH37559)*, vol. 2, 2004.

[19] Y. T. Chou and H. C. Lu, “Magnetic near-field probes with high-pass and notch filters for electric field suppression,” *IEEE Trans. Microw. Theory Tech.*, vol. 61, no. 6, pp. 2460–2470, 2013.

[20] M. Yamaguchi, S. Koya, H. Torizuka, S. Aoyama, and S. Kawahito, “Shielded-loop-type onchip magnetic-field probe to evaluate radiated emission from thin-film noise suppressor,” *IEEE Trans. Magn.*, vol. 43, no. 6, pp. 2370–2372, 2007.

[21] Y. Gao and I. Wolff, “A new miniature magnetic field probe for measuring three-dimensional fields in planar high-frequency circuits,” *IEEE Trans. Microw. Theory Tech.*, vol. 44, no. 6, pp. 911–918, 1996.

[22] M. Yamaguchi, S. Muroga, S. Nanba, K. Arai, K. Yanagi, and Y. Endo, “A 60 × 60 μ m 2 Size Planar Shielded Loop Probe for Low Lift-Off On-Chip Magnetic Near Field Measurements,” *Proc. 2013 Int. Symp. Electromagn. Compat. (EMC Eur. 2013)*, pp. 977–980, 2013.

[23] J. M. Kim, W. T. Kim, and J. G. Yook, “Resonance-suppressed magnetic field probe for em field-mapping system,” in *IEEE Transactions on Microwave Theory and Techniques*, 2005, vol. 53, no. 9, pp. 2693–2699.

[24] H. Funato and T. Suga, “Magnetic near-field probe for GHz band and spatial resolution improvement technique,” *2006 17th Int. Zurich Symp. Electromagn. Compat.*, pp. 284–287, 2006.

[25] S. Y. Lin, S. K. Yen, W. S. Chen, and P. H. Cheng, “Printed magnetic field probe with enhanced performances,” *APMC 2009 - Asia Pacific Microw. Conf. 2009*, no. 840, pp. 649–652, 2009.

[26] H. Kikuchi, S. Yabukami, M. Yamaguchi, K. I. Arai, and T. Suzuki, “Improvement of sensitivity using carrier suppression technique in high frequency carrier type thin-film magnetic field sensor,” in *INTERMAG Europe 2002 - IEEE International Magnetics Conference*, 2002, p. DQ13.

[27] W. Joseph and L. Martens, “The influence of the measurement probe on the evaluation of electromagnetic fields,” *IEEE Trans. Electromagn. Compat.*, vol. 45, no. 2, pp. 339–349, May 2003.

[28] H. M. Chen, S. Lee, R. M. Rao, M. A. Slamani, and P. K. Varshney, “Imaging for concealed weapon detection,” *IEEE Signal Process. Mag.*, vol. 22, no. 2, pp. 52–61, Mar. 2005.

[29] J. H. Bungey, “Sub-surface radar testing of concrete: A review,” *Construction and Building Materials*, vol. 18, no. 1. pp. 1–8, 2004.

[30] B. W. Schilling and G. C. Templeton, “Three-dimensional remote sensing by optical scanning holography,” *Appl. Opt.*, vol. 40, no. 30, pp. 5474–5481, Oct. 2001.

[31] C. Muller, “Electromagnetic radiation patterns and sources,” *IRE Trans. Antennas Propag.*, vol. 4, no. 3, pp. 224–232, Jul. 1956.

[32] K. P. Gaikovich, P. K. Gaikovich, Y. S. Maksimovitch, and V. A. Badeev, “Subsurface Near-Field Microwave Holography,” *IEEE J. Sel. Top. Appl. Earth Obs. Remote Sens.*, vol. 9, no. 1, pp. 74–82, Jan. 2016.

[33] W. M. Leach and D. T. Paris, “Probe Compensated Near-Field Measurements on a Cylinder,” *IEEE Trans. Antennas Propag.*, vol. 21, no. 4, pp. 435–445, Jul. 1973.

[34] M. Serhir, P. Besnier, and M. Drissi, “An accurate equivalent behavioral model of antenna radiation using a mode-matching technique based on spherical near field measurements,” *IEEE Trans. Antennas Propag.*, vol. 56, no. 1, pp. 48–57, 2008.

[35] T. K. Sarkar and A. Taaghol, “Near-field to near/far-field transformation for arbitrary near-field geometry utilizing an equivalent electric current and MoM,” *IEEE Trans. Antennas Propag.*, vol. 47, no. 3, pp. 566–573, Mar. 1999.

[36] F. Las-Heras and T. K. Sarkar, “A direct optimization approach for source reconstruction and NF-FF transformation using amplitude-only data,” *IEEE Trans. Antennas Propag.*, vol. 50, no. 4, pp. 500–510, Apr. 2002.

[37] H. Weng, D. G. Beetner, and R. E. Dubroff, “Prediction of radiated emissions using near-field measurements,” *IEEE Trans. Electromagn. Compat.*, vol. 53, no. 4, pp. 891–899, Nov. 2011.

[38] P. Li and L. J. Jiang, “Source reconstruction method-based radiated emission characterization for PCBs,” *IEEE Trans. Electromagn. Compat.*, vol. 55, no. 5, pp. 933–940, 2013.

[39] D. M. Hailu, S. Member, N. K. Nikolova, S. Member, and M. H. Bakr, “Sub-wavelength Microwave Radar Imaging for Detection of Breast Cancer Tumors,” *2007 Int. Symp. Signals Syst. Electron.*, pp. 107–110, Jul. 2007.

[40] A. Ungureanu, Y. Fu, T. P. Vuong, and F. Ndagijimana, “Electromagnetic source synthesis by reversed-TLM method,” *IEEE MTT-S Int. Microw. Symp. Dig.*, 2011.

[41] Y. Zhang, M. H. Bakr, and N. K. Nikolova, “The solution of transient electromagnetic inverse source problems using time-domain TLM method,” *IEEE Trans. Antennas Propag.*, vol. 60, no. 9, pp. 4326–4335, Sep. 2012.

3. Design and characterization of printed circuit magnetic probes

3.1 Introduction

Near field scanning is a general method for the measurement of radiated emissions from PCBs. The accuracy of this measurement depends on the probes used for the near field scan. As seen in the literature, the sensitivity and selectivity of the probe are inversely proportional. Therefore, the objective of this chapter is to design a magnetic probe with high sensitivity and high spatial resolution. The design and characterization of high-resolution magnetic probes using printed circuit technology are discussed in this chapter. The sensitivity of the probe is enhanced by integrating a Low noise amplifier at the probe output. The active probe discussed here is the first active probe in the literature, which is fabricated using printed circuit technology. The validation of active probes and three axis probes are also contained in the following sections.

3.2 Parameters of the probe

The important parameters of the probe are listed in Figure 3-1.

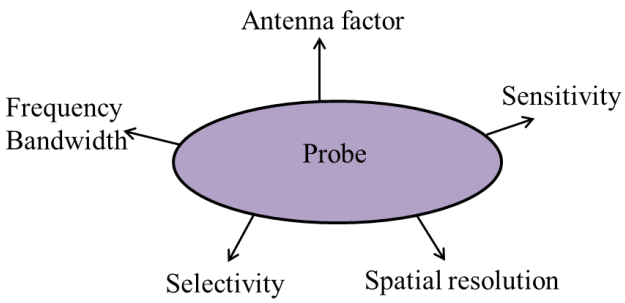

Figure 3-1 Parameters of the probe

Sensitivity: The sensitivity is defined as the minimum detectable signal of the quantity to be measured by the probe. The sensitivity of the probe increases with the increase in the size of the probe.

Selectivity: It is the ability of the probe to distinguish between the normal component and the tangential component of the electric or magnetic field.

Spatial resolution: The Rayleigh criterion defined the spatial resolution as the ability to discriminate two RF sources in close proximity. That amounts to determining a distance δ from which the system will be unable to distinguish these two sources. The spatial resolution in the case of the dipole is estimated to be equal to half of the length of the dipole probe.

Antenna factor: The antenna factor of a dipole is defined by the ratio between the incident field and the voltage induced at the input of a receiver. The antenna factor is defined as the ratio between the electric or the magnetic field of the circuit under test and the voltage induced at the probe when placed on the device under test.

$$AF_{\ in\ S/m} = \frac{H_{\ in\ A/m}}{V_{\ in\ V}} \qquad 3\text{-}1$$

And the antenna factor in dB is expressed as

$$AF_{\ in\ \ dBS/m} = H_{\left(\frac{dBA}{m}\right)} - V_{\ (dBV)} \qquad 3\text{-}2$$

For calculating this parameter the theoretical or the simulated magnetic field of the DUT is divided with the measured voltage or the simulated voltage at the probe.

The antenna factor (AF) can be derived theoretically from Ampere's law as

$$AF = \frac{1}{j\omega\mu nS} \qquad 3\text{-}3$$

Where, n is the number of turns, S is the area of the loop and $\boldsymbol{\omega}$ is the angular frequency

The AF is important to know the level of the field above the DUT when using the probe in the near-field measurement system.

3.3 The near field test bench

The characterization of the probe is performed with the near field test bench. A near field test bench has been developed by IRSEEM (Research Institute for Electronic Embedded Systems, the laboratory at Rouen, France) to collect the electromagnetic field close to devices of various sizes. The system is based on a direct measurement method and its schematic is shown in Figure 3-2. The probe is connected to the spectrum analyzer through the arm of the robot, which is mounted on a 5 axis robot at the same time. The 5 axis robot is shown in the photograph of the near field test bench in Figure 3-3. A computer monitors the probe displacement over the device under test and acquires data provided by the spectrum analyzer. The maximum scanning area is of size 200cm (x) x 100cm (y) x 60cm (z) with a mechanical resolution of 10µm in the three directions (x,

y and z) and 0.009° for two rotations. To ensure high resolution the probe must be close to the surface of the device under test due to the coupling with evanescent waves.

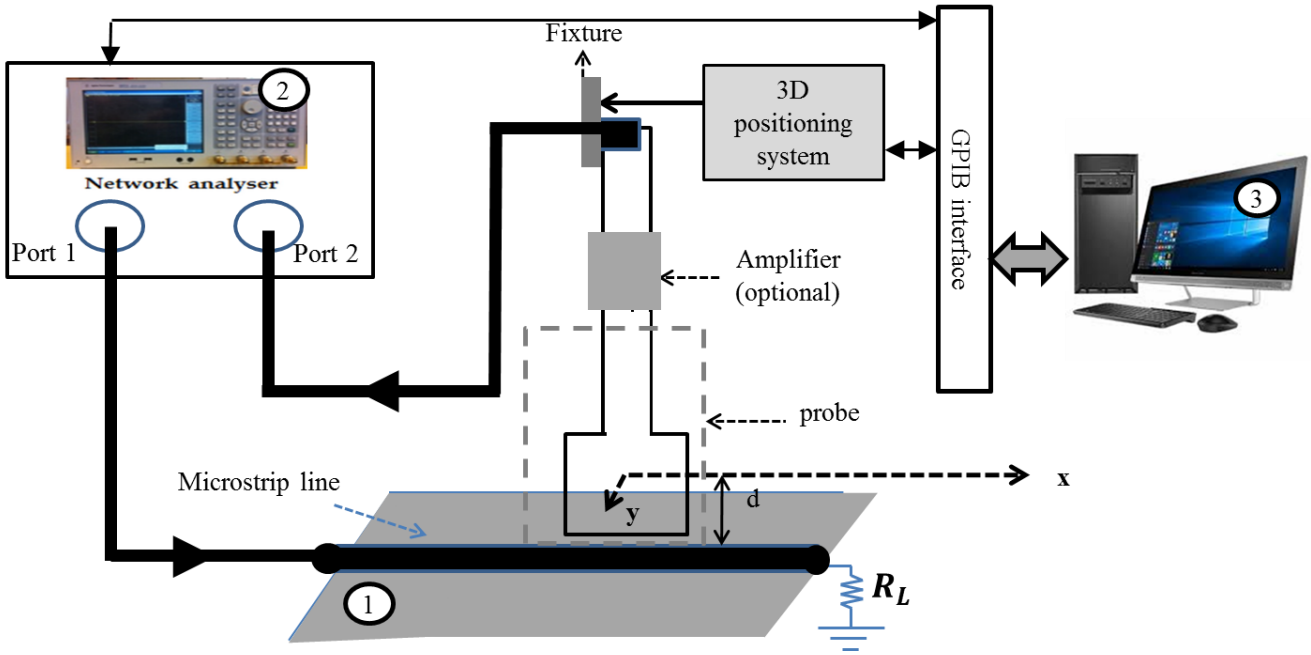

Figure 3-2 Schematic of the near field characterization setup

The 3D positioning system can be made to operate in 2 scanning modes,

1. A constant height mode and

2. A constant distance between the probe and a device under test mode.

The distance between the probe and the DUT is kept constant by using the relief model of the object to regulate probe position. The method used to acquire the relief model of objects is based on laser triangulation. The object is illuminated from one direction with a laser lime projector and viewed with the camera from another one. Laser and camera are fixed on the robot. The relief model of the device under test is acquired by translating the positioning system along the x-axis of the robot. Z-data provided by the camera are recorded on a computer and converted into probe coordinates. Finally, these data are used to position the probe over the device under test during electromagnetic measurement. The low noise amplifier having a gain of 37dB is associated with the arm of the robot.

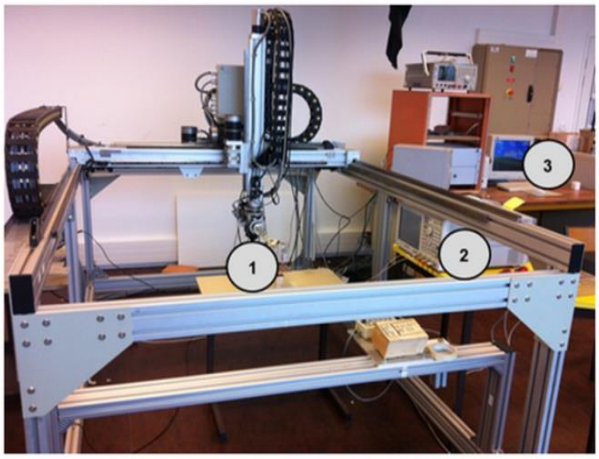

Figure 3-3Near field test bench

Reference circuit

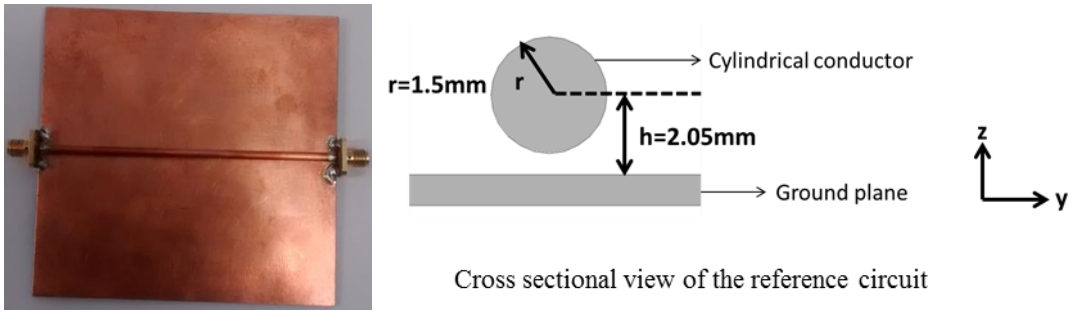

Figure 3-4 Fabricated reference circuit and its cross section

In order to make the validations, a known wire over ground structure is taken as the DUT. Since the characteristics of this DUT are known, we call it as reference circuit in the thesis. The reference circuit and its dimensions are shown in Figure 3-4. It consists of a cylindrical conductor placed at a height h from the ground plane. The one end of the cylindrical conductor is connected to the network analyzer and the other end is terminated with a 50 Ohm matched load. A plane wave is a constant frequency wave whose wave fronts (surfaces of constant phase) are infinite parallel planes of constant peak-to-peak amplitude normal to the phase velocity vector. Since there are no maxima and minima of the fields in a plane wave excitation, a wire over the ground structure is used as the source of radiation to have more accuracy in the results, which consists of different amplitude of E and H fields along the same plane.

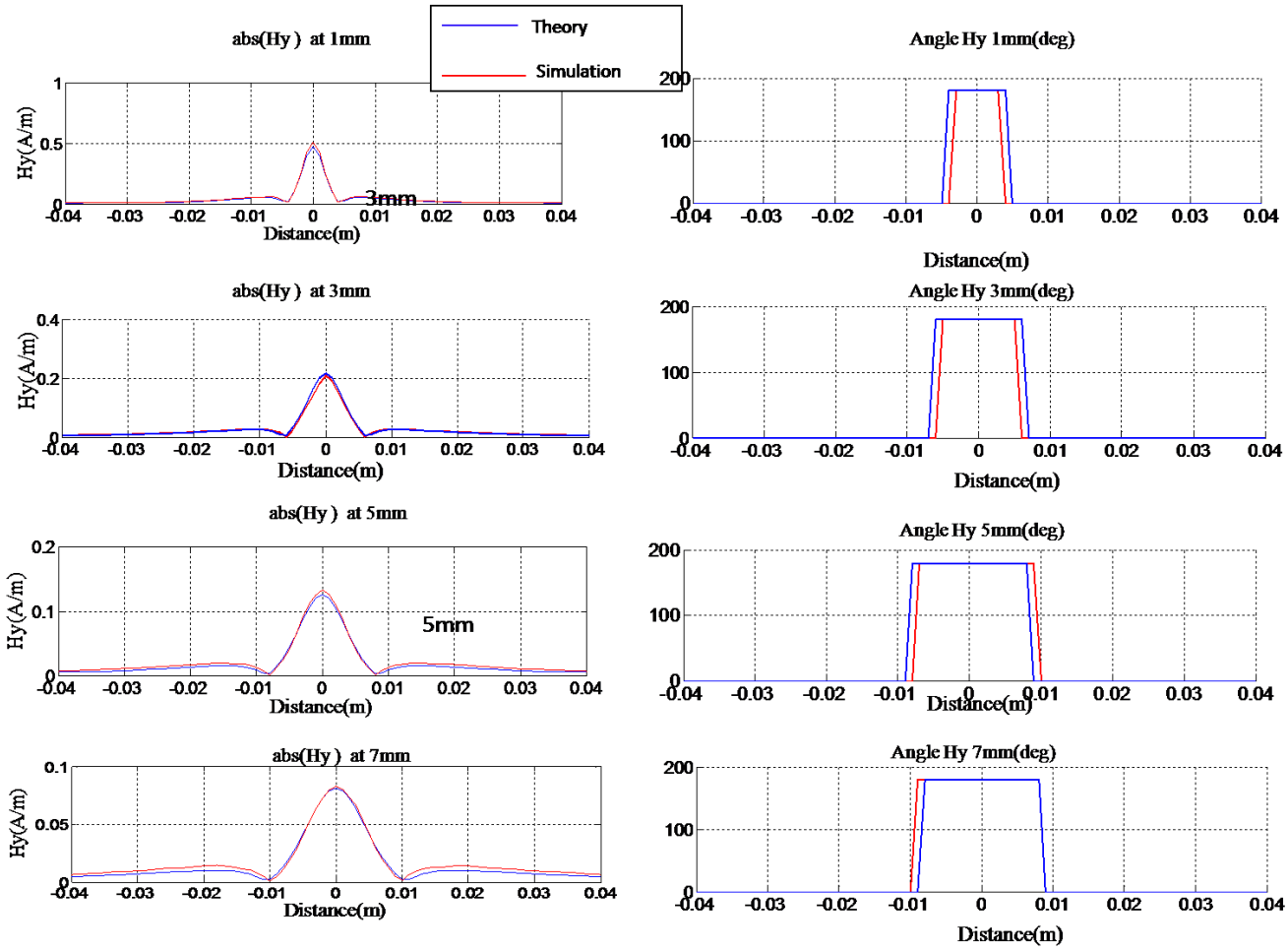

Figure 3-5The tangential component of magnetic field (Hy) at 10 MHz

The device is excited with a power of 10dBm. The expressions for the components of the electric and magnetic fields at a distance d from the cylindrical conductor is calculated by Boudry using the theory of images[1]

$$E_{y,Theory} = 8K\frac{yzn}{(y^2 + (z+n)^2)(y^2 + (z-n)^2)} \qquad 3\text{-}4$$

$$E_{z,Theory} = 4K\frac{n(y^2 - z^2 + n^2)}{(y^2 + (z+n)^2)(y^2 + (z-n)^2)} \qquad 3\text{-}5$$

$$H_{y,Theory} = -\frac{1^E}{\eta} z \qquad 3\text{-}6$$

$$H_{z,Theory} = \frac{1^E}{\eta} y \qquad 3\text{-}7$$

Where,

$$\eta = \frac{\mu_0}{\varepsilon_0} \quad , \quad K = \frac{\sqrt{2PZ_c}}{ln\left(\frac{h+n}{h-n}\right)} \text{and } n = \sqrt{h^2 - a^2}$$

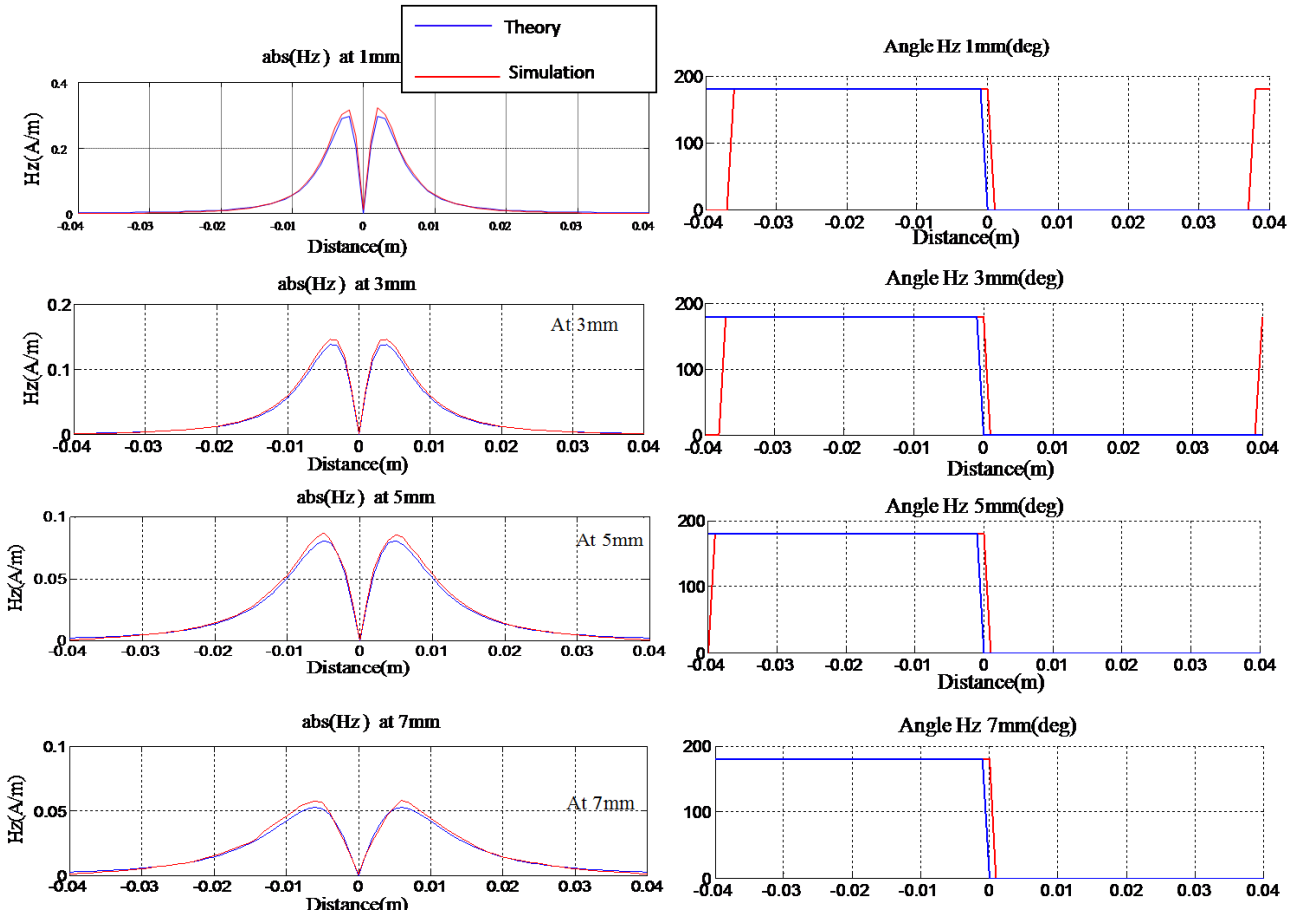

Figure 3-6The normal component of magnetic field (Hz) at 10MHz

The amplitude and phase of the magnetic field components at different heights from the cylindrical conductor and different frequencies are simulated and compared with the theoretical values in order to have good knowledge of the fields and estimate the performance of the probe. The tangential component of the magnetic field is the field along the y-axis and the component is the field along the z-axis. Figure 3-5shows the tangential (Hy) component of the magnetic fields at 10 MHz and Figure 3-6shows the normal component of the magnetic field (Hz) at 10 MHz.

3.4 Printed magnetic field probes

An ideal magnetic probe is only a loop. But, in reality, this configuration is not possible, because it requires an interface to carry the voltage induced at the probe to the receiver system. A printed circuit magnetic probe consists of a loop and a transmission line followed by the loop as shown in the schematic in Figure 3-7.

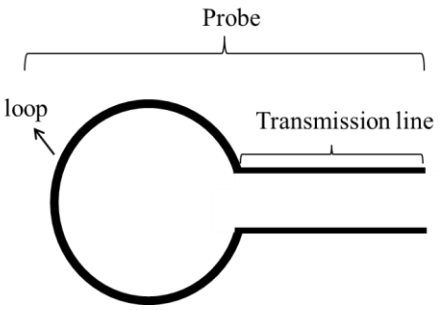

Figure 3-7Schematic of a probe

In this chapter, we have studied different probes with a different type of transmission lines. The first studied configuration is a loop with a microstrip line as the transmission line at the output of the probe. Later, a loop with a coplanar waveguide (CPW) transmission line at the output, and finally, shielded magnetic probes with stripline as the transmission line.

Type 1 loop with microstrip transmission line

Type 2 loop with CPW transmission line

Type 3 shielded magnetic probes

3.5 Printed circuit probes type 1 (with microstrip line)

In order to study the characteristics of the printed circuit probes, a rectangular loop probe is designed and simulated. The first studied configuration is a double layer double turn loop with a dimension of 3mm x 3mm named as MP-1. It is designed using the simulation software Ansoft HFSS. The detailed structure and the geometrical parameters are shown in Figure 3-8. The probe consists of loops on 2 layers named top layer and bottom layer, with 2 turns in each layer. The choice of two turns and two layers are made to have high sensitivity, as the induced voltage increases when the number of turns of the loop increases. The width of each conductor in the loop is 0.3mm and the gap between them is 0.2mm. The probe is connected to a small transmission line of length 1mm and width 0.3mm. The whole structure is designed in an FR4 substrate with dielectric constant 4.4 and thickness of 0.8mm, marked as ‘h’ in Figure 3-8 (c). The loops in the top and bottom layers are connected through a cylindrical metallic via of 400µm diameter. The simulated results of this probe are given in sec 3.5.2.

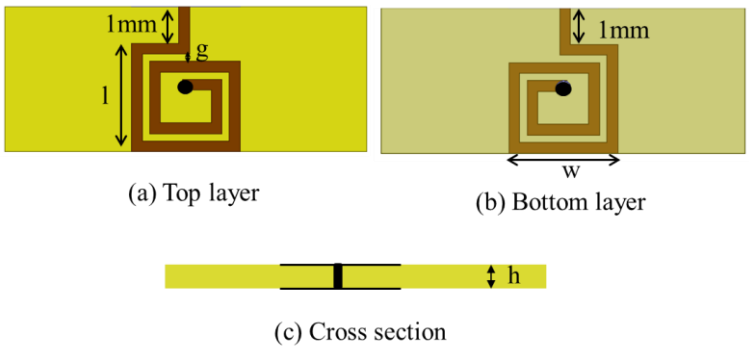

Figure 3-8 Structure and geometrical dimensions of the probeMP-1: l=3mm, w=3mm, g=0.2mm, h=0.8mm, ε_r=4.4

3.5.1 Simulation model

In order to model the behavior of the probe, the probe is placed above the reference circuit, as shown in Figure 3-9 at a distance d=3.45 mm. The distance d is measured from the top of the cylindrical conductor to the center of the loop. The end of the transmission line in the probe is assigned port 1, which is a lumped port with 50 Ohm impedance. The device under test is also assigned 50 Ohm lumped ports at both the ends.

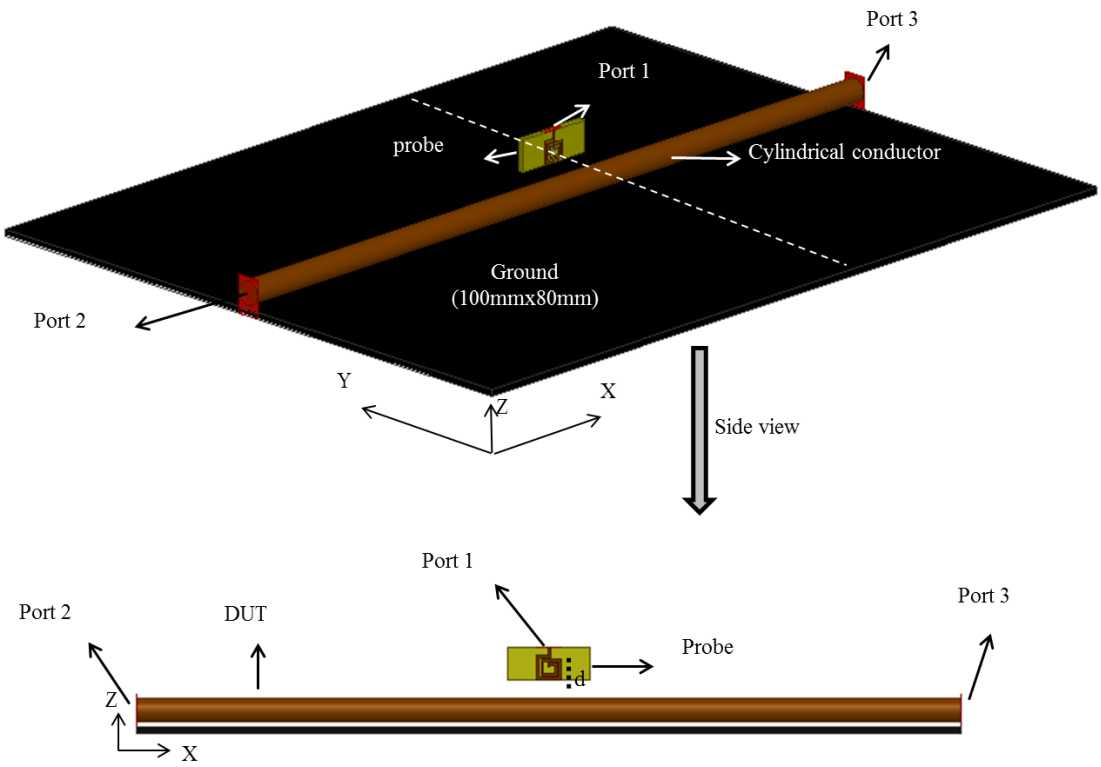

Figure 3-9 Simulation model of the probe above the reference circuit (view from HFSS)

The probe is moved along the y-axis as shown in dotted lines in the figure, keeping the reference circuit fixed. The Port 2 is assigned a power of 10 dBm. The scattering parameter S12 gives the

ratio of the voltage at port 1 to the voltage at port 2, that is, the ratio between the voltages at the probe and the input voltage. Knowing the input power at port 2, the voltage induced at the probe can be calculated.

$$V_p = \frac{S_{12}}{V_{in}} \qquad 3\text{-}8$$

Where, V_p is the output voltage of the probe, and V_{in} is the input voltage at the port 2 of reference circuit.

3.5.2 Simulated results

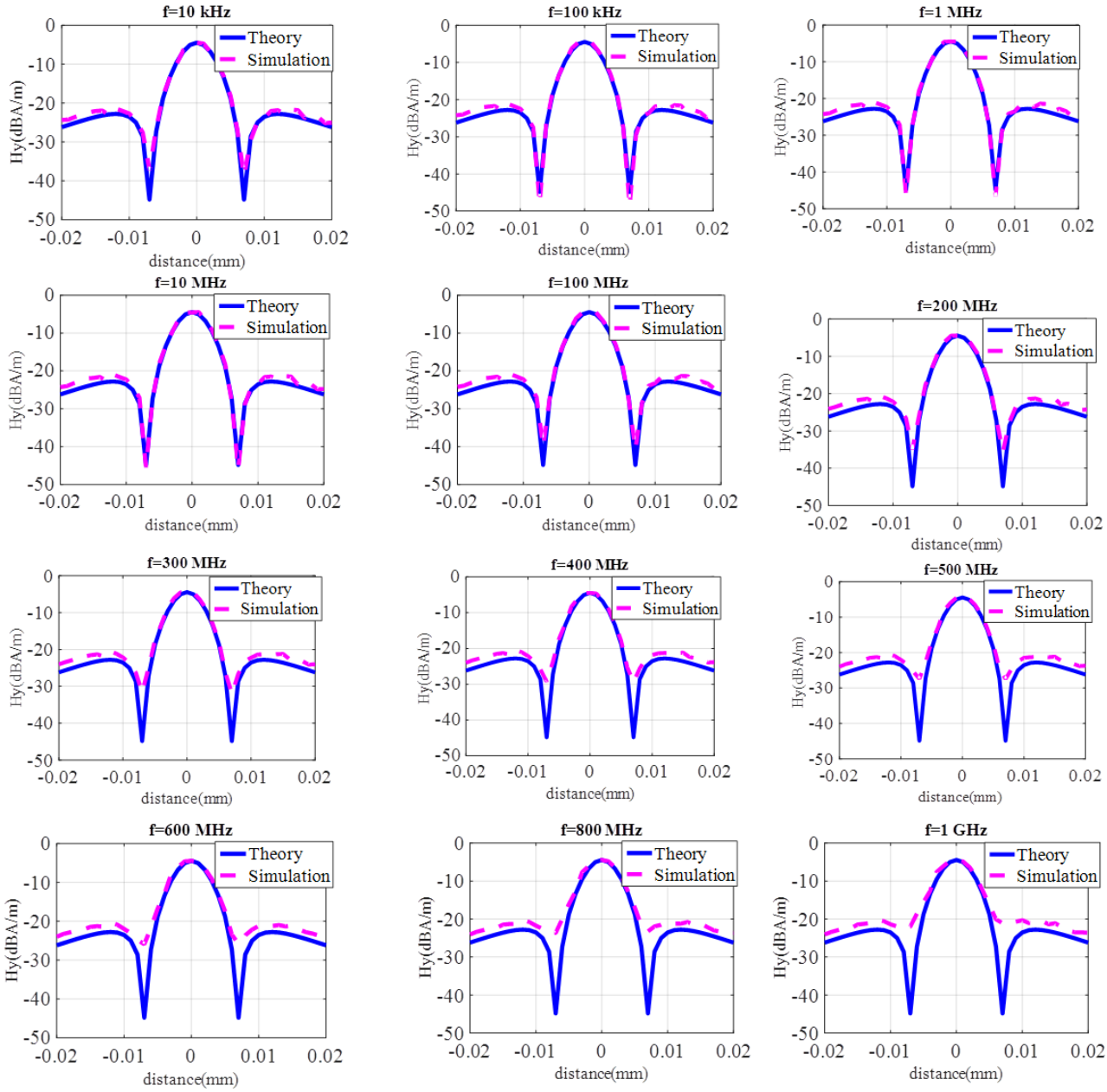

Figure 3-10 Simulations results of the magnetic field measured by the probe MP-1 at different frequencies

The simulation results of the probe in Figure 3-8are plotted in Figure 3-10 along with the original magnetic fields present at the same position of measurement, which is obtained using the analytical equation (3-6). The measured H field of the probe is calculated by multiplying Antenna Factor (AF) or Calibration Factor (CF) with the output voltage of the probe. The comparison is made at different frequencies from 10 kHz - 1 GHz. From the figure, it is seen that the probe detected the profile of the magnetic field in all the frequencies from 10 kHz-1 GHz. The received magnetic field is in very good agreement with the theoretical magnetic field from 10 kHz – 200 MHz. All the peaks are detected perfectly in this frequency band. At frequencies above 200 MHz, we can see that the detected magnetic field has the shape of the original magnetic field, but the two minima at the side lobes couldn't reach up to the level of the original field. It is also being observed that as the frequency increases, the level of the detected minima reduces. At 300 MHz, the detected minimum level of the magnetic field was 30dBA/m, at the same time, the detected minimum decays to -22 dBA/m at 1 GHz. The reason for this behavior is investigated in the following sections. As the probe consists of a loop and transmission line, the parameters considered for analysis are the effect of the structure of loop and the effect of the transmission line.

3.5.3 Effect of the structure of loop

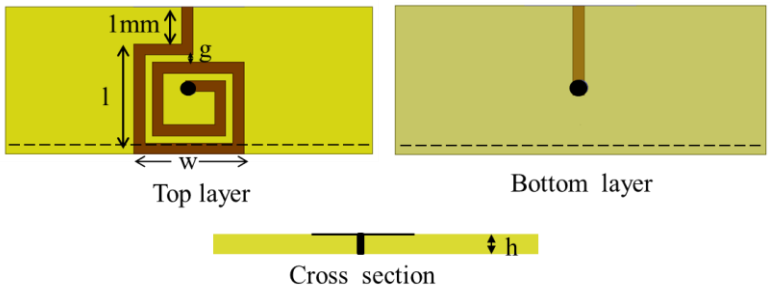

(a) MP-2

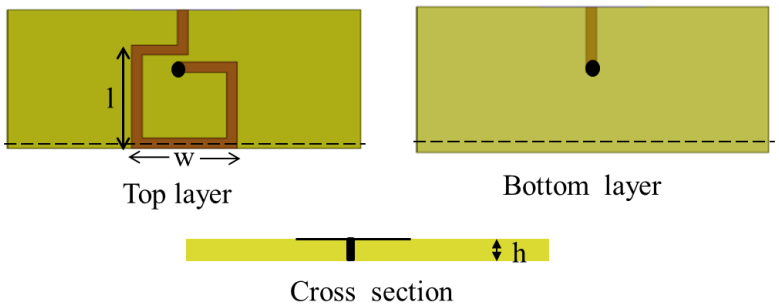

(b) MP-3

Figure 3-11 Structure of the probes (a) single layer double loop probe: MP-2 (b) single layer single loop probe: MP-3 l=3mm, w=3mm, g=0.2mm, h=0.8mm, εr=4.4

In order to understand the effect of the number of turns of the loop on the parameters of the loop (sensitivity, selectivity, and frequency bandwidth) the following two configurations of the loop is analyzed.

MP-2: Single layer double loop

MP-3: Single layer single loop

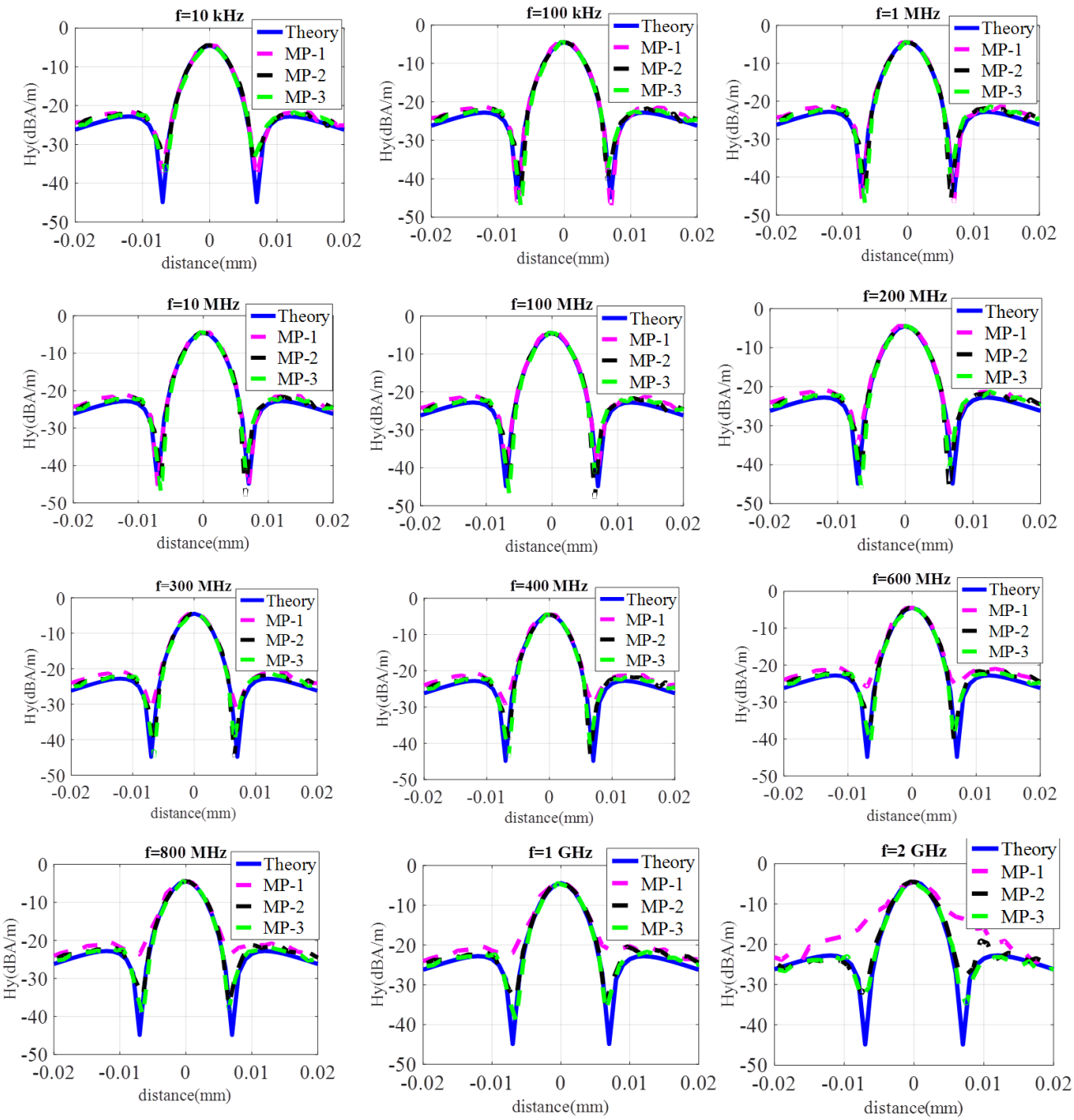

Figure 3-12Comparison of the tangential magnetic field received by the probes MP-1, MP-2 and MP-3 at different frequencies

In the first configuration, the loop in the bottom layer of the double layer probe MP1 is removed, and it results in a probe with a double turn loop on the top layer and connected to the transmission line in the bottom through a metallic via. The probe is named as MP-2 and is shown in Figure 3-11 (a). In the second configuration, there is only a single loop on the top layer of the same substrate. The probe is named as MP-3 and shown in Figure 3-11 (b). The tangential magnetic field measured by MP-2 and MP-3 is compared with MP-1 in Figure 3-12. It is quite obvious that, unlike MP-1, the detected magnetic field profile of MP-2 and MP-3 is in good agreement with the theoretical magnetic field in all frequencies from 10 kHz – 1 GHz. The minimum of the magnetic field is detected correctly in this frequency band. Therefore, the probes MP-2 and MP-3 can be said to be more selective than the probe MP-1. By reducing the number of layers of the loop, the selectivity of the probe is increased, which in turn increased the operating frequency bandwidth of the probe.

3.5.4 Effect of the transmission line

The performance of two probes MP-4 and MP-5 with different length of the microstrip line is studied (Figure 3-13). A microstrip transmission line of length L is connected to the loop through a tapered transition. The impedance of the microstrip line is made to be 50 Ohm. The probe MP-4 has a length L=6.7 cm, and the probe MP-5 has a length L=14cm.

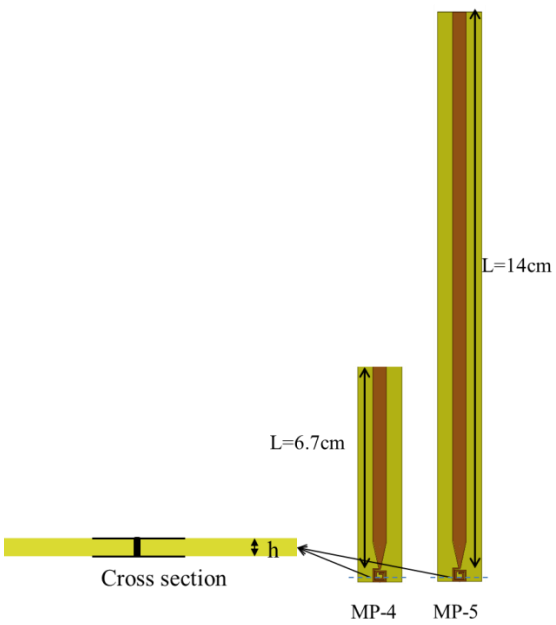

Figure 3-13Effect of transmission lines of the probes MP-4 and MP-5

The simulated tangential magnetic field of the probes MP-4 and MP-5 are compared in Figure 3-14 along with the magnetic fields of MP-1 in the frequency range of 10 kHz to 1 GHz. With the addition of the microstrip line at the loop, output has reduced the operating frequency band of the

loop. With a small 1mm line, MP-1 was able to detect the magnetic fields up to 200 MHz. However, with the addition of the line, the minimum of the magnetic field is not detected correctly from 100 MHz with MP-4 and MP-5. The profile of MP-5 at frequencies above 500 MHz is very much affected by noise than MP-4. This shows that the probe output contains the voltage induced in the loop and the voltage induced on the transmission line, which can be called as noise. These noise voltages corrupted the frequencies above 100 MHz. When the length of the transmission line increases, the highest operating frequency of the probe is reduced.

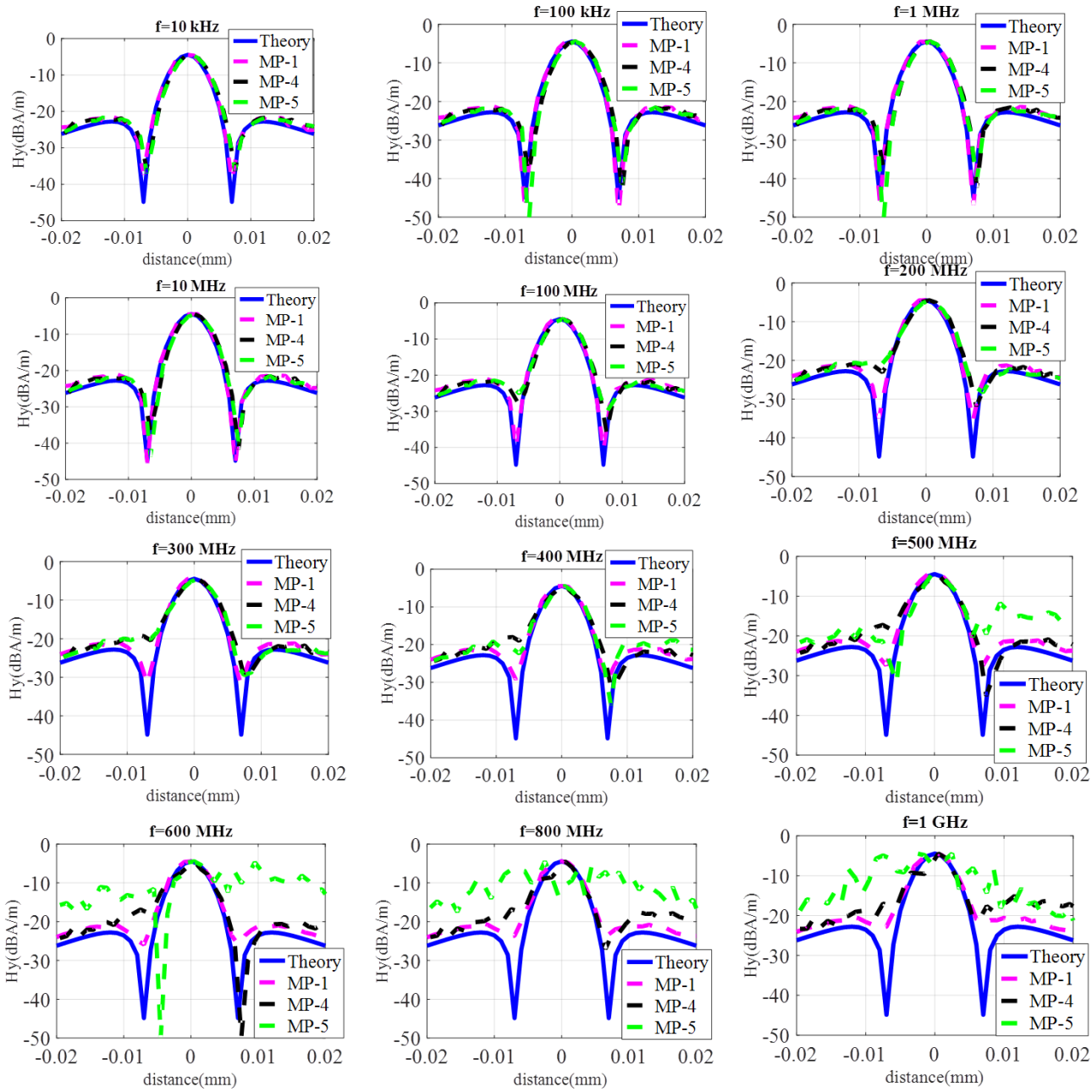

Figure 3-14 Simulations results of the magnetic field measured by the probe MP-1, MP-4, and MP-5 at different frequencies

The features of all the microstrip probes are tabulated in Table 3-1 along with its simulated operating frequency bandwidth. It is obvious from the table that when the number of layers of the loop increases, the frequency bandwidth reduces. Also, the number of turns of the loop is inversely proportional to the frequency bandwidth. It is also noted that the frequency bandwidth reduced with the increase in the length of the transmission line connected to the probe.

Name of the probe	Loop size	Number of layers In the loop	Number of turns in a layer	Line length	Simulated operating frequency bandwidth
MP-1	3mm x 3mm	2	2	1mm	<800MHz
MP-2	3mm x 3mm	1	2	1mm	>2GHz
MP-3	3mm x 3mm	1	1	1mm	>2GHz
MP-4	3mm x 3mm	2	2	6.7cm	<100MHz
MP-5	3mm x 3mm	2	2	14cm	<100MHz

Table 3-1 Comparison of different microstrip probes

3.5.5 Characterization of microstrip probes

The probe MP4 is characterized in the frequency range of 30 KHz-1GHz. The measured tangential magnetic field Hy of the probe is plotted in Figure 3-15 by applying the antenna factor.

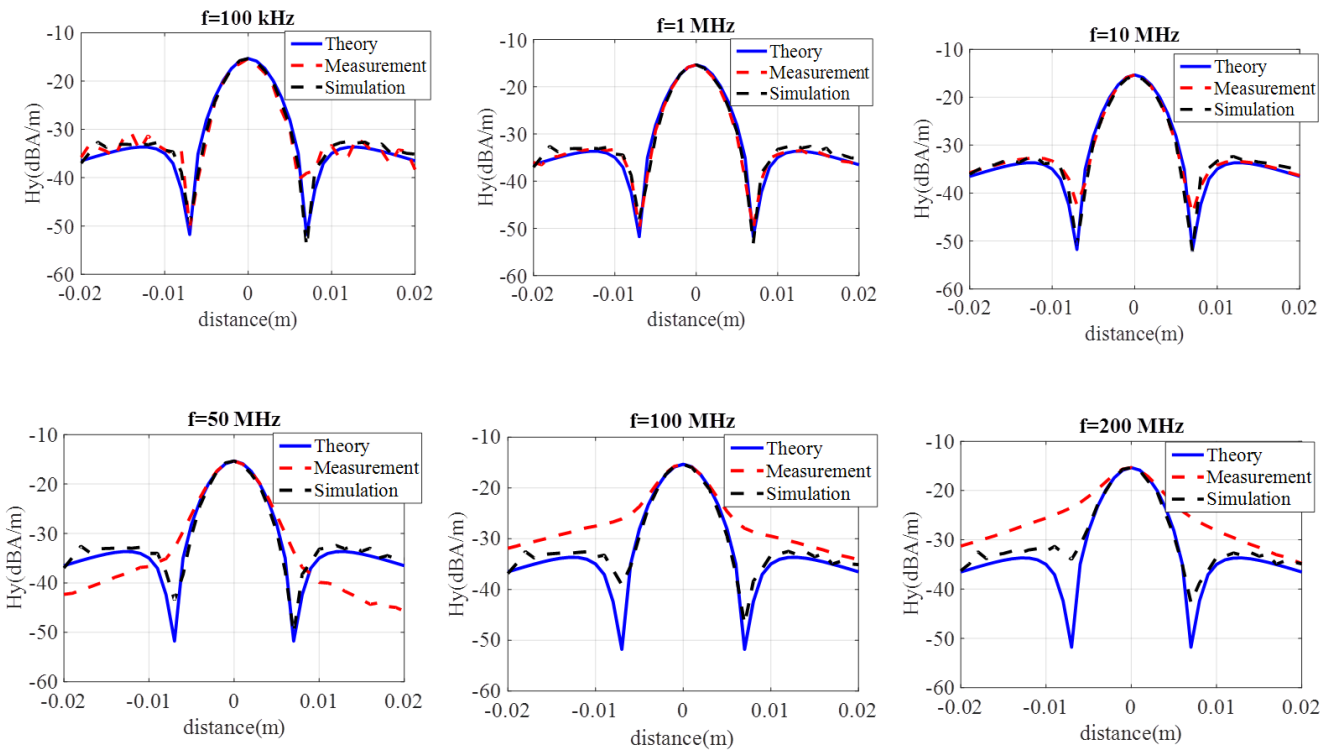

Figure 3-15 Measured tangential field components of the microstrip probe at different frequencies

The measured results are plotted along with the theoretical fields and the simulated response of the probe. An external amplifier which has a gain of 37 dB is connected at the probe output during characterization. The amplifier operates in the frequency range of 30 k Hz-200M Hz. The near-field

test bench shown in Figure 3-4 is used for the characterization. The fields are plotted from 100 KHz, as the probe is not able to detect signals below 100 kHz. The probe has a good profile up to few MHz, and when it reaches around 50 MHz, the shape of the detected profile is lost. The probe is not able to detect the magnetic field minimum positions above 50 MHz, even though the profile of the probe is good up to 100 MHz in the simulation. So, in the measurement, there are some factors other than the electric field which cause the deviation from the ideal response. The reasons for this behaviour is investigated in the following sections.

3.6 Printed circuit probes type 2 (with CPW line)

The designed and characterization of probes based on coplanar waveguide (CPW) configuration is presented in this section. A new probe with Grounded CPW (GCPW) transmission line is proposed and compared with the conventional probe with CPW transmission line

3.6.1 Coplanar waveguide (CPW) design

Coplanar waveguide (CPW) is an alternative to microstrip and stripline that places the signal and ground currents on the same layer. It is a printed circuit analogous to three-wire transmission line (Figure 3-16). A center strip which acts as the signal line is separated by a narrow gap from the ground plane on each side. The gap in the waveguide is usually very small and supports electric fields primarily concentrated in the dielectric. With the little fringing field in the air, the coplanar waveguide exhibits low dispersion. In order to concentrate the fields in the substrate area and to minimize radiation, the dielectric substrate thickness is usually set equal to about twice the gap width. A CPW has a zero cut-off frequency, but its low order propagation mode is quasi TEM. Some electric and magnetic field lines for the Quasi-TEM mode in CPW are indicated in Figure 3-17 in a defined cross-section and a defined time [2]. At higher frequencies, dispersion arises and the field becomes less TEM and more TE in nature. The two ground planes of the CPW must be maintained the same potential to prevent the unwanted modes from propagating. If the grounds are at different potentials, the CPW mode will become uneven, with a higher field in one gap than the other. In the CPW two fundamental modes in CPW are coplanar mode and the parasitic slotline mode. Air bridges between the ground planes have to be applied to suppress the undesired slotline mode. If wire bonds are used to connect the ground planes, the wires should be spaced one-quarter wavelength apart or less.

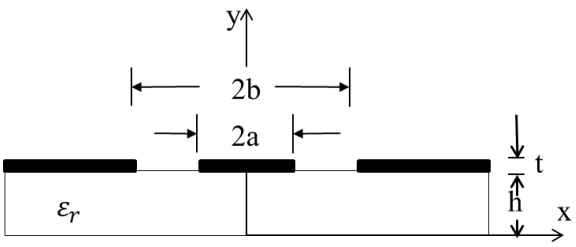

Figure 3-16 Cross section of a CPW transmission line

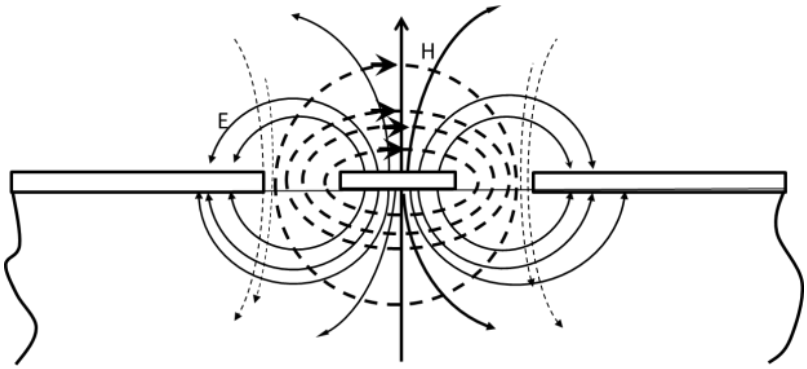

Figure 3-17 Fundamental mode – E and H field lines

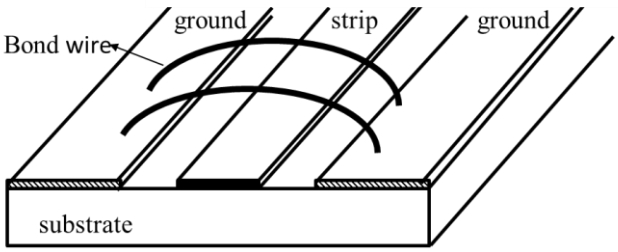

Figure 3-18 Air bridge connection between the grounds

3.6.2 Grounded coplanar waveguide (GCPW) design

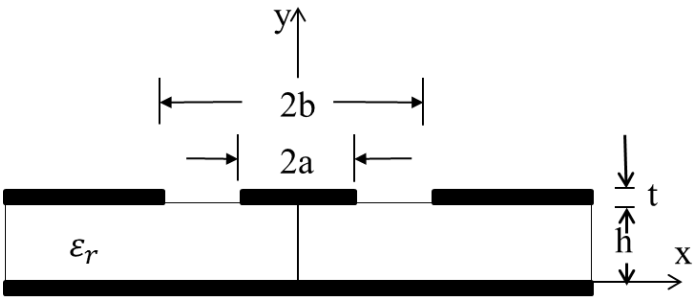

Figure 3-19 Cross section of a GCPW

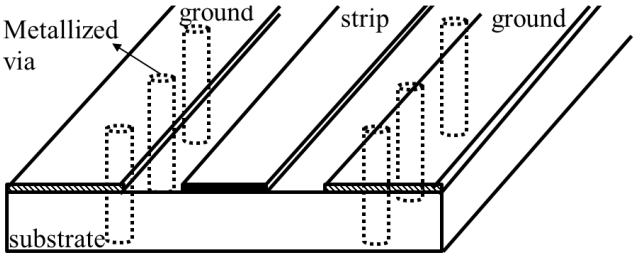

Figure 3-20 GCPW with metallic vias on the ground plane

Grounded coplanar waveguide (GCPW) or conductor-backed coplanar waveguide is a variant of coplanar waveguide, which is formed when a ground plane is provided on the opposite side of the dielectric as shown in the cross-section in Figure 3-19. With vias connecting the ground planes, GCPW is less prone to radiate and has higher isolation than microstrip (Figure 3-20).

The use of substrates with high dielectric constant, with recommended values greater than 10, the electromagnetic field is mainly concentrated inside the dielectric and avoids the field radiation in air. Spurious modes (mainly microstrip mode) can easily be generated if the separation between the CPW structure and the backing metallization is too close. The characteristic impedance is determined by the ratio of the centre strip width a to the gap width b, so the size reduction is possible without limit at the expense of higher losses.

3.6.3 Design of coplanar probes

Based on the CPW and GCPW configuration two types of probes are fabricated. The probe with the CPW transmission line is a conventional probe, which is said to operate in the frequency band of 2 GHz -7 GHz[3][4]. We have designed and fabricated the conventional CPW probe and a new GCPW probe, which has the same dimensions of the loop as in[4]. Both the probes are fabricated on Roger RO 3210, which has a dielectric constant 10.2 and thickness of the substrate h is 0.635mm. The structure of both the probes is shown in Figure 3-21.The width of the conductor of the loop is 0.5mm, and hence the aperture of each loop is 4mm x 4mm in dimension. Metallic wire bonding is provided between the grounds of the CPW probe. As the wire bond is a bridge in the air, it is easy to break and handled carefully. In order to have an equipotential ground and avoid the air bridge of the conventional CPW probe, a new configuration of probe employing a grounded coplanar waveguide is fabricated. In the GCPW probe, metallic vias having a diameter of 0.2mm are used to connect the grounds from the top to the bottom. Figure 3-22 shows the fabricated prototype of the CPW probe and GCPW probe.

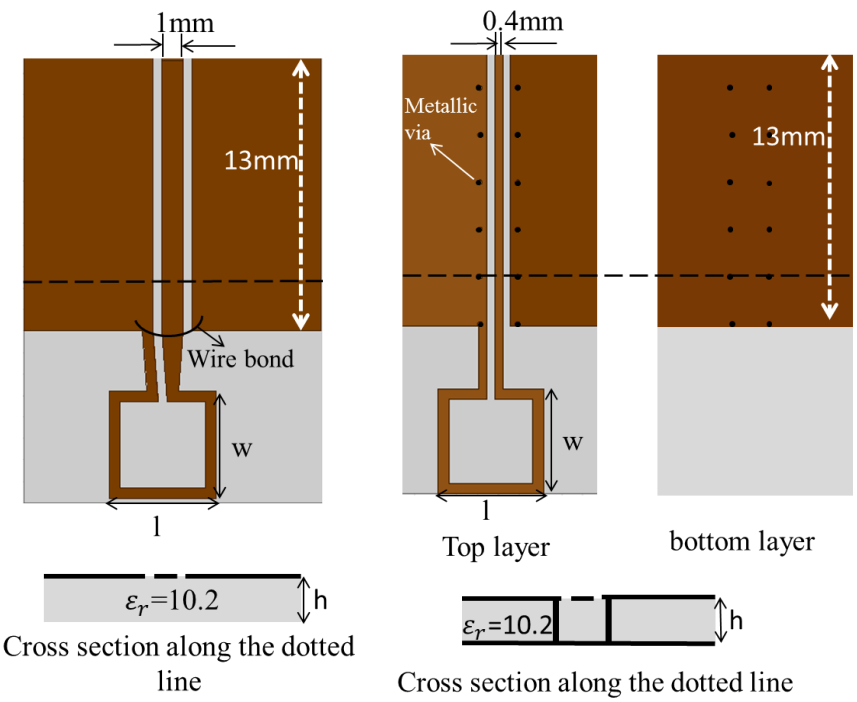

(a) (b)

Figure 3-21 Structure of the coplanar probes- simulated view (a) conventional CPW probe (b) proposed GCPW probe, l=5mm, w=5mm, h=0.635mm

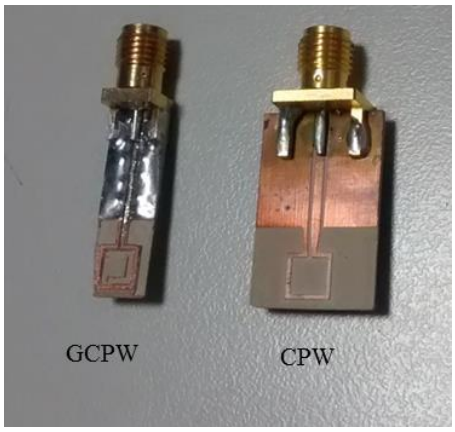

Figure 3-22 Fabricated probes with CPW and GCPW transmission lines

3.6.4 Characterization

The measured magnetic fields of both these probes at 4mm above the cylindrical conductor (d=4mm) is compared in Figure 3-23. The measurements are done without an external amplifier. Both the probes have a very bad profile at frequencies below 2 GHz. Even though, the detected profiles of GCPW probe at frequencies above 600MHz is found to be better than the CPW probe these profiles prove that the probes are not a suitable candidate for near field scan below 1 GHz.

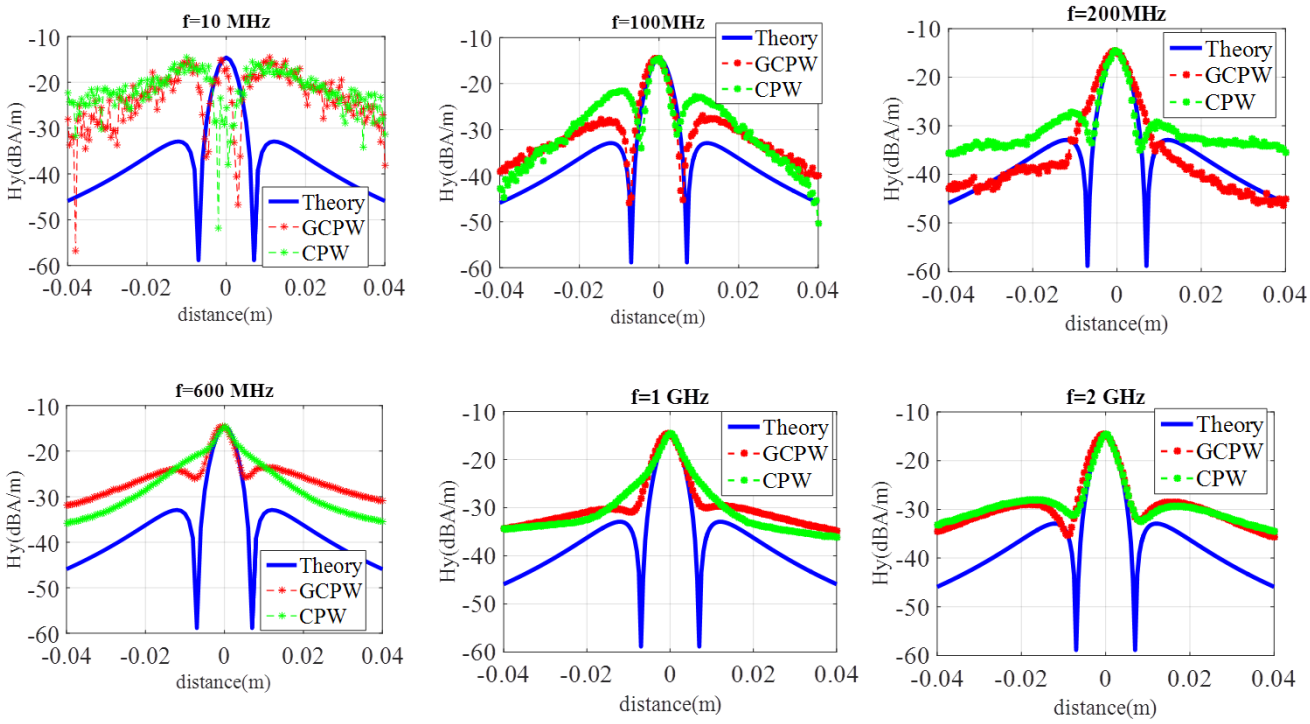

Figure 3-23 Measured tangential magnetic field components of the CPW and GCPW probes at different frequencies

3.7 Response of the loop to currents and voltages on the trace

Let us consider a simple loop placed above the cylindrical conductor in the reference circuit as in Figure 3-24. The loop is positioned in such a way to measure the tangential component of magnetic field Hy. A simple rectangular loop is connected to a coaxial cable. The current and voltage on the trace, that is, the cylindrical conductor is marked as $I_{tr}$and V_{tr} in the figure. The current in the trace I_{tr} generates the magnetic flux, which in turn induces the voltage V_{pI}in the terminals of the probe. So, we can write,

$$V_{pI} = C_I I_{tr} \qquad 3\text{-}9$$

Where,C_I is the proportionality constant.

In addition, the loop is also exposed to a vertical electric field which leads to charge redistributions on the loop and on the transmission line connected to the loop. As the field alternates, the current will flow on the loop causing a magnetic flux coupling into the loop and which in turn induces a secondary voltage V_{pV} at the probe output. At any given frequency, the induced voltage is proportional to the trace voltageV_{tr}. With a proportionality constant, the induced voltage V_{pV}

$$V_{pV} = C_V V_{tr} \qquad 3\text{-}10$$

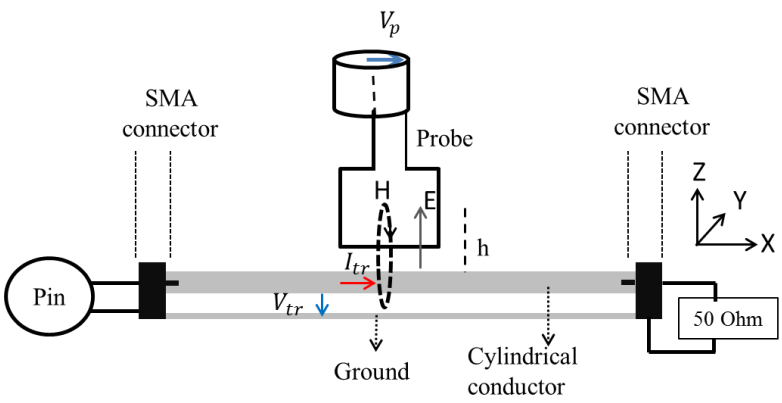

Figure 3-24 Schematic of the loop above the reference circuit

For an ideal prove C_V would be zero. In practical, it has a non-zero value. This effect can be associated with the common mode currents on the ground of the receiver or the outer shield of the coaxial cable. So, the total voltage V_p can be expressed as follows

$$V_p = V_{pI} + V_{pV} = C_I I_{tr} + C_V V_{tr} \qquad 3\text{-}11$$

C_I and $C_V$are frequency dependent complex values , which can be derived from the measurement and simulation using two different values of load impedances Z_L to the trace[5].

When referenced to the local common or ground, a common-mode signal appears on both lines of a 2-wire cable, in-phase and with equal amplitudes[6]. Such signals can arise from one or more of the following sources:

- Radiated signals coupled equally to both lines,
- An offset from signal common created in the driver circuit, or
- A ground differential between the transmitting and receiving locations.

The fundamental deviations from ideal response of the probe are related to the excitation of higher-order current modes in the loop, i.e., current distributions other than the ideal uniform current around the loop periphery. The first higher-order mode corresponds to a short electric dipole response giving rise to electric-field coupling. Any electric field present at the probe location causes a receiver response in addition to the desired pure magnetic field response. Further higher-order terms in the loop current give rise to additional unwanted responses. All these higher-order terms are related to the loop dimensions (loop radius, for a circular loop) measured in wavelengths. In the case of an ideal loop, which is isolated from ground, the worst-case plane-wave E-field to H-field coupling ratio equals twice the ratio between probe perimeter and wavelength [7]. There are quite a few literatures which treated the common mode response of the probe.

3.8 Miniaturized Shielded magnetic probe

3.8.1 Design of the shielded probe

In order to suppress these common mode currents due to the electric field, a shielded magnetic probe is designed. The structure of the probe is shown in Figure 3-25.

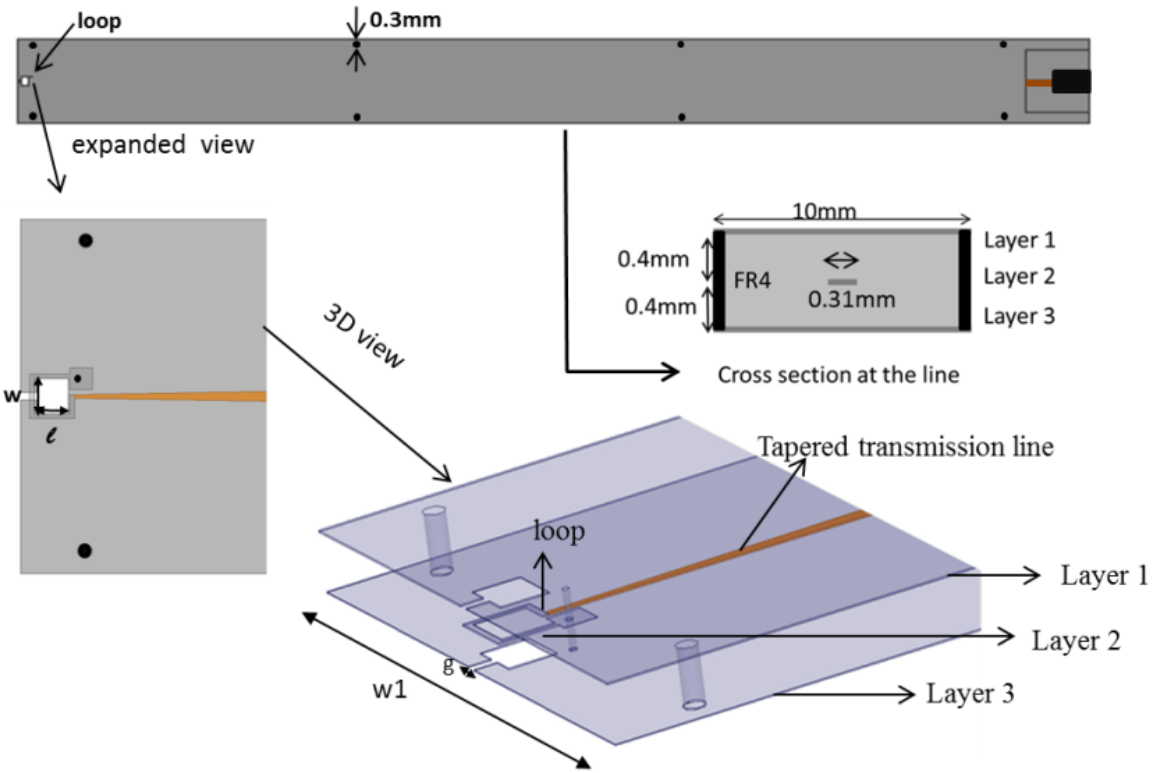

Figure 3-25 Structure of the shielded magnetic probe

The proposed probe is based on a stripline configuration. The transmission line or service line connected to the probe is a stripline which is matched to receiver impedance 50Ohm. The probe is connected to the transmission line through a tapered transition as shown in Figure 3-25. One end of the loop is connected to the hot conductor of a symmetrical stripline in the middle layer and the other end is connected to the top and bottom grounds. The shape of the probe is chosen as square, because the surface area of a square loop is larger than a circle with the same diameter as the length of one side of the aperture, and hence it increases the induced voltage of square loop probe. The length and width of the aperture (l=w) are 800µm. A shielding is extended to the part of the loop and a rectangular slot with a gap distance, g=160um is provided in order to eliminate the eddy currents on the grounds. The probe is fabricated on a standard low-cost PCB fabrication substrate Fr4 with a dielectric constant 4.4 and loss tangent 0.02. The thickness of the substrate between the top and the middle layer (h1) and between the middle layer and bottom layer (h2) is 0.4mm. The thickness of the metal in shielding layer is 18µm. The total length of the probe is made 10.5 cm

because of the length of the robot arm used to hold the probe and the width is W1=10mm. The grounds at layer 1 and layer 2 are connected by cylindrical vias of 300µm diameter at consecutive intervals in order to avoid the parallel plate mode of operation of the stripline and increase the isolation from the electric field. A rectangular metallic pad of 500µm x 500µm is provided at the end of the loop in order for the connection of via during fabrication.

3.8.1.1 Design of the transmission line

The transmission line used is a stripline structure having a strip conductor sandwiched between two ground layers [8]. A stripline is essentially a printed circuit version of a coaxial transmission line. Stripline has three layers of conductors (as seen in Figure 3-26). The internal conductor is commonly called "hot conductor". The other two conductors which are always connected to the signal ground are called the "cold conductors" or "ground conductors". The hot conductor is embedded in a homogeneous isotropic dielectric of dielectric constant $\varepsilon_{r.}$ Its dominant mode is pure TEM, assuming perfect conductors. The stripline is more suitable for use at low microwave frequencies because of the possibility of exciting parallel plate mode at higher frequencies.

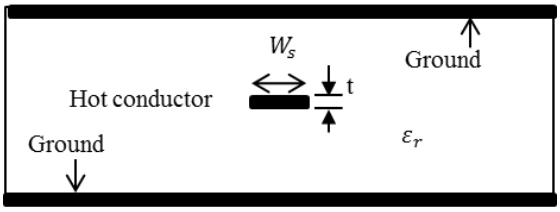

Figure 3-26 Cross section of astripline

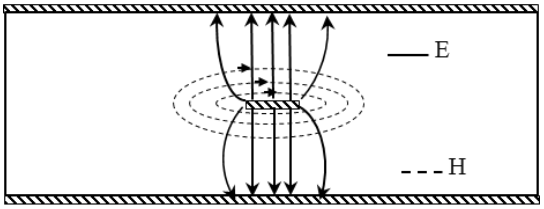

Figure 3-27 Electric E and magnetic H field lines of stripline

The electric and magnetic field lines of the strip line are indicated in Figure 3-27in defined cross-section and a defined time. As the region between the two conductor plates of stripline contains only a single medium, the phase velocity and the characteristic impedance of the dominant TEM mode do not vary with frequency. In the fundamental mode, the hot conductor is equipotential *ie.*, every point in it is at the same potential. If the top and bottom ground plates are not at the same potential, a parallel-plate mode can propagate between them. If excited, this mode will not remain confined to the region near the strip but will be able to propagate wherever the two ground planes exist.

3.8.1.2 Choice of the via and the via spacing

Striplines are less sensitive to lateral ground planes of a metallic enclosure because the electromagnetic field is strongly contained near the center conductor and the top–bottom ground planes. The return current path for a high frequency signal trace is located directly above and below the signal trace on the ground planes. The high frequency signal is thus contained entirely inside the PCB, minimizing emissions and providing natural shielding against incoming spurious signals. The metallized via holes connecting the two ground planes suppresses the parallel plate mode of the stripline. The via should be placed closely; a spacing "s" of one-eighth of a wavelength in the dielectric is recommended to prevent a potential difference from forming between the ground planes. Such vias form a cage around the strip and makes it like a basic coaxial line. When the vias are placed too close to the edge of the strip, they can perturb the characteristic impedance. The via separation 'w' should be a minimum of three-strip widths, and 5 is preferable. If the via separation is too large, a pseudo-rectangular waveguide mode can be excited. This mode has a cut off frequency given by

$$w < \frac{c}{2f_{max}} \qquad 3\text{-}12$$

Where, c is the speed of light in the dielectric. Thus, at the highest frequency of operationf_{max}, the via separation should be less than the ratio of the velocity of light and twice the maximum frequency.

3.8.1.1 Considerations for thickness of the shield

The thickness of the shield t_s is chosen to be greater than the skin depth δ of the metallic shield over the frequency range of interest.

$$t_s > \delta \qquad 3\text{-}13$$

The skin depth δ is calculated as [9]

$$\delta = \sqrt{\frac{2\rho}{\omega\mu}} \qquad 3\text{-}14$$

Where, ρ - resistivity of the conductor

ω – the angular frequency of the current

$$\mu = \mu_r \mu_0$$

μ_r – the relative permeability of the conductor

μ_0 – the permeability of free space

For copper resistivity is $\rho = 1.98 \times 10^{-8}$ Ohm meter. At 50MHz, copper has a skin depth of 9.2 µm and at 1 GHz, δ is 2 µm.

3.8.2 Equivalent circuit model

A simple circular loop isolated from the ground is used to explain the reception of the electric and magnetic field by the loop [10]. Assume that a plane wave impinges on the loop with magnetic field perpendicular to the plane of the loop and the electric field along the plane of the loop. This configuration maximizes the interaction between the loop, the H field, and E field.

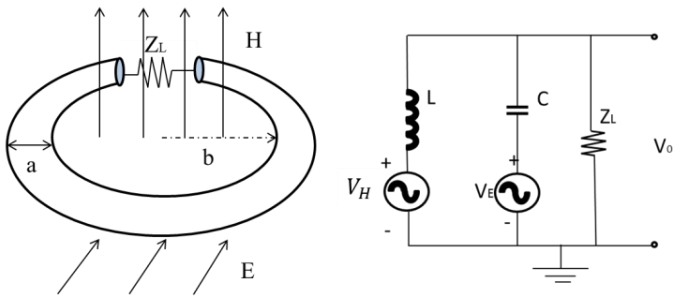

(a) (b)

Figure 3-28 (a) EM field reception; (b) simplified equivalent circuit model of the receiving loop

For this configuration, the equivalent circuit can be represented as shown in Figure 3-28, where the inductance and capacitance are calculated as follows,

$$L = \mu_0 b \left(ln\left(\frac{8b}{a}\right) - 2 \right) \qquad 3\text{-}15$$

$$C = 2\varepsilon_0 b \left(\ln\left(\frac{8b}{a}\right) - 2 \right) \qquad 3\text{-}16$$

L = self-inductance of the loop

C= self-capacitance of the loop

The radiation resistance in series with L and C is neglected in this case. Ideally pure magnetic response and first order e field response are considered.

$$V_E = \pi b E \qquad 3\text{-}17$$

$$V_H = -jw\mu\pi b^2 H,\ 2\pi b << \lambda 0 \qquad 3\text{-}18$$

The ratio of the H field response to the E field response is

$$\frac{V_{0H}}{V_{0E}} = \frac{c}{4\pi bf} \qquad 3\text{-}19$$

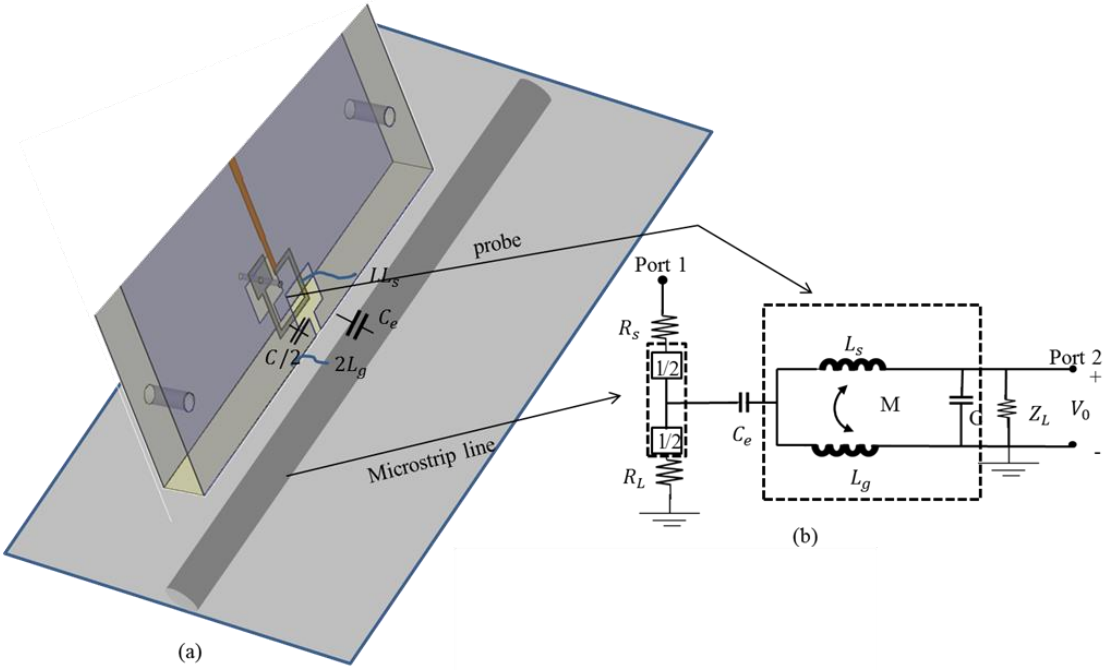

Figure 3-29 Equivalent circuit representation of the shielded magnetic probe (a) shielded probe above the microstrip trace (b) equivalent circuit (c) alternative representation

The equivalent circuit of the proposed probe when the microstrip circuit is used as the device under test can be modelled as shown in Figure 3-29.Figure 3-29 (a) shows the simulated view of the probe above the reference circuit. Figure 3-29 (b) shows the equivalent circuit representation of this configuration. $R_s$is the source impedance. $R_L$is the load impedance connected to the microstrip line. $Z_L$is the impedance of the receiving device, C_e represents the effect of the E field coupling. C is the capacitance of the loop; L_s is the self-inductance of the loop.$L_g$is the self-inductance of the ground. M is the mutual inductance [11].

3.8.3 Characterization

The results of the simulation and measurement of the probe are discussed in this section. The design of the probe is done using HFSS. The photograph of the fabricated probe is shown in Figure 3-30

Figure 3-30 Photograph of the fabricated probe SP1-A

This probe is called as SP1-A in this thesis. The measurement analysis is carried out in two configurations, (1) without an amplifier and (2) with an external amplifier between the probe and the receiving device. The distance from the center of the probe to the top of the cylindrical conductor is 1.7mm during the measurement. The external amplifier used for the measurement is a pulse amplifier ZPUL with the gain curve as shown in Figure 3-31. The noise figure of this amplifier is 7dB.

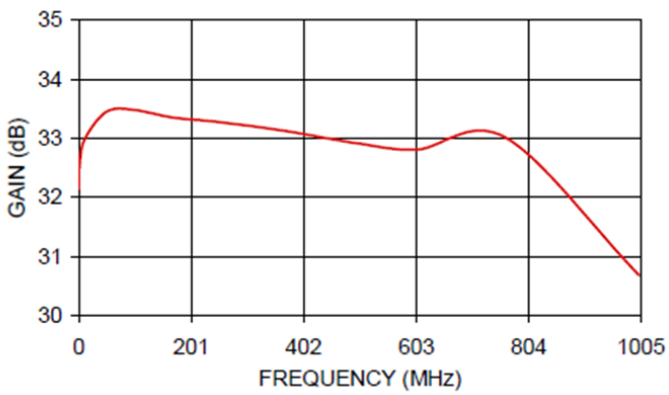

Figure 3-31 Gain curve of the amplifier ZPUL-30 [12]

3.8.3.1 *Antenna Factor*

The antenna factor of the probe is calculated using equation 3-2. The measured antenna factor is plotted in Figure 3-32 along with the simulated antenna factor of the proposed probe. The detected voltage of the probe is calculated from the S-parameters of the probe with the amplifier (ZPUL-30). The antenna factor without amplifier is then calculated by subtracting the gain of the amplifier from the measured voltage. The simulated antenna factor of the probe alone is in good agreement with the measured antenna factor of the probe without any amplifiers. With the use of the amplifier, the original antenna factor of the probe is reduced by the gain of the amplifier.

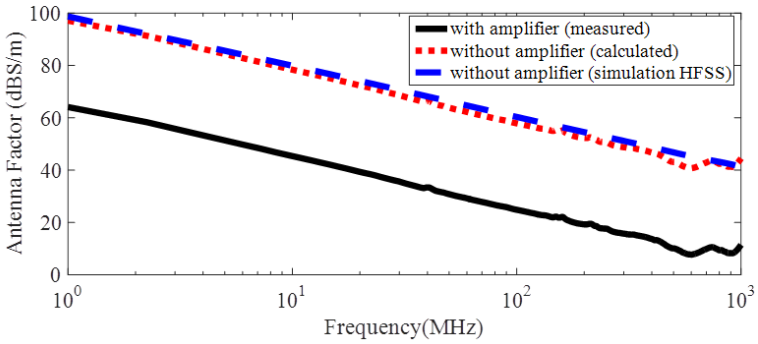

Figure 3-32 Measured and simulated Antenna factor of the probe SP1

3.8.3.2 *Sensitivity of the probe*

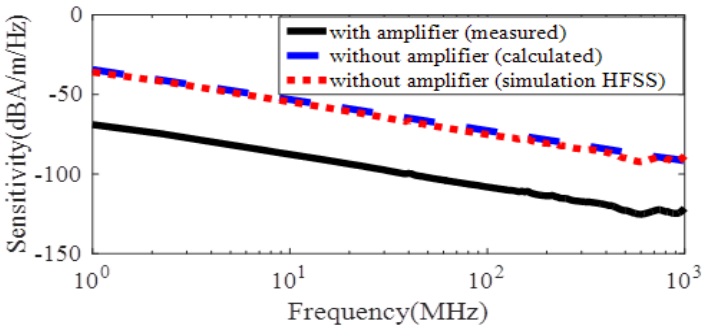

Figure 3-33Sensitivity versus frequency of the probe SP1

The minimum detectable level of the quantity to be measured by the probe is called Sensitivity of the probe. The sensitivity of the probe depends on the Noise floor of the receiving equipment and the antenna factor. Although the sensitivity of the probe change depending on the noise floor of the receiving device, the sensitivity here is calculated in Figure 3-33 for the measurements with a vector network analyzer E5071C which has a noise floor of -123dBm/Hz from 10 MHz-5 GHz. Sensitivity is calculated by multiplication of the antenna factor and the minimum detectable voltage of the receiving device, which depends on the resolution bandwidth and is calculated from the noise floor of the receiving device. The sensitivity of the probe decreases with the decrease in frequency. As is

obvious from the figure, the use of the amplifier has increased the sensitivity of the probe in the measurement.

3.8.3.3 Simulated near field scan results

The probe in Figure 3-29 is simulated above the reference circuit in order to get the magnetic field received by the probe along the y-axis. The simulated tangential magnetic field received by the probe is plotted in Figure 3-34 by applying the simulated antenna factor. The detected profile of the tangential magnetic field is in good agreement with the theoretical fields of the microstrip in all the frequencies from 10 MHz to 3 GHz. The simulated fields below 10 MHz are not plotted because the antenna facto below 1 MHz is very high and the probe is expected to have very less sensitivity.

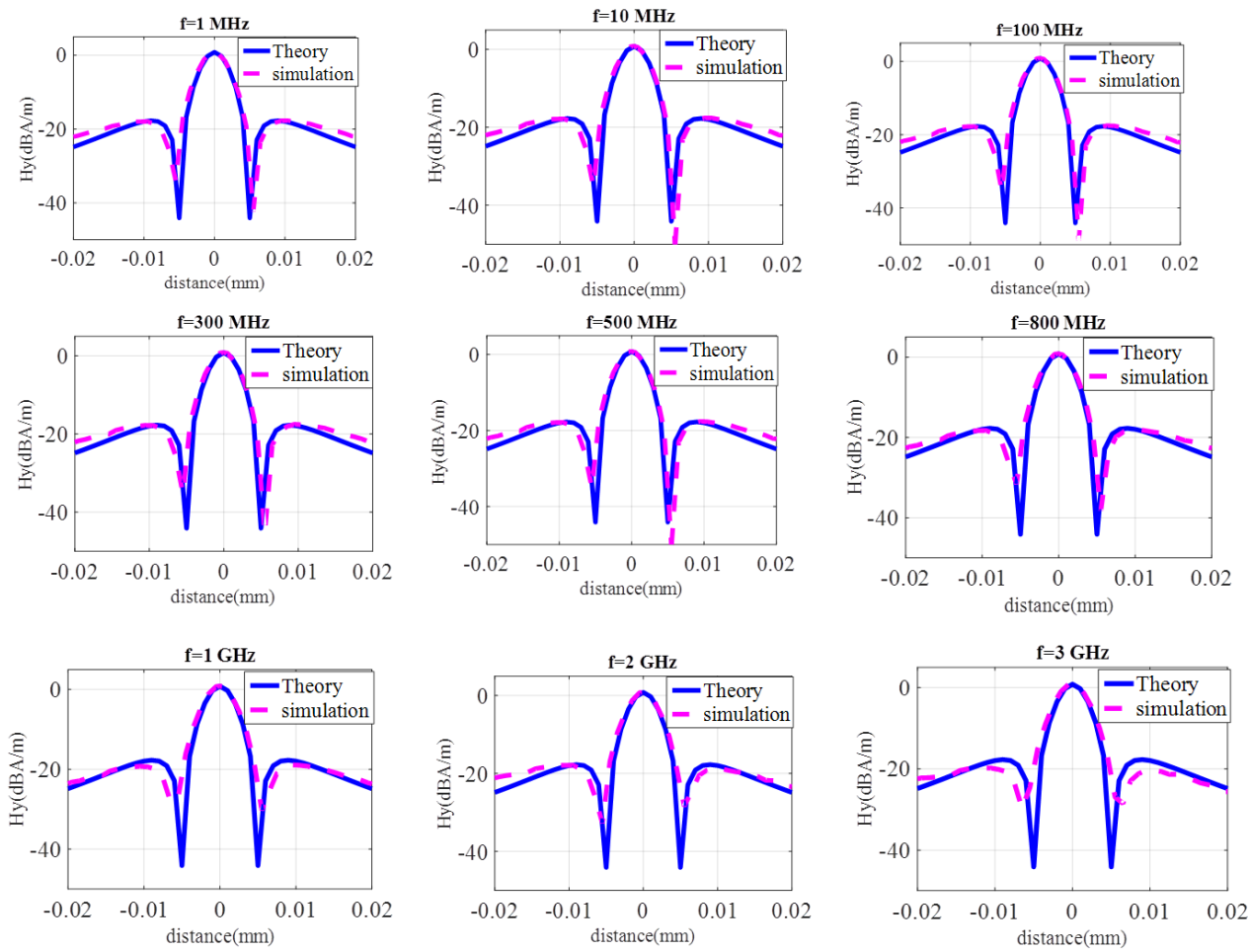

Figure 3-34 Simulated tangential magnetic field of probe SP1 at 1.7mm

3.8.3.4 *Near field scanning without amplifier*

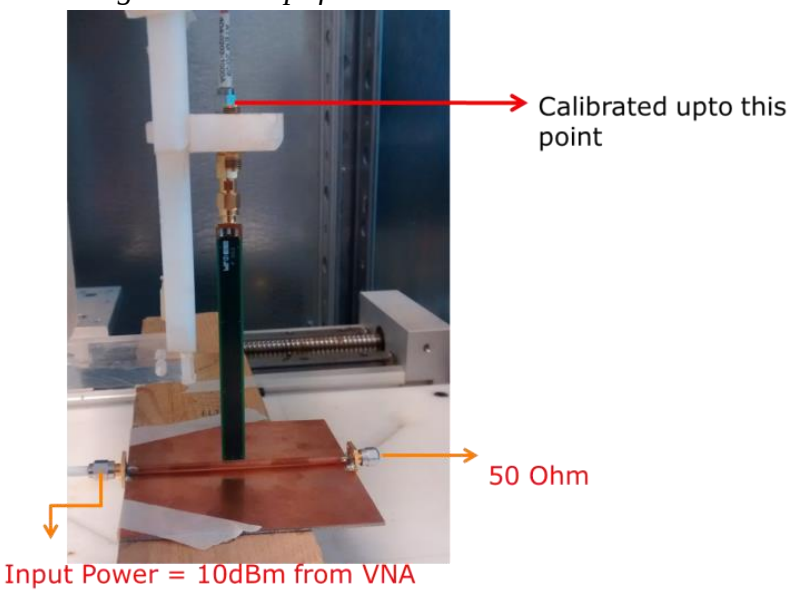

Figure 3-35Near field scanning setup without amplifier

The probe is first characterized without an amplifier ie, the probe output is connected directly to the network analyzer (Figure 3-35). The robot is moved above the microstrip along the y-axis in order to measure the tangential component of magnetic field.

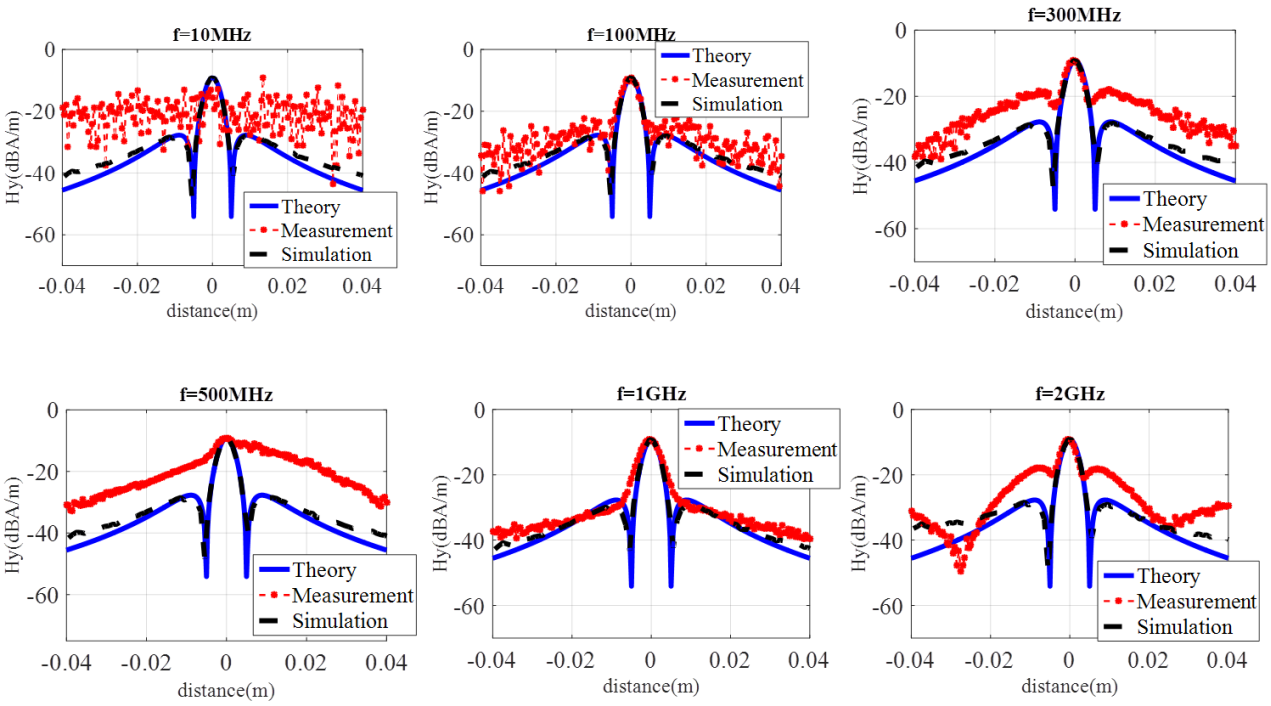

Figure 3-36 Measured tangential field received by the probe at different frequencies without any amplifier

The received tangential magnetic field at different frequencies is plotted by applying the antenna factor. From Figure 3-36, it is obvious that the detected magnetic fields are very much close to the

noise level. Measured tangential field profile of the probe is below the noise level for all positions up to 100 MHz.The levels of the minimum don't coincide with the minimum level of the theoretical magnetic field for frequencies above 100 MHz, even though the profile has a similar shape of the original magnetic field. This is because, as the dimensions of the probe are very small, the proposed probe has very less sensitivity in the entire frequency band from 1 MHz to 1 GHz and the noise floor of the vector network analyzer is very high in order to be not able to receive the signals in all positions. Even at frequencies above 1 GHz (profile at 2 GHz is shown in Figure 3-36), the detected voltage is below the noise floor of the receiver.

3.8.3.5 Near field scanning with external amplifier

In order to increase the sensitivity of the probe, an amplifier with a gain curve as shown Figure 3-31 is connected immediately at the terminals of the probe as shown in Figure 3-37.The near field scanning is again performed at the same height (at d=1.7mm).

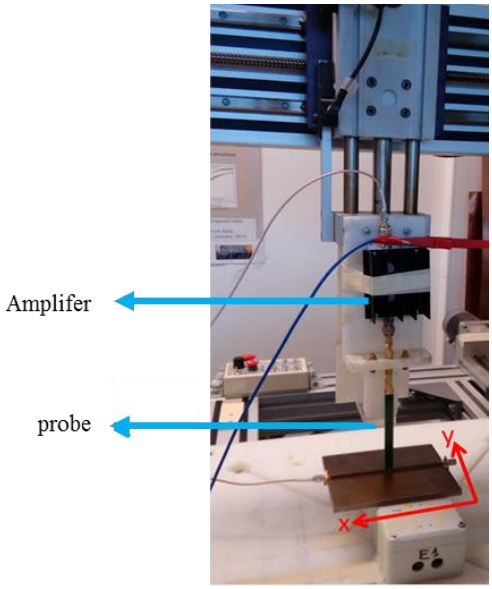

Figure 3-37Near field scanning setup with an external amplifier.

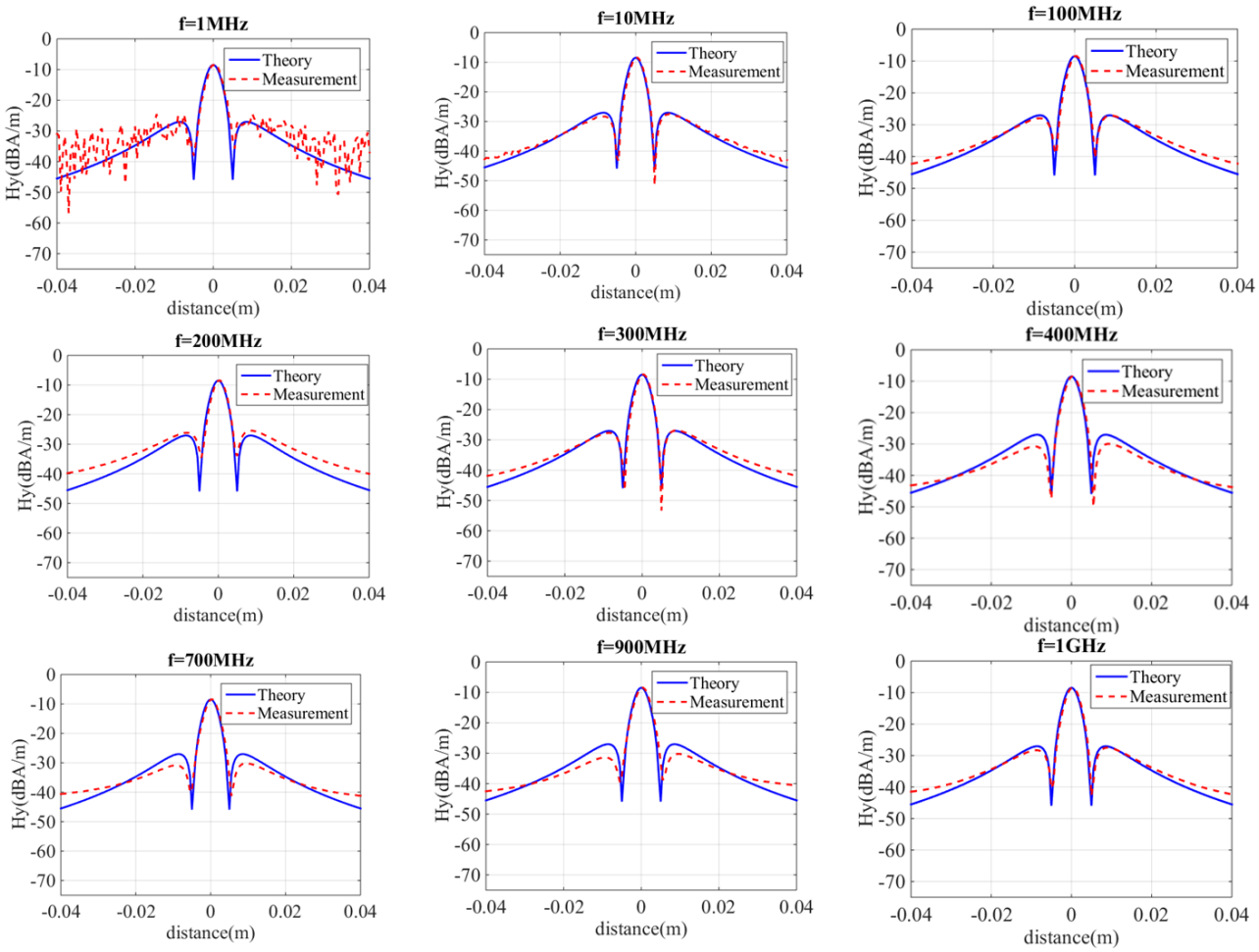

Figure 3-38 Measured tangential component of magnetic field (Hy) with amplifier

The measured tangential magnetic field component is plotted by applying the measured antenna factor in Figure 3-38. At 1 MHz, the detected field is still noisy in the positions where the field is close to the minimum level. This indicates that the 37 dB gain of the amplifier is not enough to detect the frequencies below 1 MHz. The fields are measured only up to 1 GHz because the amplifier is usable up to 1 GHz. The profile of the measured tangential field is in good agreement with the theoretical magnetic field from 10 MHz to 400 MHz. In the frequency band of 400 MHz-900 MHz, even though the maximum and minimum are correctly detected, there is a small deviation from theoretical values at the positions of the side lobes. This is expected due to the 10 cm long length of the transmission in the probe, which is not calibrated. This length of the line was unavoidable due to the length of the arm of the robot in the near field test bench.

3.8.4 Effect of the length of the probe and arm of the measurement system

In order to measure the probes with length less than 10cm, we used another scanning system because of the mechanical limitations of the length of the arm holding the probe.

3.8.4.1 An alternate near field scanning system

A scanning system has been developed at Pheline lab (at CSTB Grenoble), which consists of a robot, Teledyne LeCroy Wave Runner 640Zi oscilloscope, PC and the designed 3D H-field probes. The robot is able to move in 3-axis with a step size of 1mm. As the step size is very high, the precision of this scanning system is less compared to the one presented in the section 3.3. The scanning robot is connected to the oscilloscope to the PC. The PC is programmed to control the movement of the robot and the data collection from the spectrum analyzer. The plastic arm of the robot holds the probe above the DUT. The movement of the robot arm can be precisely adjusted to 0.1mm/step by a 3D movable controller system. The output of probe can be connected to any of the channels of the oscilloscope.

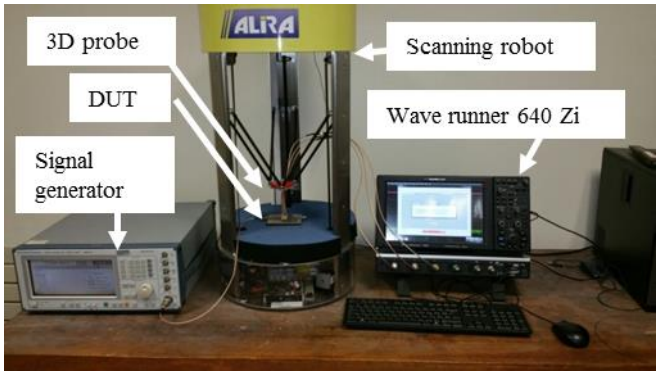

Figure 3-39 Alternate near field scanning system

3.8.4.2 Design and characterization of probe with reduced length

In order to understand the influence of the length of the arm of the measurement system in which the probe is attached, we have designed a probe with the same dimensions of the loop and with a transmission line of 1.5cm and is named as SP1-B. The fabricated probe is shown in Figure 3-40 (a).

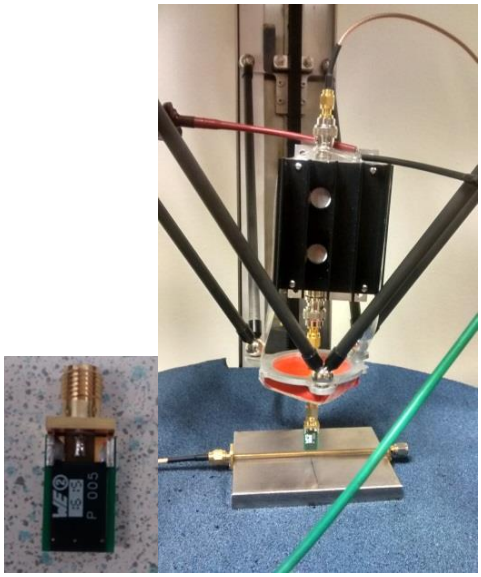

(a) (b)

Figure 3-40 Shielded probe SP1-B (a) fabricated probe (b) measurement setup

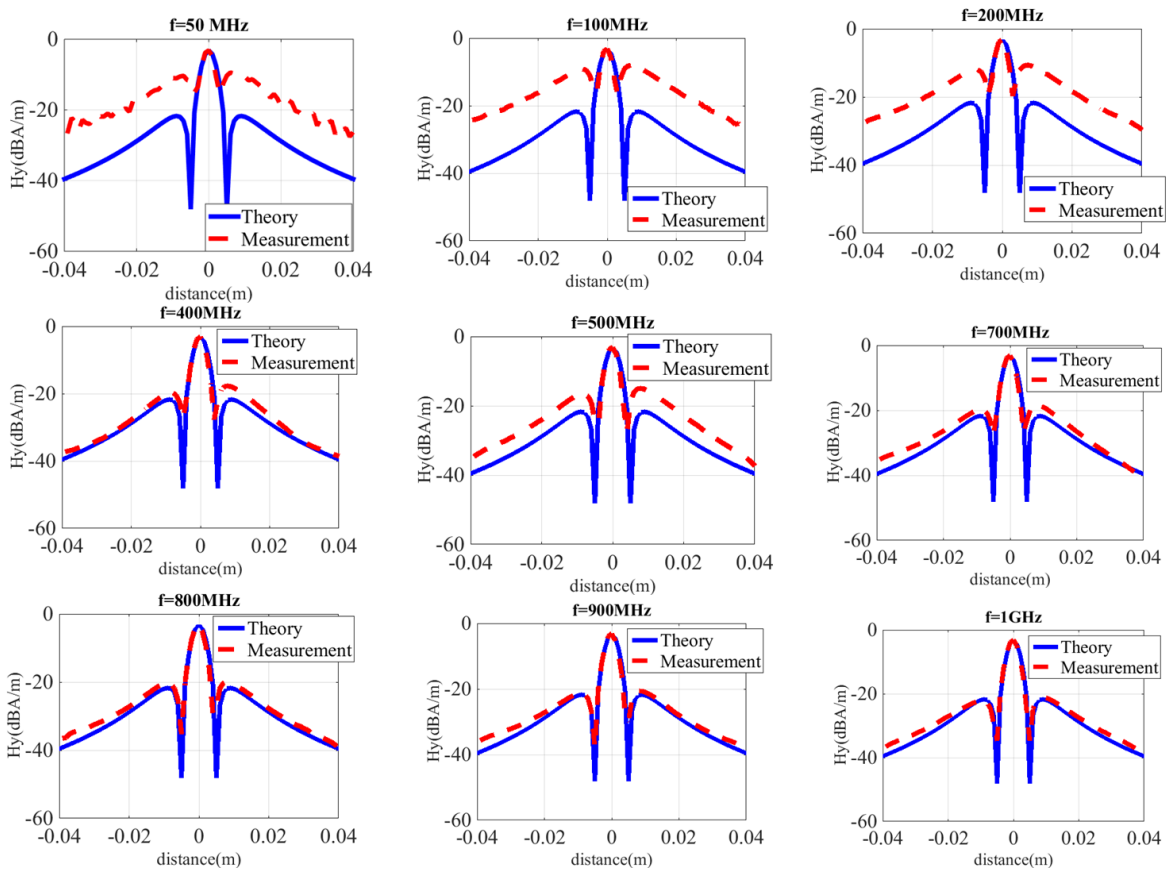

Figure 3-41 Measured tangential magnetic fields of SP1-B

It was not -possible to characterize this probe with the near field test bench discussed above unless we connect the probe to an additional length of coaxial cable or another transmission line. So, we have another near field test bench in Figure 3-39. The photograph of the measurement setup is

shown in Figure 3-40 (b). The amplifier ZPUL is connected immediately at the output of the probe. The amplified output of the probe is connected to spectrum analyzer inside the oscilloscope. Near field scanning is performed at every desired frequency. The input power from the signal generator is 10dBm. The tangential field measured by this configuration is plotted in Figure 3-41.

Unlike the probe SP1-A with a long line, the scanned profile of the probe SP1-B at frequencies above 400 MHz are in very good agreement with the theoretical field. So, it is the length of the line in SP-A which caused the small deviations from the theoretical field at some frequency band as suspected. But it is not well understood that the frequencies below 400 MHz, has deviated more from the theoretical fields in the side lobe levels, even though it preserves the shape of the profile.

3.9 Design and characterization of3 axis magnetic field probes

It is necessary to have all the 3 components of magnetic or electric fields for accurate prediction of radiated emissions [13]. But it requires a large scanning time in order to complete one surface of a PCB during the near field measurements. In [14] a 3D near field scanner for IC chip level measurements is proposed. It consists of 3D near field scanner with a magnetic probe head. Two separate magnetic fields probe (to measure the normal and tangential component of the magnetic field) for measuring three-dimensional fields in high frequency planar circuits is proposed in [15]. Still, these methods don't reduce the scanning time because each component has to be measured separately. In order to minimize the scanning time, we propose a three dimensional (3D) scanning system consisting of a near field scanner and a three-axis probe which measures the three components of the magnetic field at the same time. Jomaa has already realized a scanning system with a 3-axis probe consisting of conventional circular loops [16]. These probes suffer from having a poor spatial resolution because of its larger size and are also difficult to fabricate manually. The proposed 3-axis probe is a printed circuit magnetic probe which has 3 loops printed inside a substrate in order to measure the three components of the magnetic field simultaneously.

3.9.1 Design and characterization

3.9.1.1 Structure of the probe

The 3 axis printed circuit probe consists of 3 rectangular loops oriented in 3 different directions X, Y and Z. Every single loop is designed to measure one component of magnetic field. Figure 3-42 shows the fabricated 3-axis probe along with the 3D view. The 3-axis printed circuit probe consists of 3 loops oriented in 3 different directions X, Y and Z. The loop oriented in the y-direction measures the x component of the magnetic field and the loop oriented along the x-direction measures the y component of magnetic field. The loop in the XY plane measures the normal component of magnetic field.

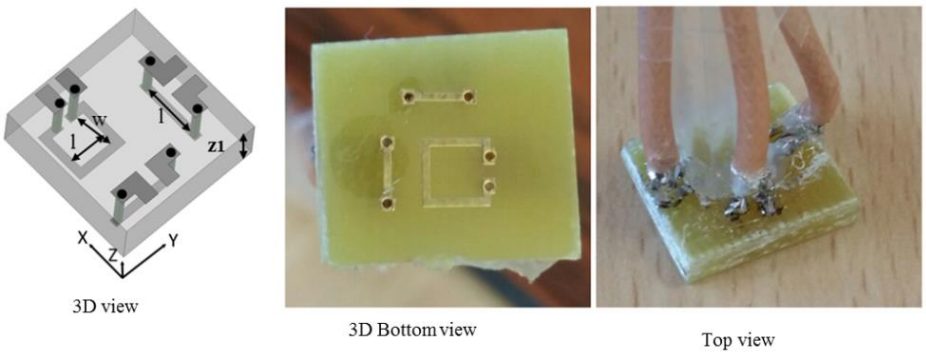

Figure 3-42*Structure of the 3 axis probe, l* = w = z1= 3.2 mm

Each loop having a dimension of 3.2mm x 3.2mm is fabricated on both sides of an FR4 substrate with a thickness of 3.2mm. The probe has an overall dimension of 0.9mm x 0.9mm x 3.2mm. In order to form loops on the X and Y directions, top and bottom conductors are connected through a cylindrical via having a radius of 500 µm. The connecting pads for all individual loops are provided at the top surface in order to be able to connect it to the coaxial cable.

3.9.1.2 Calibration

The calibration setup used in this work is shown in Figure 3-43 FCC-TEM-JM1 cell was used to produce calculable electric and magnetic field strengths. It operates in the transverse electromagnetic mode so that both the E and H-field components generated between the septum and outer conductor have the characteristics of a wave propagating in free space. The field strength can be calculated from the dimensions of the cell, its impedance at the measurement plane and the input power as shown in the equations below [17]:

$$E_z[V/m] = \frac{\sqrt{2Z_c P_{in}[watt]}}{h_{tem}[m]} \qquad 3\text{-}20$$

$$H[A/m] = \frac{E[V/m]}{\eta[\Omega]} \qquad 3\text{-}21$$

Where Z_c is the input impedance of the measuring instrument in Ohm

$P_{in}$is the input power in watts

$h_{tem}$is the distance in meters between the septum and the outer conductor of the TEM cell

$\eta$is the intrinsic impedance of the free space in ohms.

The antenna factor then can be calculated by placing the probe inside the TEM cell and measuring the induced voltageV_{ind}across the loop terminals, according to the following equation:

$$AF\left[dB\frac{A/m}{V}\right] = 20\log\left(\frac{H[A/m]}{V_{ind}[V]}\right) \qquad 3\text{-}22$$

Where V_{ind} is the induced voltage in the loop (in volts) and it is given by:

$$V_{ind} = \sqrt{2Z_c|S_{21}|^2P_{in}}[watt]e^{j.arg(S_{21})} \qquad 3\text{-}23$$

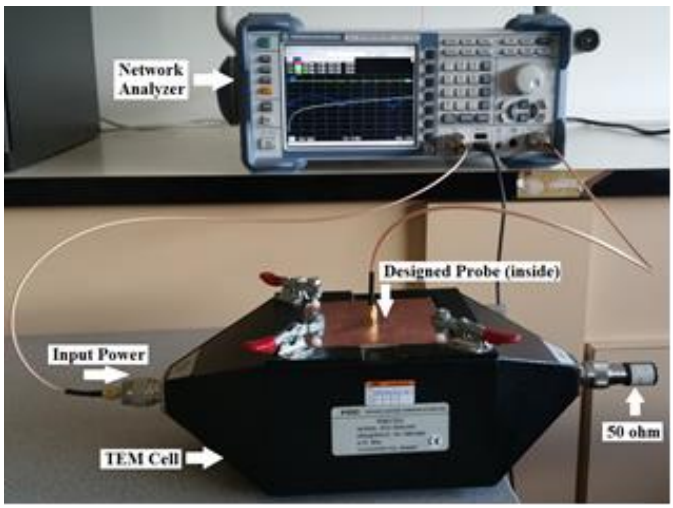

Figure 3-43 Calibration setup with TEM cell

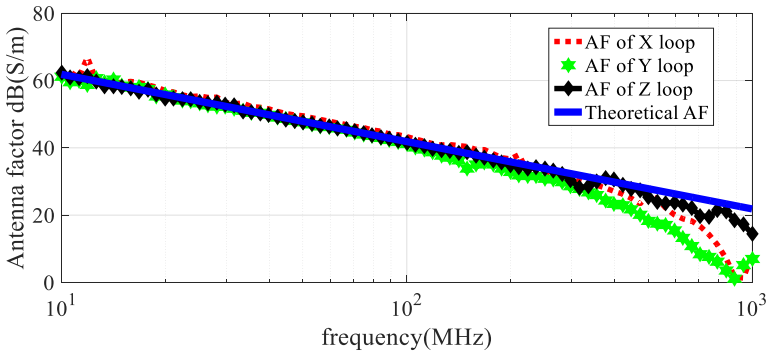

Figure 3-44 Measured antenna factor of the 3 axis probe

The measured AF of each loop in the proposed probe] is shown in Figure 3-44 for a frequency range of 10 MHz – 1 GHz along with the theoretical antenna factor. Compared to the theoretical AF, the antenna factor of each loop in the 3D probe has fluctuations above 200MHz. These are due to the coupling between the individual probes in the 3D probe.

3.9.1.3 Near field scanning

The near field scanning setup of this 3 axis probe is shown in Figure 3-45. During the near field scan, the z-axis is normal to the scanned plane. Measurements were done at different heights and frequencies. The scanning is done along the y-axis with a step width of 1 mm. The computed theoretical field values are compared with the measured ones at 13 MHz and 400 MHz and they are presented in Figure 3-46 and Figure 3-47 respectively. The normal and tangential component of the

magnetic field is plotted atd= 0.5mm and 2.5mm, where d is the distance from the top of the cylindrical conductor to the bottom side of the probe when placed as shown in Figure 3-45.

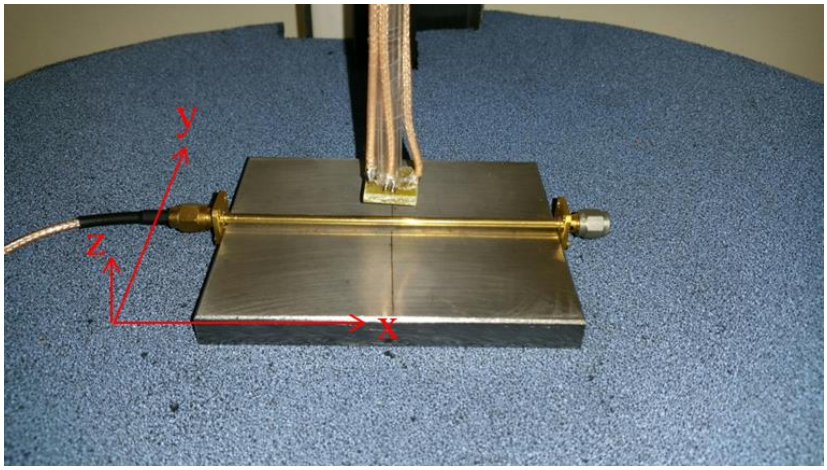

Figure 3-45 Configuration of near field scanning

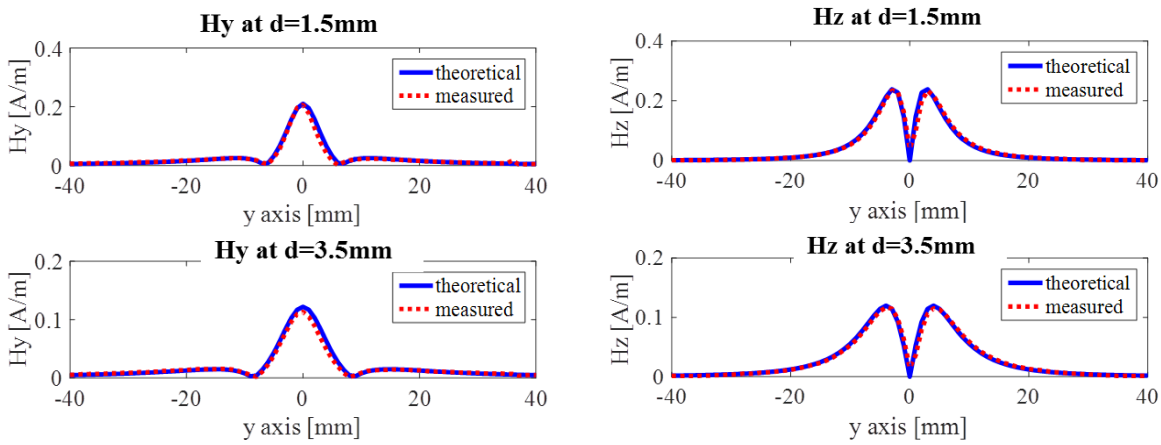

(a) (b)

Figure 3-46 H-field components at 13 MHz (a) normal component (b) tangential component

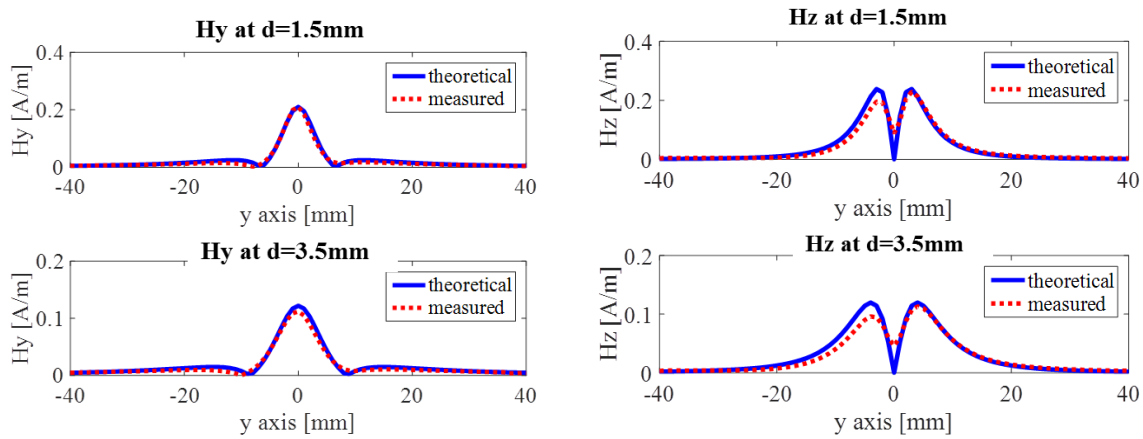

(a) (b)

Figure 3-47H-field components at 400 MHz (a) normal component (b) tangential component

Figure 3-46 shows the normal and tangential magnetic field component at 13MHz, while in Figure 3-47 the field components at 400 MHz are plotted along with the theoretical field. The comparison shows that the field measurements are in good agreement with the theoretical calculations for the 3D probe. Also, a good spatial resolution is obtained for the probes in measuring the magnetic field components. The volume of the proposed probe is only 15 % of the previous 3D probe[16]. Compared to the conventional circular loop probes printed circuit probes are easy to miniaturize and less susceptible to damage. Also, the proposed probes have the advantage of being low cost, compact and easy to handle.

The electrical connection between the loop and the coaxial cables is found to be very critical in the near fields scanning. The long connecting lines printed in the probe are found to distort the scanned profile of the probe. So the connecting pad to connect the loop to the coaxial cable is made very small in order reduce the coupling effects.

3.10 Active magnetic probes

There is always a trade-off between the sensitivity and the spatial resolution of the probe. The sensitivity of the probe is reduced when the probe is reduced, especially at low frequencies. Figure 3-48 shows the relation between the size of the probe, spatial resolution, and sensitivity of the probe at different frequencies. The spatial resolution of the probe is directly related to the size of the probe in such a way that the spatial resolution is half of the size of the probe. At the low frequencies, there is a gradual reduction in the sensitivity of the probe with the reduction in the size of the probe.

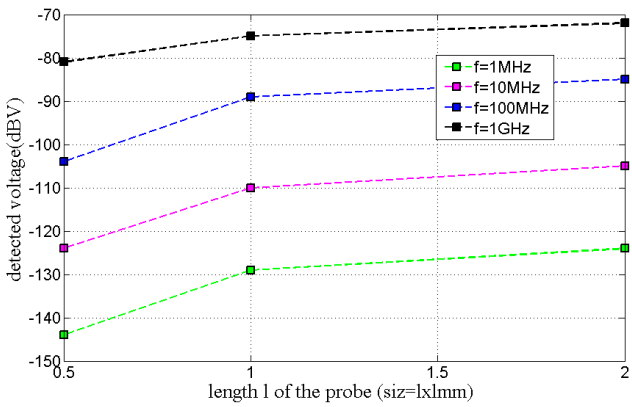

Figure 3-48 Graph showing the relation between the size of the probe and the sensitivity at various frequencies

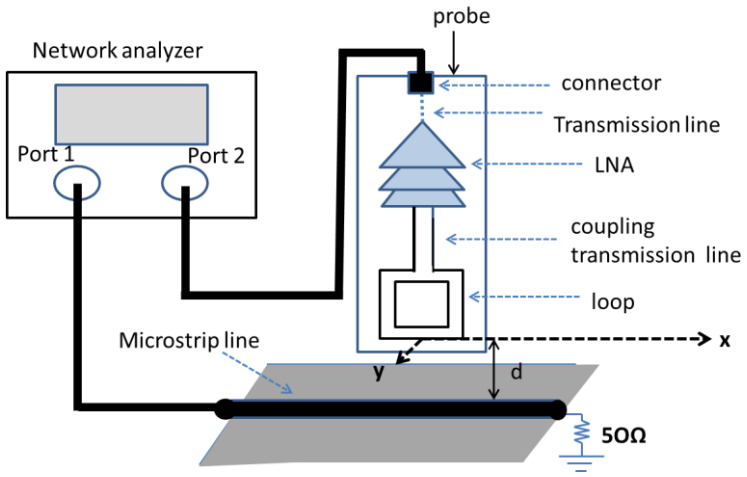

Figure 3-49 Schematic of active probe

We observed that the miniaturized probe suffers from a very low sensitivity at frequencies below 3 GHz. Integrating a low noise amplifier with a gain G (dB) at the output of the probe can solve the problem of low sensitivity. Some active probes existing in literature is based on CMOS integration technology [18][19]. With the integration of the amplifier, it is expected to increase the level of the detected output voltage of the probe by the gain of the amplifier, as it was the case with an external amplifier discussed in sec 3.8.1. The schematic diagram of an active probe in the measurement configuration is shown in Figure 3-49.

3.10.1 Design of active probe

The active probe is made by integrating an amplifier at the output of the loop in the probe. As a preliminary study, we have integrated a single stage Low noise amplifier (LNA) at the probe output of the shielded probe SP1 presented in sec 3.8.1. The chosen LNA is BGA 427, which has the gain as shown in Figure 3-50.The gain of the amplifier is measured using vector network analyzer. The noise figure of the LNA is 2.2 dB. The LNA is located at 8 cm away from the loop. The fabricated active probe (named as AP1-A) is shown in Figure 3-51. The active probe has the same length as that of the passive probe SP1. The dimensions of the loop aperture are 800µm x 800µm.

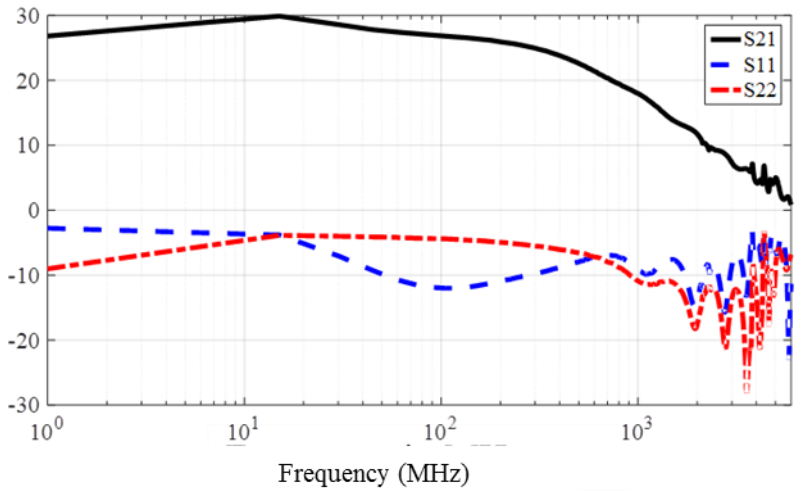

Figure 3-50 Measured gain and reflection coefficient of the amplifier

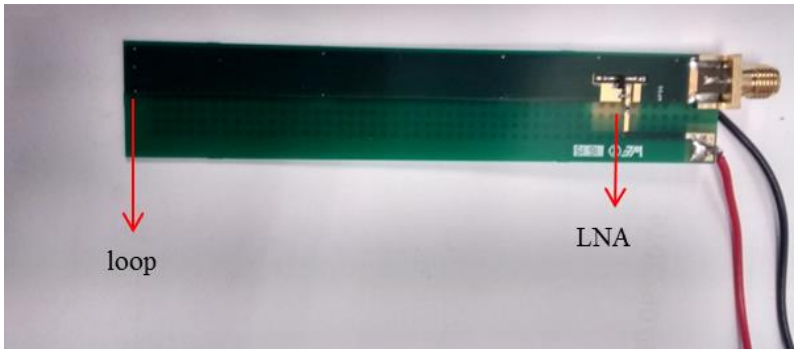

Figure 3-51 Fabricated active probe AP1-A

3.10.2 Characterization

The active probe AP1-A is characterized using a vector network analyzer from 1 MHz to 10 GHz. The near field map of the tangential magnetic field received by the active probe AP1-Ais plotted in Figure 3-52 at different frequencies. The detected profile up to 100 MHz is under the noise of the network analyzer. The 27 dB gain of the amplifier is not enough to detect the signals below 100MHz. The distorted profile at 10 MHz is completely below the noise floor of the receiver. From 100 MHz-500 MHz, even though the profile is detected, the points near minimum are close to the noise floor. But the profiles of the magnetic field from 800 MHz- 1 GHz are lost. This is due to the bad input and output reflection coefficient of the amplifier from 500 MHz to 1GHz.

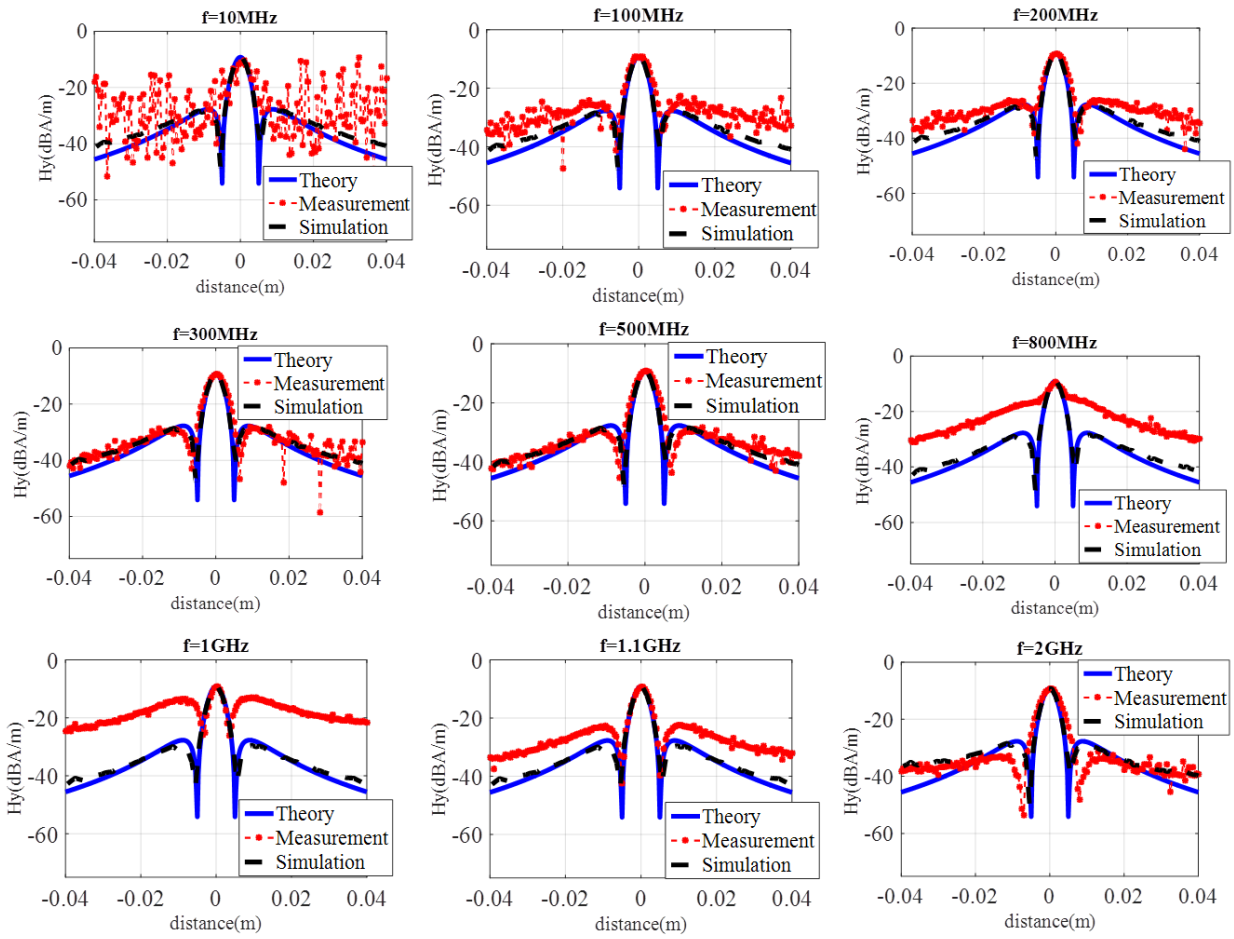

Figure 3-52 Measured tangential magnetic field of active probe AP1-A

3.10.3 Positioning of the amplifier on the active probe

It is necessary to know the optimum position where the amplifier can be placed on the probe. We have reduced the total length of the active probe to 2.9cm, and placed the amplifier close to the loop. The fabricated probe is shown in Figure 3-53and is named as AP1–B. The loop in the probe AP1-B has the same dimensions as that of AP1-A and SP1-A. In order to perform the near field scanning with this probe, an additional length of semi-rigid coaxial bale of 10 cm length is used as shown in Figure 3-53. The scanned profile of tangential magnetic field along the y-axis of the microstrip line is plotted in Figure 3-54.

At frequencies up to 10 MHz, the detected signal is completely below the noise floor as it was the case with AP1-A. But, unlike AP1-A, the profile at all frequencies are distorted. So, it can be concluded that there is an interaction between the magnetic field of the microstrip and the amplifier circuit. When the amplifier is away from the loop, it is away from the device under test also, so, there is less disturbance offered to the device under test by the amplifier. So, it is not wise to keep the amplifier circuit close to the loop, At the same time it is not possible to keep the amplifier very far, because it increases the length of the line between the loop and hence the total length of the

probe increases, which in turn reduces the highest operating frequency of the probe. The choice of the position of the amplifier has to be made subject to the frequency band in which the probe is required to operate.

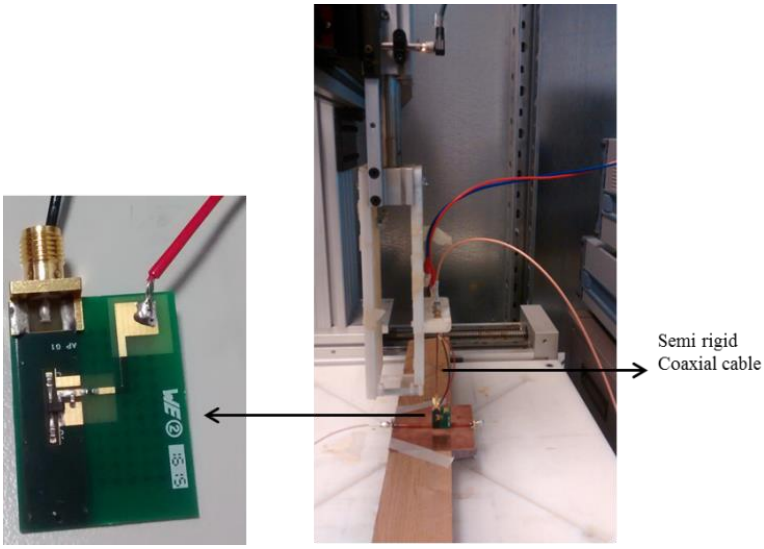

Figure 3-53 Active probe (AP1-B) and measurement configuration

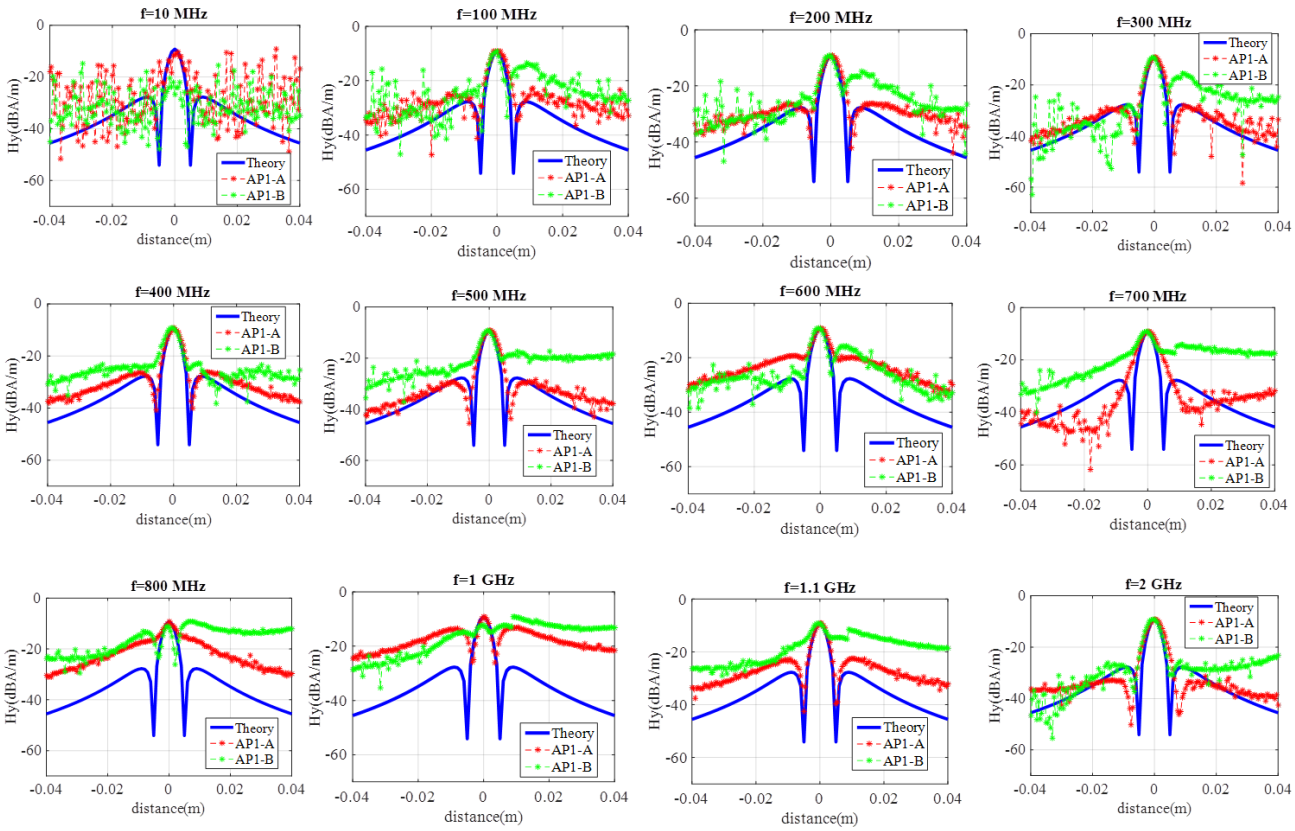

Figure 3-54 Measured tangential magnetic field; Comparison of the length of the active probe (AP1-A and AP1-B).

The reason for the deviation of the performance of the active probes from the passive probes can be explained from the measurement of the scattering parameter of all these probes above the device under test. The S-parameter S21 is a measure of the output voltage of the probe. When the probe is placed at the center of the cylindrical conductor, as in Figure 3-53, the detected output voltage has maximum value. The S21 as a function of frequency is plotted for both the active probes and the passive probe in Figure 3-55. The curve of the passive probe plotted here belongs to SP1-A, by using the external amplifier (ZPUL-30).

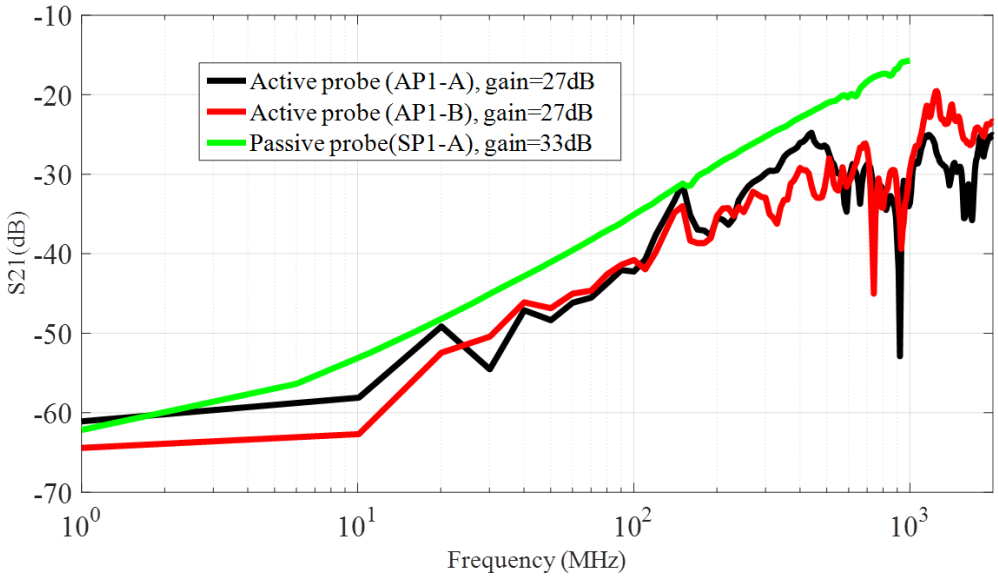

Figure 3-55 Comparison of the measured s parameter of the active and passive probes at the centre of the microstrip line

It is obvious that the loops of the same size don't give the same voltage at the output. The curves have a different level of detected voltage, and there are multiple resonances in the curve of active probe, which is not found in the output of passive probe measured with an external amplifier. The output voltage of AP1-A is more linear and close to that of passive probe up to 400 MHz, where the profile is detected correctly. Above 400MHz, the probe output is oscillating. This oscillating response is increased when the amplifier is placed close to the loop. These oscillations can be

- Due to the bad input and output reflection coefficient of the amplifier.
- Due to the interaction between the fields of the microstrip line and the probe.

For the probe AP1-B, there are more oscillations which are expected due to the reflection between the output of the amplifier and the semi-rigid coaxial cable, because the LNA has poor output reflection coefficient

3.11 Conclusion

In this chapter, we have designed and characterized probes based on microstrip line, CPW line,and shielded probes. The probes with single turn loop have the highest frequency band of operation. The output voltage at the probe is not only due to the voltage is a sum of the voltage due to the magnetic field and the voltage due to the electric field. The highest frequency of operation of the probes decreases with the increase in the length of the transmission line. E field coupling into the probe has very undesired effects. The common mode voltages are a big problem, which causes a large error in the measurement of the probes. The electric (E) field coupling into the probe is the major cause of common mode voltages at the probe output. The probes with microstrip and CPW configurations suffer from common mode response and the probe fails to detect the minimum magnetic field in the frequency band of 100 MHz- 1GHz.

The shielded probe suppresses the voltage due to the electric field. Rejection of the electric field in the shielded probe has also reduced the common mode response. It is observed that, for a single turn loop,it is not necessary to use the shielding for frequencies below 100 MHz, as they are not susceptible to electric field response.

The introductions of the shielded probe could resolve this problem up to some extent and increase the operating frequency range of the probe. Even with the shielded probe, the total length of the probe (loop + transmission line) plays an important role in the measured results.

As the size of the probe decreases, the sensitivity of the probe reduces, which requires the receiver with high sensitivity or the use of the amplifier in the measurement. The frequency operation of the probe then depends on the characteristics of the amplifier.

For a loop with 800µmx 800 µm dimensions, all the frequencies below 1GHz require the use of an amplifier. With an external amplifier connected to the probe, the sensitivity of the probe is increased and the profile of the magnetic field is detected correctly. But the active probe introduces more errors in the measurement, depending on the characteristics of the amplifier and the position of placement of amplifier. It may be not required to use an active probe to increase the sensitivity of the probe, as it introduces other problems and causes a spurious error in the measurement.

3.12 References

[1] D. Baudry, a. Louis, and B. Mazari, "Characterization of the Open-Ended Coaxial Probe Used for Near-Field Measurements in Emc Applications," *Prog. Electromagn. Res.*, vol. 60, pp. 311–333, 2006.

[2] F. Di Paolo, *Networks and devices using planar transmission lines*. CRC Press, 2000.

[3] C.-P. C. C.-P. Chen, K. S. K. Sugawara, K. Li, H. Nihei, T. Anada, and C. Christopoulos, "Non-contacting near-field mapping of planar circuits in microwave frequency band," *2008 IEEE Int. Symp. Electromagn. Compat.*, pp. 8–13, Aug. 2008.

[4] J. M. Kim, W. T. Kim, and J. G. Yook, "Resonance-suppressed magnetic field probe for em field-mapping system," *IEEE Trans. Microw. Theory Tech.*, vol. 53, no. 9, pp. 2693–2699, 2005.

[5] M. Spang, M. Albach, and G. Schubert, "Response of a magnetic loop probe to the current and voltage on a microstrip line," in *2008 IEEE International Symposium on Electromagnetic Compatibility*, 2008, pp. 2–6.

[6] C. Y. Ho, K. S. Chen, T. S. Horng, J. M. Wu, and C. H. Huang, "Method of measuring common-mode current conversion coefficient for estimating variation in radiated emission from printed circuit board components," *Radioengineering*, vol. 23, no. 2, pp. 709–716, 2014.

[7] C. F. M. Carobbi and L. M. Millanta, "Analysis of the Common-Mode Rejection in the Measurement and Generation of Magnetic Fields Using Loop Probes," *IEEE Trans. Instrum. Meas.*, vol. 53, no. 2, pp. 514–523, Apr. 2004.

[8] B. C. Wadell, *Transmission line design handbook*. Artech House, 1991.

[9] *Electromagnetic waves and radiating systems - Edward Conrad Jordan, Keith George Balmain - Google Books*. .

[10] C. F. M. Carobbi, L. M. Millanta, and L. Chiosi, "The high-frequency behavior of the shield in the magnetic-field probes," *IEEE Int. Symp. Electromagn. Compat. Symp. Rec. (Cat. No.00CH37016)*, vol. 1, pp. 35–40, 2000.

[11] Y. T. Chou and H. C. Lu, "Magnetic near-field probes with high-pass and notch filters for electric field suppression," *IEEE Trans. Microw. Theory Tech.*, vol. 61, no. 6, pp. 2460–2470, 2013.

[12] "Mini-Circuits." [Online]. Available: https://www.minicircuits.com/WebStore/dashboard.html?model=ZPUL-30P.

[13] H. Weng, D. G. Beetner, and R. E. Dubroff, "Prediction of radiated emissions using near-field measurements," *IEEE Trans. Electromagn. Compat.*, vol. 53, no. 4, pp. 891–899, Nov. 2011.

[14] S. Muroga, K. Arai, S. Dhungana, R. Okuta, Y. Endo, and M. Yamaguchi, "3-D magnetic-near-field scanner for IC chip-level noise coupling measurements," *IEEE Trans. Magn.*, vol.

49, no. 7, pp. 3886–3889, 2013.

[15] Y. Gao and I. Wolff, “A new miniature magnetic field probe for measuring three-dimensional fields in planar high-frequency circuits,” *IEEE Trans. Microw. Theory Tech.*, vol. 44, no. 6, pp. 911–918, 1996.

[16] K. Jomaa, F. Ndagijimana, J. Jomaah, and H. Ayad, “Near-field measurement system with 3D magnetic-field probe design for dosimetric applications,” in *2016 IEEE Middle East Conference on Antennas and Propagation (MECAP)*, 2016, pp. 1–4.

[17] J. P. Kärst, C. Groh, and H. Garbe, “Calculable field generation using TEM cells applied to the calibration of a novel E-field probe,” *IEEE Trans. Electromagn. Compat.*, vol. 44, no. 1, pp. 59–71, 2002.

[18] S. Aoyama, S. Kawahito, T. Yasui, and M. Yamaguchi, “A high-sensitivity active magnetic probe using CMOS integrated circuits technology,” in *IEEE 14th Topical Meeting on Electrical Performance of Electronic Packaging, 2005.*, pp. 103–106.

[19] S. Aoyama, S. Kawahito, and M. Yamaguchi, “An active magnetic probe array for the multiple-point concurrent measurement of electromagnetic emissions,” *IEEE Trans. Magn.*, vol. 42, no. 10, pp. 3303–3305, 2006.

4. Source reconstruction methods for the prediction of EMC

4.1 Introduction

It is required to predict the far field radiated from PCBs for the prediction of electromagnetic interference. The prediction of far field needs to have the knowledge of the radiating sources. The electromagnetic inverse problem can be defined as the reconstruction of the electromagnetic source from its radiated field. This source distribution can be used to calculate the far field which is more cost efficient than the direct far field measurement, which requires a large anechoic chamber.

This chapter deals with the methods for reconstruction of the sources from the near field scan data. Two methods based on the inverse transmission line matrix and 2D cross-correlation method is presented in the following sections.

4.2 EM source reconstruction using inverse- TLM method

4.2.1 Time reversal- an overview

A device that produces an outgoing wave, equal to the time symmetric of an incoming wave is defined as a time reversal mirror. It is an array of transceivers and dedicated electronics. The time dependence of an electric field is recorded on each transceiver in the first step. Each transceiver plays back the signal in reverse order during the second step. In the case of a tile symmetric propagation medium, the wave propagates back and finally focuses on the initial source location. The time reversal mirror is experimentally realized by D. Cassereau and M.Fink in their laboratory for the 3 D time reversal of ultrasonic fields[1][2]. A theoretical model for time reversal cavities to optimize homogeneous and inhomogeneous media is described. It used impulse diffraction theory to obtain the impulse response of the cavity in any inhomogeneous medium. After that TRM has been developed for acoustic applications such as sound focusing, ultrasonic non-destructive testing, ultrasonic hyperthermia for medical therapy and seismology [2][3]. The acoustic wave equation in a non-dissipative heterogeneous medium is invariant under a time reversal operation. Indeed, it only contains a second-order time-derivative operator. Therefore, for every burst of sound $\phi(\mathbf{r}, t)$

diverging from a source- and possibly reflected, refracted or scattered by any heterogeneous media- there exists in theory a set of waves $\phi(\mathbf{r},-t)$ that precisely retraces all of these complex paths and converges in synchrony, at the original source, as if time was going backwards. This is the basic idea behind the time reversal in acoustics. It requires both the time-reversal invariant and spatial reciprocity to reconstruct the time-reversed wave in a whole volume.

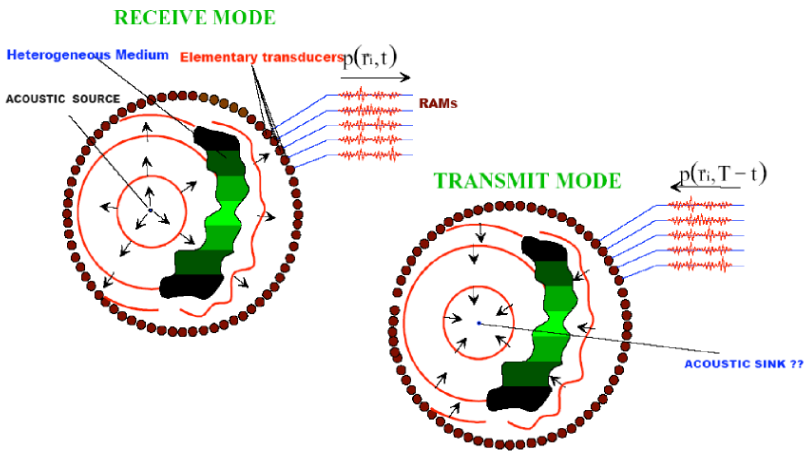

Figure 4-1 Time reversal in acoustics (a) Recording step: A closed surface is filled with transducer elements. A point-like source generates a wavefront which is distorted by heterogeneities. The distorted pressure field is recorded on the cavity elements. (b) Time-reversed or reconstruction step: The recorded signals are time-reversed and reemitted by the cavity elements. The time-reversed pressure field propagates back and refocuses exactly on the initial source.[4]

In acoustics, a closed time-reversal mirror (TRM) consists of a two-dimensional piezoelectric transducer array that samples the wavefield over a closed surface as shown inFigure 4-1[4]. An array pitch of the order of λ/2, where λ is the smallest wavelength of the pressure field needed to ensure the recording of all the information on the wavefield. Electronic circuitry connected to each transducer consists of a receiving amplifier, an A/D converter, a storage memory and a programmable transmitter able to synthesize a time-reversed version of the stored signal. The time reversal technique is applied more recently in electromagnetics[5][6].

The first experimental demonstration on time reversal focusing of electromagnetic waves is done by G. Lerosey et.al[7]. Theory of monochromatic time reversal for electromagnetic waves was developed by[8]. Figure 4-2 shows the simplified sketch of time reversal with dipolar sources. The applications of time reversal mirrors include radio communications, terahertz imaging and medical imaging [9][10][11]. The decomposition of time reversal mirrors (DORT) method is used to detect the scatterers in the electromagnetic field[12].

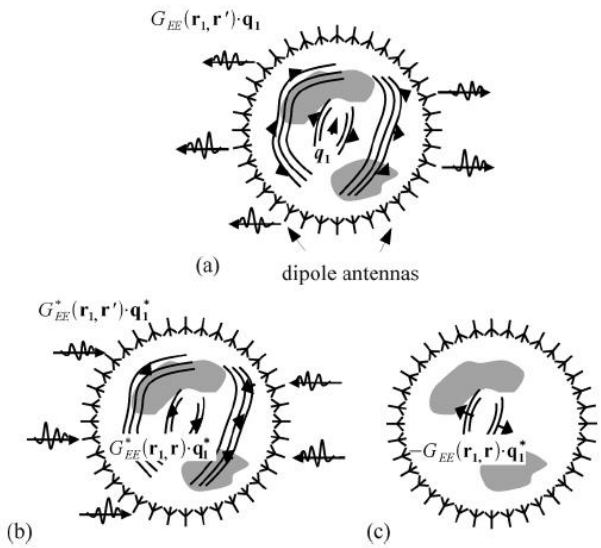

Figure 4-2 Schematic illustration of the far field time reversal by dipolar sources: (a) A source generates a wave. The electric components are recorded on a closed surface. (b) This electric field is time reversed and re-emitted by dipolar sources and the back propagated wave is generated. (c) The converging wave is followed by a diverging one[7].

A numerical synthesis technique based on inverse transmission line matrix was first proposed by [13]to reconstruct the scattering sources. Later it is used in the synthesis of microwave filters and antennas and deals with the problem of resolution[14][15][16][17][18][19].

4.2.2 Transmission line matrix (TLM) method

The transmission line method is an approach to the simulation of wave motion and other physical phenomenon. It is a physical model with an exact computer solution. It is a modelling process rather than a numerical method for solving differential or integral equations. TLM method sets up a spatial and time discretization scheme. It substitutes the original medium by an analogous transmission line mesh in which voltage and current pulses propagate in the same way as the electromagnetic waves would propagate in the original medium.

The expanded node network has been used for a variety of applications until the 1990s. It is a network of transmission lines developed by interconnecting two-dimensional series and shunt nodes. As these nodes have a time delay of half a time step, these nodes are called as expanded node network. The topology of the expanded node network and finite difference method is quite complicated. The nodes to calculate different field component are spatially separated. Due to this, the data preparation for the modelling of boundaries is difficult and liable to error, and the problem is acute in the implementation of automatic data preparation schemes. The inconvenience of an expanded node structure has led to the development of a condensed node structure by P. Saguet and E. Pic in 1982 [20]. Depending on the direction of view, the first connection in the node is either

shunt or series. Hence, the node is said to be an asymmetrical condensed node. Even though the effect of these asymmetries is insignificant, the boundaries viewed in one direction have slightly different properties when viewed in another direction. Although it involves quite lengthy arithmetic, the asymmetrical condensed node technique uses less resource than expanded node technique. The symmetrical condensed node (SCN) developed by P.B. Johns eliminates the disadvantages of asymmetric and lengthy arithmetic while preserving the advantages of condensed node working. He has developed the scattering matrix for the SCN with and without the stubs. The absence of stubs means that the node represents only a cubic block of Cartesian mesh. The extra inductance and capacitance cannot be added locally to the node. The node with stubs can be used in inhomogeneous problems[21][22].

The symmetrical condensed node without stubs is shown in Figure 4-3. The two polarizations in any direction of propagation are carried out on two pairs of non-coupling transmission lines. There are 12 transmission lines and each of them has characteristic impedance Z_0 same as that of free space. Since these lines link the Cartesian mesh of nodes together, they are called as link transmission lines. The incident and reflected pulses appear on the terminals of the transmission line. The 12 incident pulses on the link transmission lines produces scattering into 12 reflected pulses. The scattering is defined by

$$V^r = SV^i \qquad 4\text{-}1$$

Where S is a 12x12 matrix with elements S_{mn} in the m th row and n th column.

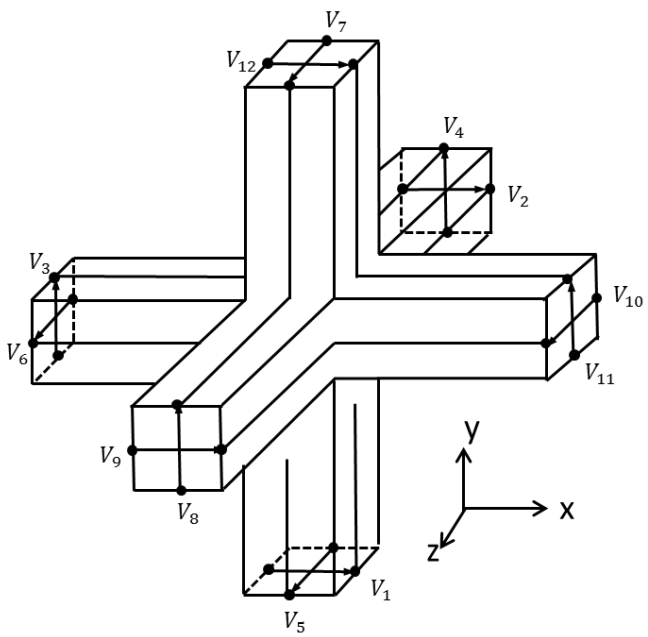

Figure 4-3 TLM symmetrical condensed node (SCN)

For a condensed node without stub, the scattering matrix is given as follows

$$S = \begin{bmatrix} 0 & 1 & 1 & 0 & 0 & 0 & 0 & 0 & 1 & 0 & -1 & 0 \\ 1 & 0 & 0 & 0 & 0 & 1 & 0 & 0 & 0 & -1 & 0 & 1 \\ 1 & 0 & 0 & 1 & 0 & 0 & 0 & 1 & 0 & 0 & 0 & -1 \\ 0 & 0 & 1 & 0 & 1 & 0 & -1 & 0 & 0 & 0 & 1 & 0 \\ 0 & 0 & 0 & 1 & 0 & 1 & 0 & -1 & 0 & 1 & 0 & 0 \\ 0 & 0 & 0 & 0 & 1 & 0 & 1 & 0 & -1 & 0 & 0 & 0 \\ 0 & 0 & 0 & -1 & 0 & 1 & 0 & 1 & 0 & 1 & 0 & 0 \\ 0 & 0 & 1 & 0 & -1 & 0 & 0 & 0 & 0 & 0 & 1 & 0 \\ 1 & 0 & 0 & 0 & 0 & 1 & 0 & 0 & 0 & 1 & 0 & 1 \\ 0 & -1 & 0 & 0 & 1 & 0 & 1 & 0 & 1 & 0 & 0 & 0 \\ -1 & 0 & 0 & 1 & 0 & 0 & 0 & 1 & 0 & 0 & 0 & 1 \\ 0 & 1 & -1 & 0 & 0 & 0 & 0 & 0 & 1 & 0 & 1 & 0 \end{bmatrix} \qquad 4\text{-}2$$

In order to excite the separate components of E and H, a possible set of incident pulses are given by the following equations.

$$V_1^i = {(uE_x + wZ_0H_z)}/{2} \qquad 4\text{-}3$$

$$V_2^i = {(uE_x - vZ_0H_y)}/{2} \qquad 4\text{-}4$$

$$V_3^i = {(vE_y - wZ_0H_z)}/{2} \qquad 4\text{-}5$$

$$V_4^i = {(vE_y + wZ_0H_x)}/{2} \qquad 4\text{-}6$$

$$V_5^i = {(wE_z + uZ_0H_x)}/{2} \qquad 4\text{-}7$$

$$V_6^i = {(wE_z + vZ_0H_y)}/{2} \qquad 4\text{-}8$$

$$V_7^i = {(wE_z + uZ_0H_x)}/{2} \qquad 4\text{-}9$$

$$V_8^i = {(vE_y - uZ_0H_x)}/{2} \qquad 4\text{-}10$$

$$V_9^i = {(uE_x + vZ_0H_y)}/{2} \qquad 4\text{-}11$$

$$V_{10}^i = {(wE_z - vZ_0H_y)}/{2} \qquad 4\text{-}12$$

$$V_{11}^{i} = \left(vE_y + wZ_0H_z\right)/2 \qquad 4\text{-}13$$

$$V_{12}^{i} = \left(uE_x + wZ_0H_z\right)/2 \qquad 4\text{-}14$$

The output E and H fields are calculated as follows,

$$E_x = \left(V_1^i + V_2^i + V_9^i + V_{12}^i\right)/2u \qquad 4\text{-}15$$

$$E_y = \left(V_3^i + V_4^i + V_8^i + V_{11}^i\right)/2v \qquad 4\text{-}16$$

$$E_z = \left(V_5^i + V_6^i + V_7^i + V_{10}^i\right)/2w \qquad 4\text{-}17$$

$$H_x = \left(V_4^i + V_5^i + V_7^i + V_8^i\right)/2Z_0u \qquad 4\text{-}18$$

$$H_y = \left(-V_2^i + V_6^i + V_9^i + V_{10}^i\right)/2Z_0v$$

$$H_z = \left(-V_3^i + V_1^i + V_{11}^i + V_{12}^i\right)/2Z_0w \qquad 4\text{-}21$$

The pulses at port 1, 2, 9 and 12 contribute to Ex field. The pulses at port 3, 4, 8, and 11 contribute to Ey field. And the pulses contributing to Ez field are at ports 5, 6, 7 and 10. Similarly, the Hx field is contributed by pulses at ports 4, 5, 7 and 8. Hy is contributed by pulses at ports 2, 6,9,10 and Hz is due to the pulses at ports 1, 3, 11, 12.

4.2.3 Inverse TLM method

The 1-D scalar wave equations aregiven by

$$\nabla^2 - \frac{1}{c^2}\frac{\partial^2}{\partial t^2}\Psi(\overline{r,r_0},t) = 0 \qquad 4\text{-}22$$

Theory of wave propagation TR is based on the invariance property of the scalar wave equation 4-22 under TR transformation, in a lossless space. Where, $\Psi(\overline{r,r_0},t)$ is the scalar radiated field, r is the distance-vector between the source and the observation point, r_0 is the source position, t is the time and c is the speed of light. This is a differential equation, containing only a second order derivative with respect to time. Therefore, if $\Psi(\overline{r,r_0},t)$ is a solution of this equation, then $\Psi(\overline{r,r_0},-t)$ is also a solution [23], [24]. It can be said in other words that, scalar wave equation remains invariant under TR transformation in a non-absorbing medium.

Maxwell's equations are also symmetrical under time reversal. So, if E(r,t)and H(r,t) are solutions of Maxwell's equations, then E (r,-t) and −H (r,- t) are solutions of the same set of equations. On

the other hand, in all wave propagation problems, boundary and initial conditions determine a unique solution of the wave equation:

$$\Psi(\overline{r},\overline{r_0},t) = G(\overline{r},\overline{r_0},t) * f(t) \qquad 4\text{-}23$$

Where $G(\overline{r},\overline{r_0},t)$ is the greens function, $f(t)$ initial time domain excitation, * is the convolution operator in time domain. So, changes in the initial condition generates the dual solution $\Psi(\overline{r},\overline{r_0},-t)$.

The impulse scattering matrix of the two-dimensional TLM shunt node which relates the reflected voltage impulses at the time (k + 1)At to the incident voltage impulses at the previous time step kAt is identical to its inverse. So we can write

$$\begin{bmatrix} V_1 \\ V_2 \\ V_3 \\ V_4 \end{bmatrix}_{k+1}^{r} = \frac{1}{2}\begin{bmatrix} -1 & 1 & 1 & 1 \\ 1 & -1 & 1 & 1 \\ 1 & 1 & -1 & 1 \\ 1 & 1 & 1 & -1 \end{bmatrix}\begin{bmatrix} V_1 \\ V_2 \\ V_3 \\ V_4 \end{bmatrix}_{k}^{i} \qquad 4\text{-}24$$

The scattering matrix is equal to its inverse

$$S^{-1} = S \qquad 4\text{-}25$$

Where

$$S = \frac{1}{2}\begin{bmatrix} -1 & 1 & 1 & 1 \\ 1 & -1 & 1 & 1 \\ 1 & 1 & -1 & 1 \\ 1 & 1 & 1 & -1 \end{bmatrix} \qquad 4\text{-}26$$

This property of the scattering matrix implies that the TLM process can be reversed without any change in the scattering algorithm. Practically speaking, if a TLM network has been excited by a single voltage impulse at time t = 0, and if after k computational steps the impulses on all branches of the mesh have been computed and stored, one can return to the initial state at t = 0 by reversing the direction of all impulses at t = k and iterating k-times. By virtue of the unique property of the scattering matrix, this reverse simulation is identical to a forward simulation in which the initial excitation has been obtained by re-injecting the result of a previous simulation. So, one can reconstruct a source distribution from a field distribution by reversing the TLM process in time. This is true for three dimensional distributed and condensed node algorithms. Thus, an EM radiation process can be theoretically time- reversed without any change. The unique difference is that the initial conditions change.

4.2.4 EM source synthesis with reverse TLM method- state of the art

The EM point source reconstruction using the radiated fields outside the region containing the sources has been studied in [25][26]Different phases of forwarding and backward simulation of an impulsive point sources using inverse TLM is shown in Figure 4-4.

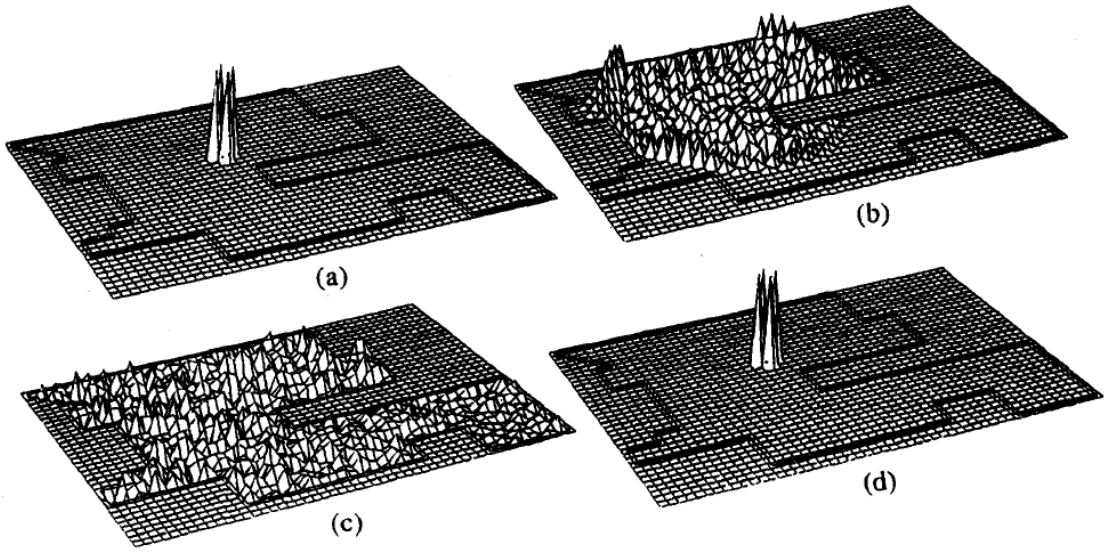

Figure 4-4 Four phases of a forward/backward simulation involving (a) the excitation of a lossless structure by a single impulse after the first iteration, (b) the field in the structure after 20 iterations, (c) the field in the structure after 100 iterations, and (d) the reconstructed source after 100 inverse computation steps[13].

The reconstruction of the source is affected only by the round-off error which is typically less than 10^{-5} for several thousand computation steps in single precision[13]. They have reconstructed the induced sources from the scattered field using inverse TLM method. Figure 4-5 shows two identical sections of parallel plate waveguide which are terminated with absorbing boundaries at its ends. The upper one is empty and the lower one contains a thin perfectly conducting septum. Figure 4-6 shows different steps in the reconstruction process from the scattered field. A Gaussian pulse is used as the excitation signal. This procedure differs from the previous one in that the forward response is not simply reversed at all nodes in the network, but it has first picked up the response at a limited number of output points, and then re-injected after subtracting the incident filed. The resolution of reconstruction was directly proportional to the mesh parameter Δl.

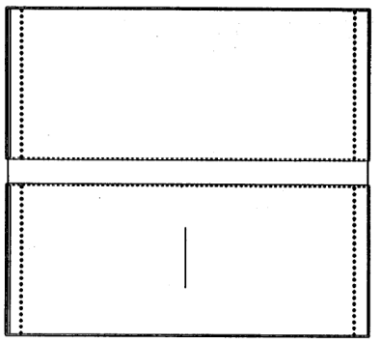

Figure 4-5Top views of two parallel plate waveguide sections matched at both ends. The upper section is empty and the lower section contains a conducting septum [13]

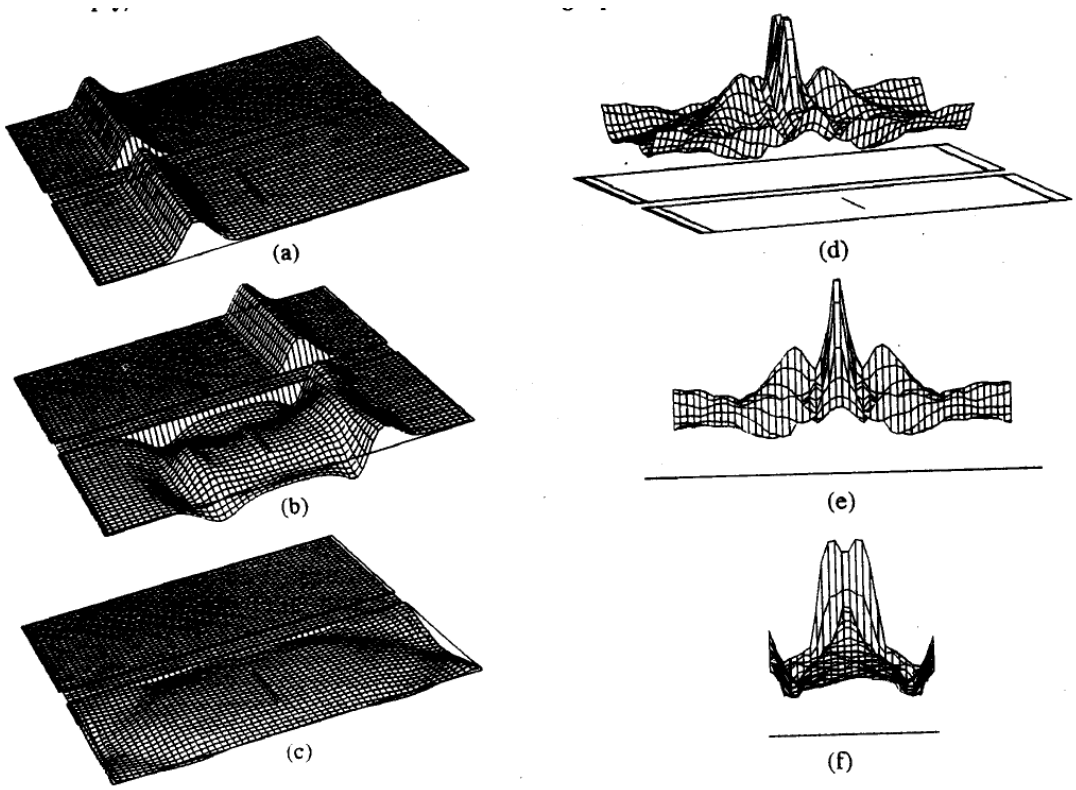

Figure 4-6Response for a Gaussian pulse injected into both sections from the left side of the waveguide: (a) to (c) show the fields after 30,70 and 100 iterations. The responses of both structures are captured at the output points, subtracted from each other, and re-injected at the same points into the empty section in reverse time sequence. (d)-(e) the perspective, side and front views of the maximum field after re-injection[13]

Another synthesis procedure for conducting scatterers is proposed by [27]. They have also demonstrated the source reconstruction in a simple discontinuity inside a parallel plate waveguide as shown in Figure 4-7, which consists of a thin conducting obstacle at the center. Their synthesis method consists of the following stages (1) a time sampled Gaussian pulse is injected into the empty waveguide and the incident pulses on both the absorbing boundaries are stored using forward analysis; (2) the same pulses are stored with the discontinuity in place using forward analysis; (3) as a final step, both the impulse responses are subtracted from each other yielding a particular solution

and this output function is then time reversed and applied to both ends of the waveguide. The number of computational steps in all stages was kept the same. The different aspects of the contour of the obstacle were determined from different field components. The highest value of the normal electric field occurs at the surface of the obstacle. The position of the sharp edges of the scatterer was determined from the longitudinal magnetic field components. Figure 4-8 (a) shows the image from which the conducting septum is reconstructed.

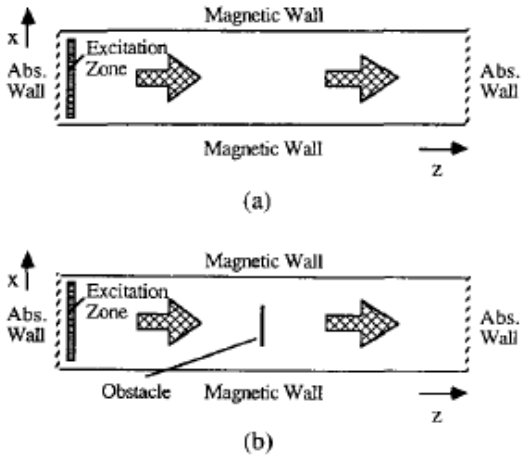

Figure 4-7Parallel plate waveguide: (a) Empty waveguide yielding the homogeneous field solution. (b) Waveguide with an obstacle[27]

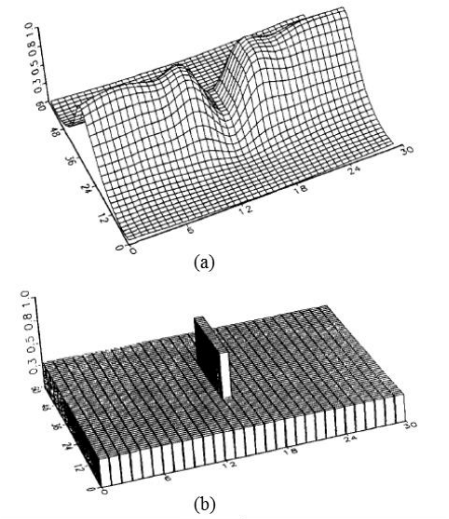

Figure 4-8Results for the synthesis of a metallic septum: (a) Distribution of the maximum value of the magnitude of the Poynting vector inside the structure after the inversion of the TLM process. (b) The shape of the reconstructed obstacle extracted from the Poynting vector distribution[27].

A.Ungureanu has used the Time reversed TLM method to reconstruct the unknown source reconstruction from the far field radiation [18]. An additional resolution improvement step is performed in order to overcome the spatial resolution limit of half wavelength. Figure 4-9 shows the result of the reconstruction of two point sources. The first figure (a) is obtained after the first

reconstruction process and the second figure (b) is obtained after the resolution improvement step. With the resolution improvement procedure, they have overcome the spatial resolution limit of half wavelength. They have also applied inverse TLM method to reconstruct the monopole antenna from its far field radiation pattern. The reconstructed normal magnetic field component of monopole is shown in Figure 4-10. The position and orientation of the current distribution are determined from the reconstructed field.

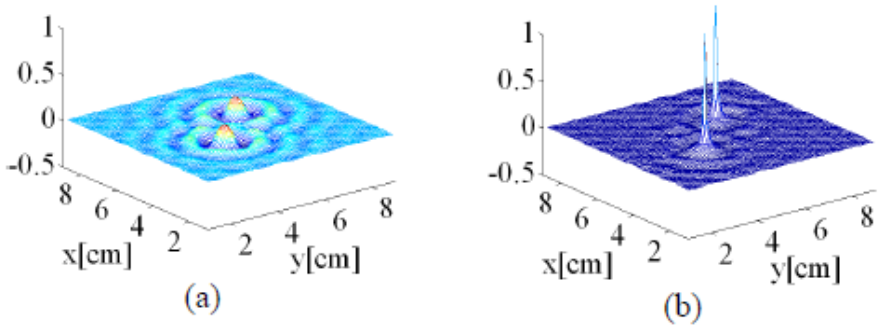

Figure 4-9 Reconstructed sources (a) after coarse reconstruction step (b) after resolution improvement step[18]

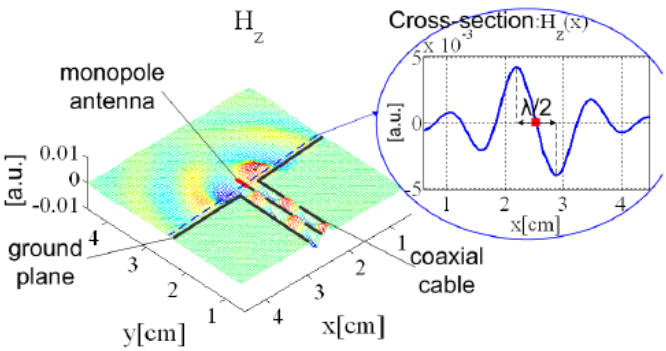

Figure 4-10 Normal component of magnetic field in the plane containing the monopole antenna[18]

4.3 Equivalent source from near field data using Inverse TLM Method

4.3.1 Excitation signal

The main advantage of a time domain method resides in the ability to work with a large bandwidth signal and the possibility to include transient phenomena which are both important in the time domain synthesis of a microwave structure. In order to represent the real RF excitation signals a Gaussian modulated sinusoidal pulse, centered at the required frequency is used as the excitation signal. In the following sections, a pulse shown in Figure 4-11is used to excite the current and voltage sources. The center frequency this pulse is at 100 MHz, which is shown in the frequency of

the same signal. The frequency spectrum is obtained by calculating the discrete Fourier transform (DFT) of the signal.

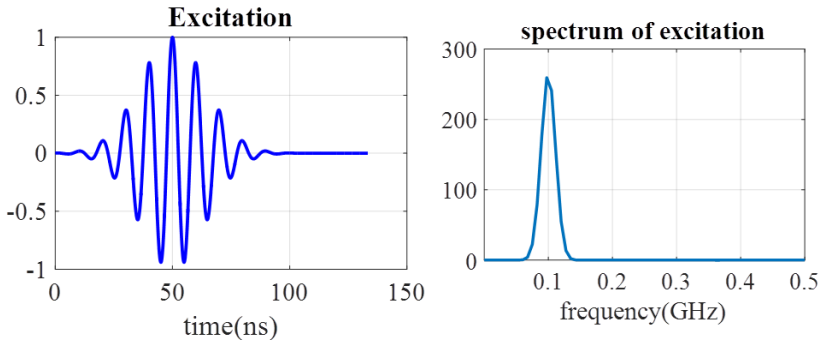

Figure 4-11 Excitation signal used in the TLM mesh

4.3.2 Reconstruction of ideal sources

In order to validate the source reconstruction using inverse TLM algorithm, the developed method is applied to ideal sources with different polarization. The sources are considered to be above a ground plane as the real PCB will have a large ground plane.

4.3.2.1 Ey polarization

Excitation by an electric field corresponds to a voltage source. A distributed voltage source Vy is excited at the center of the XZ plane. The metallic ground is provided at 1.5mm below the source (Figure 4-12).

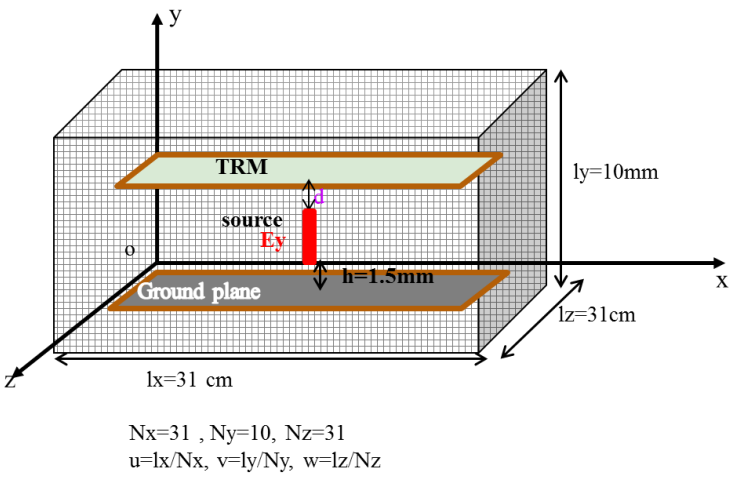

Figure 4-12 TLM cell with an ideal voltage source Ey

The length of the source l_s= 2mm. The electric and magnetic fields are recorded at 1 mm above the source by applying direct TLM. These fields are time reversed in the plane, which is called as time reversal mirror (TRM) and inverse propagated. The fields at the plane of the source are recorded after the inverse performing inverse propagation with inverse TLM method. The real component of

reconstructed E and H fields at the source position are shown in Figure 4-13 below. These fields are recorded at the time when the normal component of electric field Ey has a maximum value

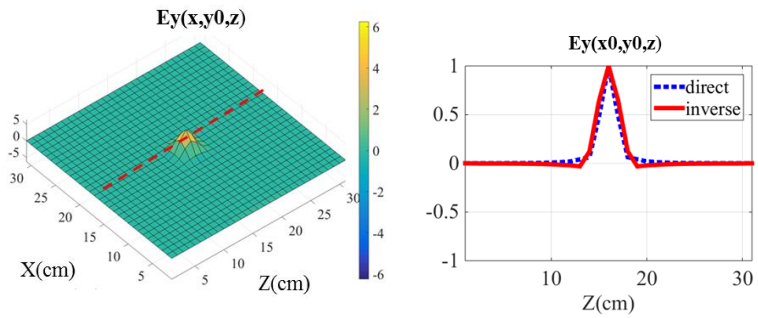

(b)

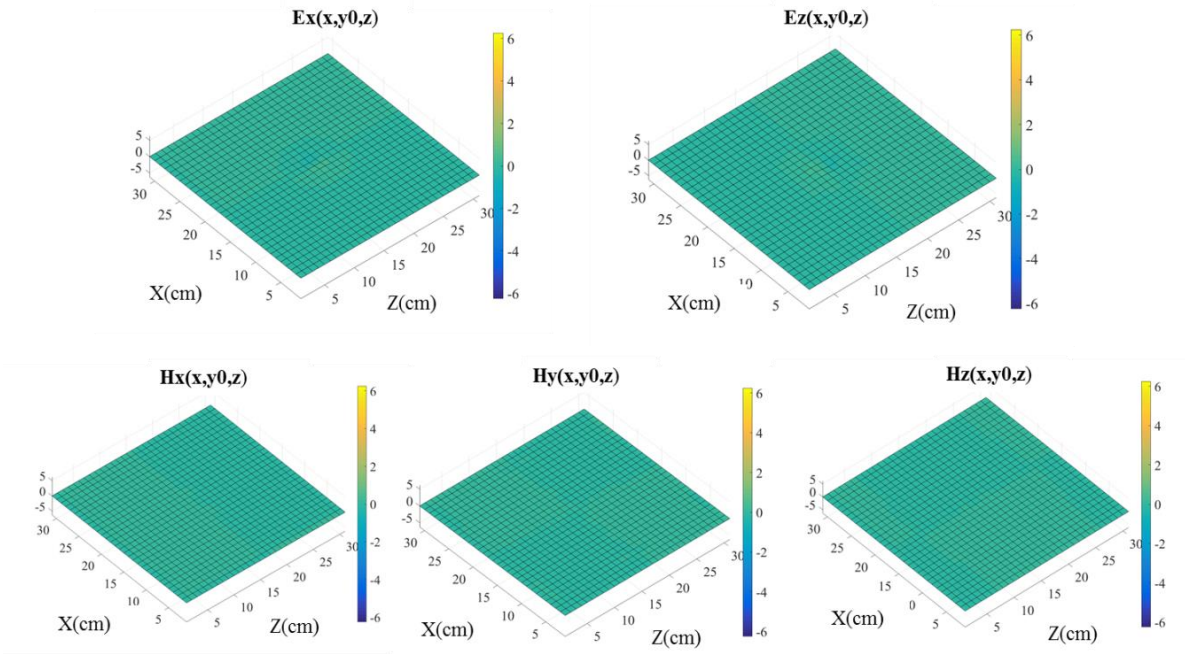

(c)

Figure 4-13 Real component of reconstructed E and H fields at the plane of the source Vy (a) Ey (b) Normalized Ey along the dotted lines in the z-axis (c) Ex, Ez, Hx, Hy, Hz

The y component of electric field in the XZ plane is shown in Figure 4-13 (a), and its cross-section along the dotted red line is plotted in Figure 4-13 (b). The other field components at this time are shown in Figure 4-13 (c). Among all the field components, Ey has the maximum value. This indicates that the source is a voltage source with y polarization. The normalized electric field Ey of the source calculated by the direct method at the same position is compared with the reconstructedEy, in the cross-sectional plot of Ey along the Z-axis in Figure 4-13 (b).

4.3.2.2 Ex polarization

A voltage source with x polarization Vx is placed above the ground plane (as shown in Figure 4-14). The length of the source is 2mm. The ground plane is situated 1.5mm below the source. The

electric and magnetic fields in the XZ plane at 1mm above the source are recorded using the direct TLM process and time reversed for inverse propagation.

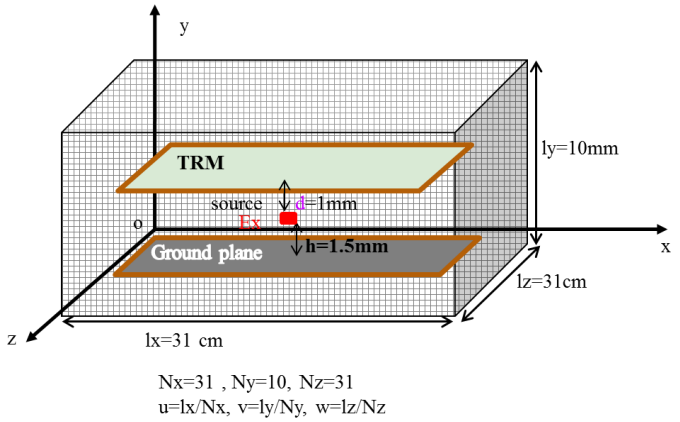

Figure 4-14 TLM cell with ideal voltage source Ex

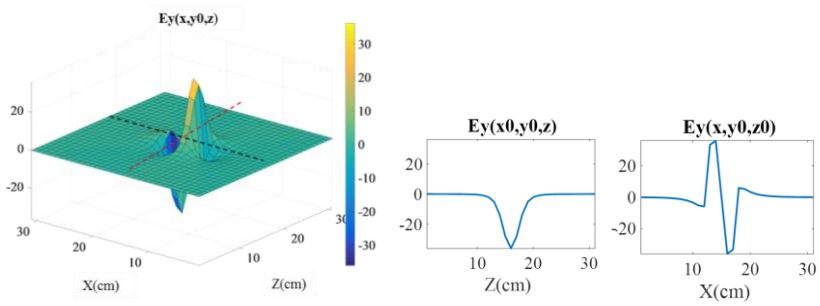

(a) (b)

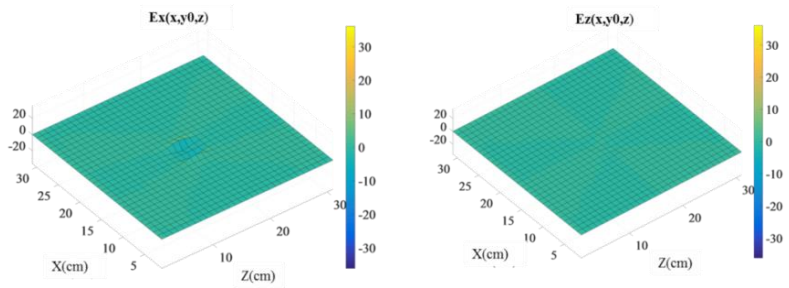

(c)

Figure 4-15 Real component of reconstructed E fields at the plane containing the source Vx (a) reconstructed Ey, (b) cross-sectional view of Ey along z-axis and x-axis (c) Ex and Ez

The real component of reconstructed fields at the plane of the source is shown in Figure 4-15. The fields are plotted at the time when the tangential electric field Ex is maximum. But, it is to be noted that, at this time, the normal component of the electric field has the maximum value among all the field components. The maximum amplitude of Ex is only 12% of the maximum amplitude of Ey. This is because we took the fields for reconstruction from the plane which is tangential to the source

and also the source is reconstructed in the tangential plane. The normal component of E field at the plane of the source is plotted in Figure 4-15 (a). And its cross sections along the x and z-axis are shown in Figure 4-15 (b). The tangential field components in this plane are plotted in Figure 4-15 (c). Their amplitude is negligible compared to the amplitude of the normal component. From the distribution of the normal component of E field, we can see that the E field varies along the x-axis. It has a positive and negative maximum along the x-axis with the same magnitude. Along z-axis, the field has only one peak, and there are no alternating maxima and minima.

4.3.2.3 Ez polarization

Similarly, a voltage source is excited with z polarization as in Figure 4-16. The length of the source is 2mm, which is same as before. Figure 4-17 shows the reconstructed electric fields at the plane of the source.

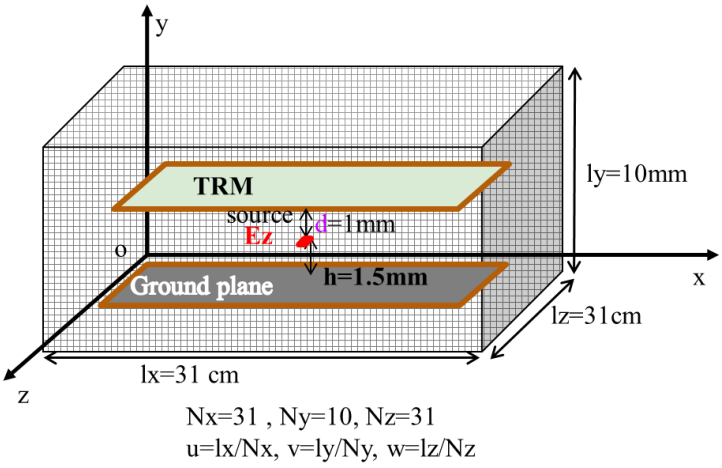

Figure 4-16 TLM cell with ideal voltage source Ez

The reconstructed fields are quite similar to that of the voltage source with x polarization, except that the axis has changed. The maximum amplitude of Ez is only 12.5% as that of the maximum amplitude of the normal E field component. In this case, the y component of the E field has an alternating maximum and minima along the z-axis as shown the cross-sectional plot in Figure 4-17 (b). The other E field components Ex and Ez plotted in Figure 1 21 (c) are close to zero because the plane of reconstruction is tangential to the orientation of the source.

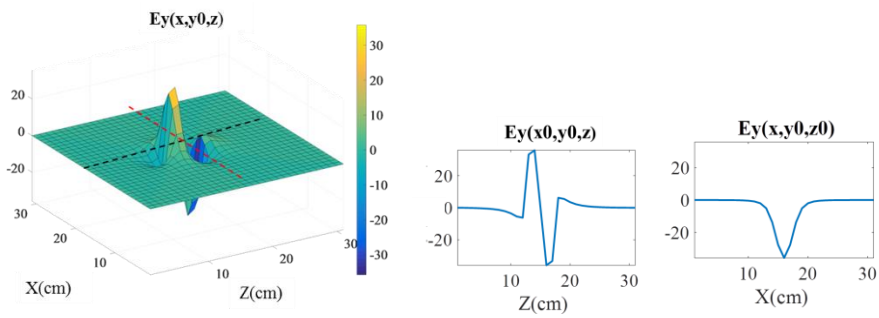

(a) (b)

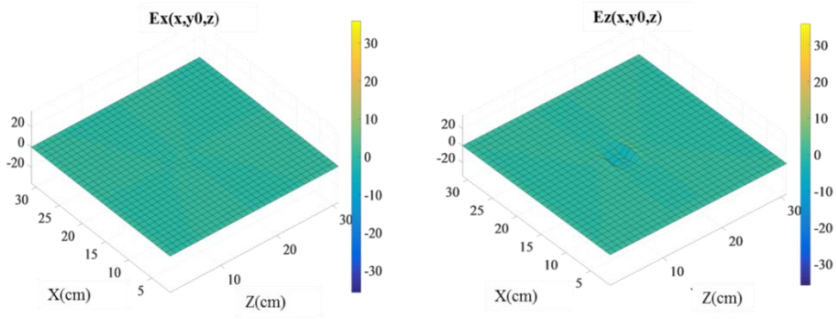

(c)

Figure 4-17 Real value of reconstructed E fields at the plane containing the source Vz (a) reconstructed Ey, (b) cross-sectional view of Ey along z-axis and x-axis (c) Ex and Ez

Now, we can conclude that for a tangential voltage source, the distribution of the normal component can be used to determine the orientation of the source. If the source is oriented along the x-direction, the normal component of E field will have alternating maximum and minimum along the axis and if the source is oriented along the z-axis, the alternating maxima and minima of the normal electric field component are found along the z-axis.

4.3.2.4 Current source Jy

A circulating magnetic field produces a current at the center and vice versa. A current source Jy is excited at the center of the TLM mesh as shown in Figure 4-18. The length of the current source is 3mm and is oriented along the y-direction. The current source is simulated using the direct TLM method. The E and H fields at 1mm above the current source are recorded in the XZ plane. These fields are time reversed and inverse propagated towards the direction of the source. The number of time steps in both the forward and reverse computation is kept the same. As it is a vertical current source, the tangential component of the magnetic field will give the information about the current source. The reconstructed tangential magnetic fields Hx and Hz are plotted at 2.5mm above the ground plane (shown in Figure 4-19). We can see that the Hx component alternates along the x-direction and the Hz component alternates along the z-direction, forming a circulating magnetic field. From this, we can determine the current source is a vertical current Jy and is at the center of the alternating magnetic field Hx and Hz.

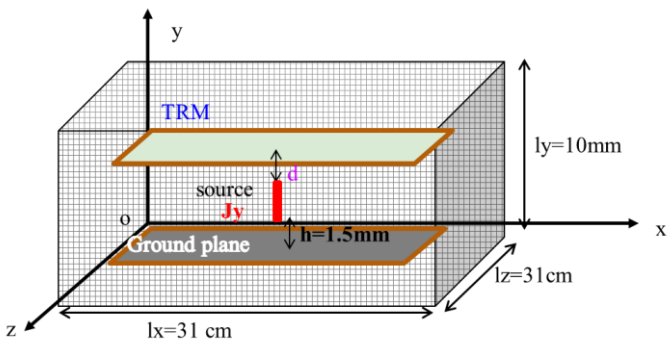

Figure 4-18The vertical current source in the TLM mesh, d=1mm

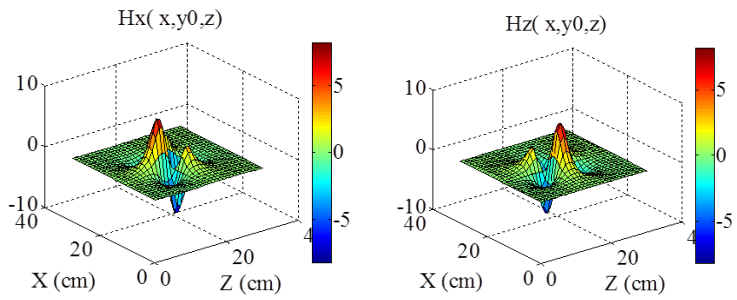

(a) (b)

Figure 4-19Real component of reconstructed magnetic fields at the position of the current source Jy (2.5mm above the ground plane) (a) Hx (b) Hz

4.3.2.5 Current source Jz

A current source oriented along the z-axis, Jz is excited at the TLM mesh as shown in Figure 4-20. The time reversal mirror is located at 1 mm above the current source. The electric and magnetic fields recorded at 1mm are applied in the TRM.We know that the plane at which the source is reconstructed is tangential to the source. As the source is a tangential current source, the circulating magnetic field cannot be found in the tangential plane. The maximum amplitude of magnetic field is found for the reconstructed normal component of the magnetic field Hy, at the plane containing the source. The reconstructed normal component of the magnetic field is shown in Figure 4-21. From the cross-sectional view through the X and Z axis along the dotted lines (Figure 4-21 (b)), it is clear that the magnetic field has a positive and negative maximum along the x-axis. This implies that there is an alternating magnetic field along the x-direction, which in turn indicates the current along the z-direction.

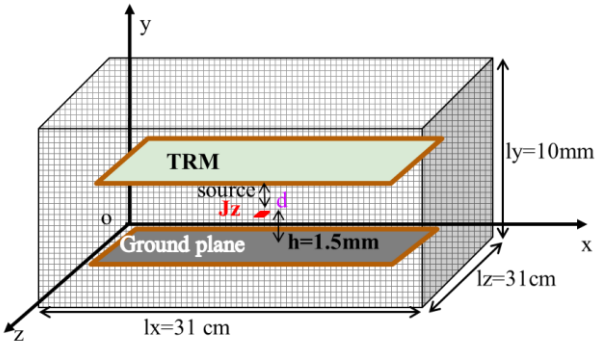

Figure 4-20 Horizontal current source Jz in the TLM mesh, d=1mm

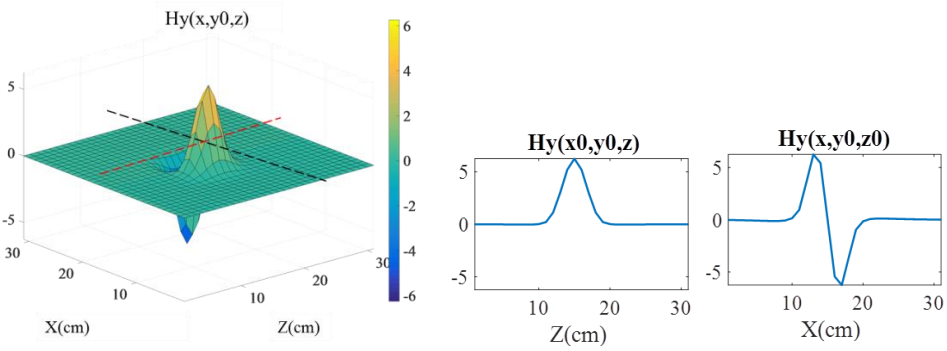

(a) (b)

Figure 4-21Real component of reconstructed magnetic field at the position of a current source Jz (a) Hy in the XZ plane (b) cross section along the dotted lines through the x and z-axis of (a)

4.3.2.6 Current source Jx

The same procedure is repeated for a tangential current source Jx (as shown in Figure 4-22). Among the reconstructed magnetic fields, the maximum value is found for the normal component as in the case of the current source Jz, but the axes are interchanged, which is obvious from Figure 4-23. It can be seen that the amplitudes of the reconstructed magnetic field are same and it has alternating peaks along the z-axis. This indicates the presence of the tangential current Jx.

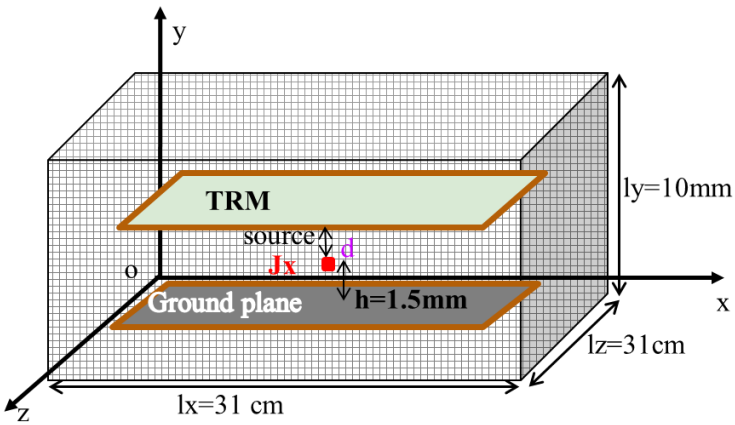

Figure 4-22 Horizontal current source Jx in the TLM mesh, d=1mm

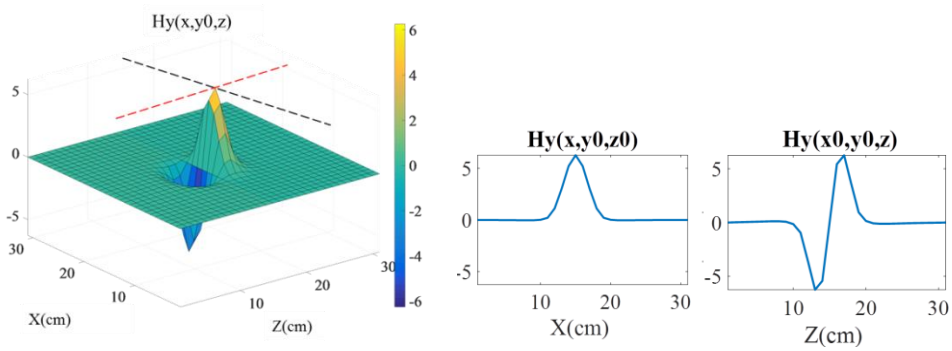

(a) (b)

Figure 4-23 Real component of reconstructed magnetic field at the position of a current source Jx (a) Hy in the XZ plane (b) cross section along the dotted lines through the x and z-axis of (a)

These results show that the normal component of the current can be identified from the two tangential magnetic field components and the tangential current can be identified from the normal component of magnetic field depending on the direction in which the magnetic field alternates. For a current along the x-direction, the normal component alternates along z-direction and vice versa.

4.3.3 Effect of near field scanning height on source reconstruction

In order to investigate the effect of the height between the source and the near field scanning plane, the simple example of the voltage source Vy, which is discussed before is considered here. The electromagnetic fields are recorded at different heights (d=1mm, 2mm, 3mm, 4mm) using the forward simulation. The source is reconstructed by using data from each height separately using the inverse propagation. The reconstructed E field at the plane containing the source is plotted in Figure 4-24 (a)-(d). The original field distribution at the position of the source, which obtained with the forward simulation, is compared with the reconstructed field at the same position. It is obviously seen from the figures that the width of the reconstructed pulse has increased when the height d increased from 1mm-4mm. Also, the increase in width of the reconstructed field is proportional to the height d.

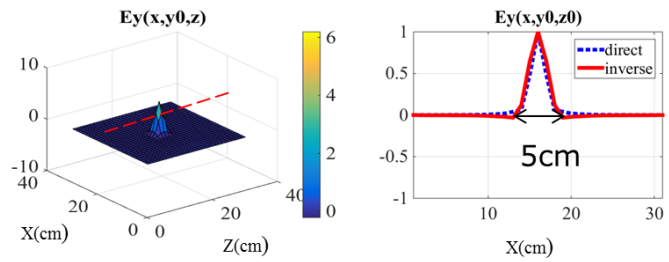

(a) d=1mm

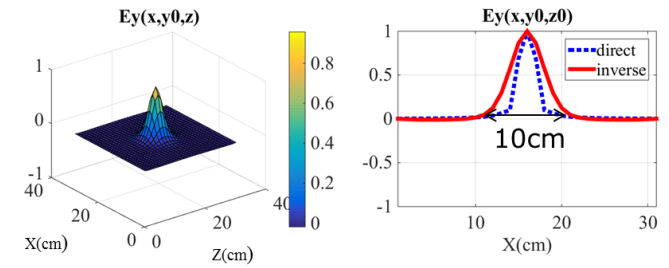

(b) d=2mm

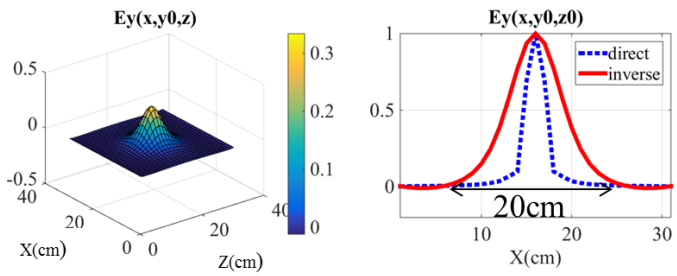

(c) d=3mm

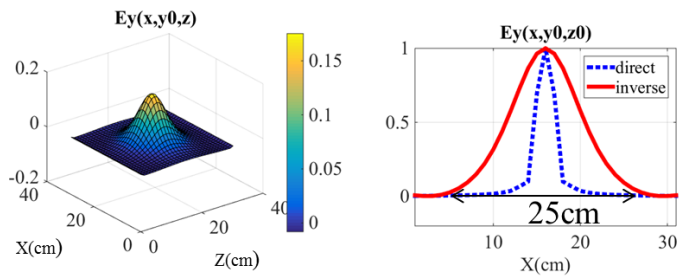

(d) d=4mm

Figure 4-24 Results of the reconstruction of the voltage source Vy using fields from a different height of the near field plane, d.

4.3.4 Spatial resolution

The spatial resolution is the distance between two sources that can be reconstructed by the inverse method. Two voltage sourcesEy, separated by a distance ‘s’ as shown in Figure 4-25 are simulated using forward using propagation. Inverse propagations are made using the fields recorded at 1mm

above the source for each value of ‘s’ in the forward propagation. The time steps in both the forward and inverse propagations are the same for all cases.

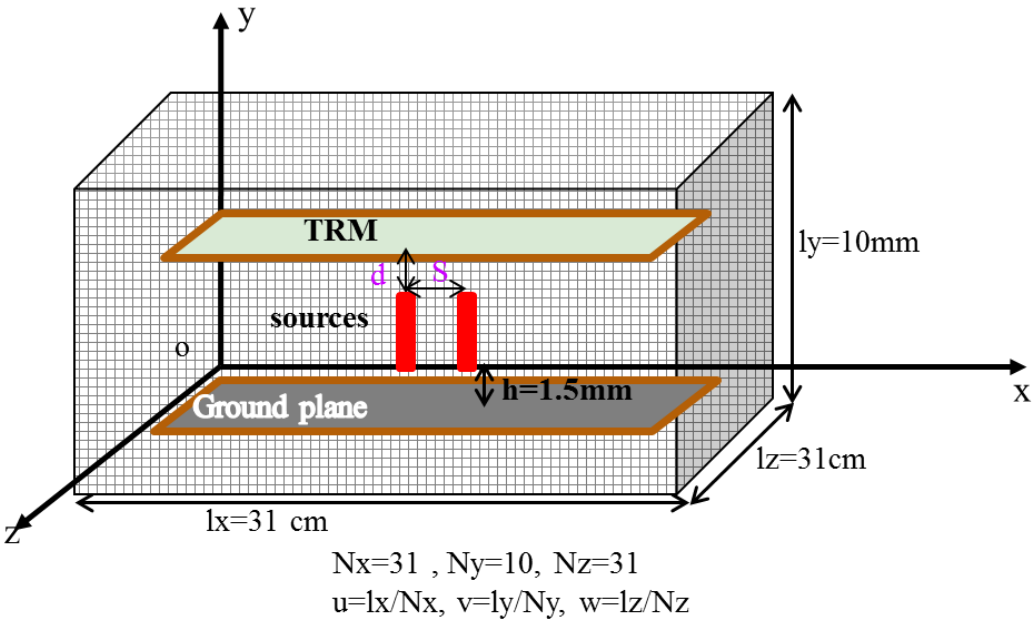

Figure 4-25 Two voltage sources separated by a distance s

Figure 4-26 (a) to (c) shows the real component of the reconstructed E fields for S=2mm, 3mm, and 4mm respectively. The reconstructed fields are compared with the original field present at the source position, which is obtained using direct propagation. The E field values at the position containing the position of the source, which is obtained after direct and inverse propagation are normalized with respect to its maximum value in order for the comparison. When the separation between the sources is 2u which is equal to 2cm, the reconstructed E field is not able to distinguish between the two sources. It is seen that there only one peak, which is in the middle of the two sources, this indicates that the source is a single voltage located source at the middle of the two sources. When the distance between them has increased to 3cm (3u), the two peaks are found in the reconstructed field at the same position of the source. When the distance between the sources is increased, the sources are reconstructed more accurately. The factor which limits the resolution of the reconstruction is the mesh parameter (u and v in this example).

In order to reconstruct the sources more accurately, the mesh parameter has to be reduced, that means the number of spatial sampling points in the near field recording has to be increased.

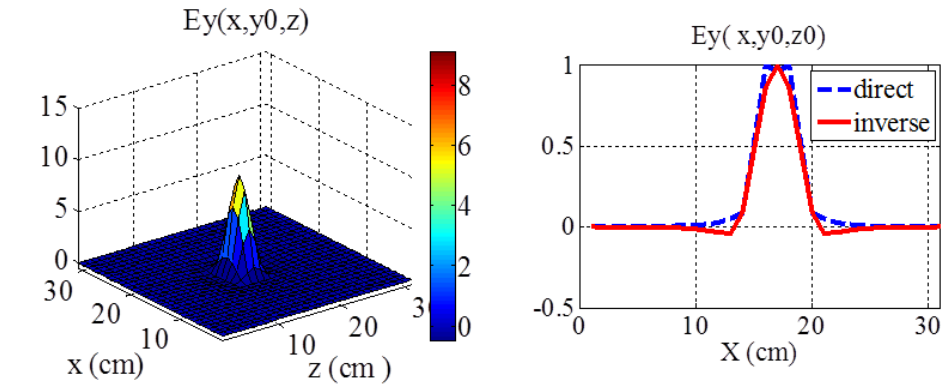

(a) S=2cm

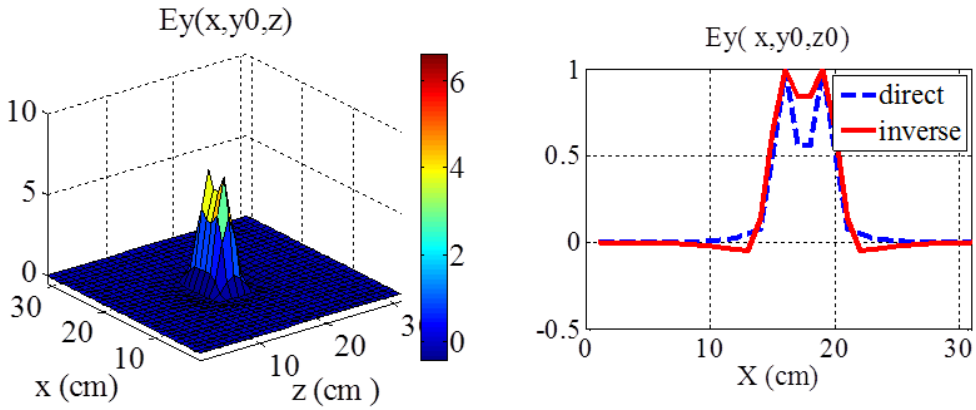

(b) S=3cm

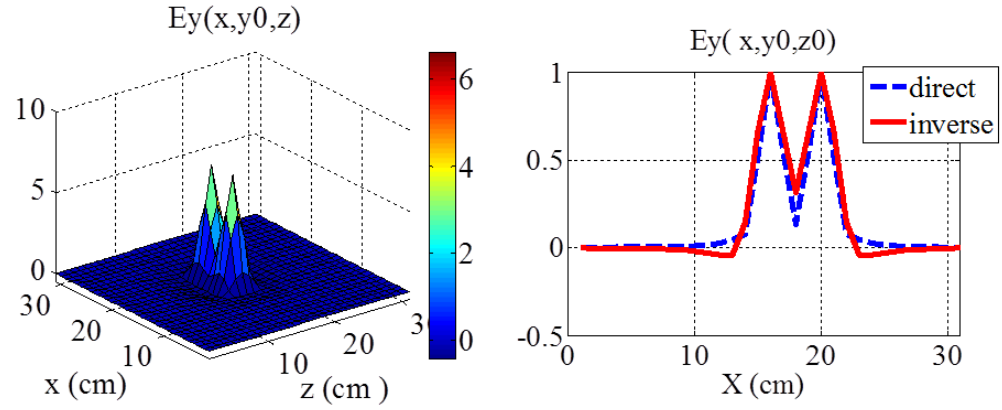

(c) S=4cm

Figure 4-26 Reconstructed normal component of E field of two voltage source Vy with a distance of separation 's' between them. (a) S=2cm (b) S=3cm (c) S=4cm

4.3.5 Application of frequency domain NFS data to time domain TLM method

The choice of using a time domain TLM method or frequency domain TLM method varies depending on the type of the problem to be solved. Although the relationship between the time domain and frequency domain TLM was not very clear until 2008, Z. Chen and M.M. Ney showed that there is a one to one correspondence between the two [28].

EMC measurements are carried out in the frequency domain.The near field scan (NFS) data contains the magnitude and phase of the magnetic field components at different frequencies. As the inverse transmission line matrix method is based on time reversal of electromagnetic waves it is not possible to apply the scanned data directly on its mesh. The discrete Fourier transform (DFT) of the time domain signal gives the corresponding frequency domain signal, and it is applicable in the case of TLM method as well [28], [29]. As per the properties of the Fourier transform, a delayed signal in the time domain corresponds to a phase shifted signal frequency domain.

$$F[x(t \pm t_0)] = X(j\omega)e^{j\omega t_0} \qquad 4\text{-}27$$

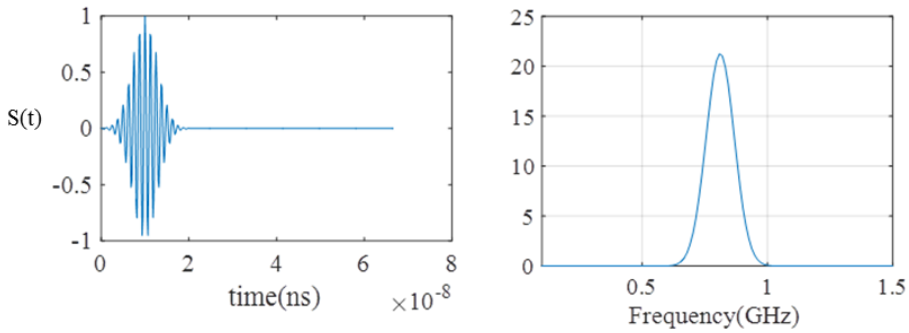

(a) (b)

Figure 4-27 (a) Sinusoidal Gaussian pulse used for superposition (b) Frequency spectrum

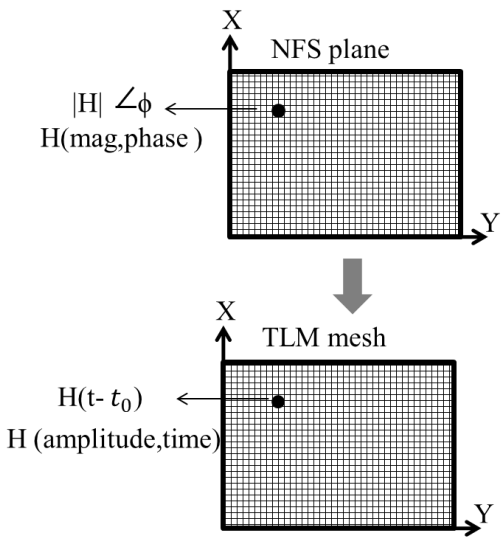

Figure 4-28 Application of the near field scan data to TLM mesh

The time delay t_0 of the propagated signal can be extracted knowing the amplitude and phase of the same signal. This time delay is applied to a reference signal centered at a frequency ω. During the reverse propagation, the maximum amplitude of the signal corresponds to the frequency ω. Figure 4-27shows sinusoidal Gaussian pulse used as the reference signal. The time period of this

signal can be denoted as t, the time delay between each point in the TLM mesh t_0 is applied on this signal to modify the period as $t \pm t_0$. The application of the NFS data on to the TLM mesh is shown schematically in Figure 4-28.

4.3.6 Calculation of equivalent source

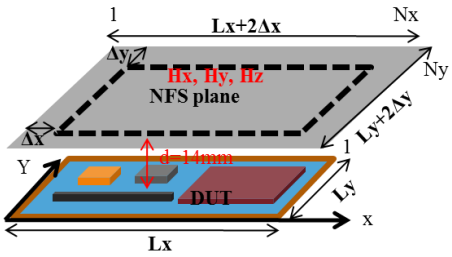

Figure 4-29 Arbitrary PCB showing the near field scanning plane

Consider an arbitrary PCB with dimensions Lx*Ly as shown in Figure 4-29. In order to make sure that all the fields from sources in the edges are covered, we have recorded the magnetic field in a plane which is larger than the area of the device under test. We have taken an extra length of Δx and Δy along the x and y-axis. So, the scanning area of the device under test will become Lx+2Δx * Ly+2Δy. The distance from the ground plane of the device under test to the near field scanning plane is marked as d in the figure.

A conductor above a ground plane is simulated using CST Microwave studio as shown in Figure 4-30. The length of the conductor is 12 mm, and it is oriented along the z-axis. The conductor which acts as a monopole is excited from the ground plane by a voltage 1V. The dimensions of the ground plane are 100mm x 100mm.

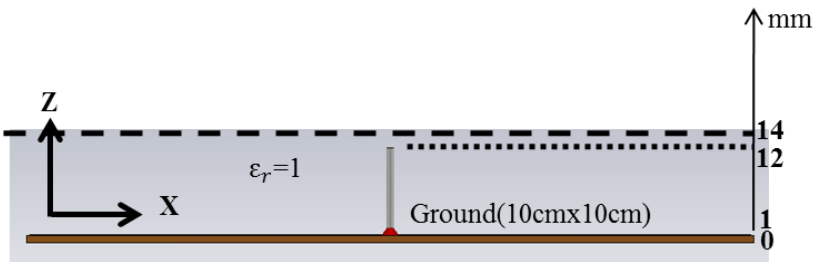

Figure 4-30 Monopole above a ground plane

The simulated magnetic field components Hx, Hy, Hz are recorded in the XY plane at a height 14mm above the ground plane. The Δx and Δx correspond to 4mm. The fields are recorded at 109 x 109 points and the distance of separation between each point is 1mm along the x and y directions. The absolute value of the magnetic fields above the DUT is plotted in Figure 4-31. The phase of the magnetic field at each point is extracted to calculate the time delay between the

adjacent points as described above. This time delay is applied to the sinusoidal Gaussian pulse along with its recorded amplitude at each point. These recorded magnetic fields are then time reversed to the TLM mesh (Figure 4-32). A ground plane of 109mm x 109mm is provided in the TLM simulation. The time-reversed magnetic field is then applied to the TRM located at 14mm above the ground plane. After the reverse propagation, the magnetic fields are recorded at 1mm above the ground plane. The reconstructed magnetic field components are shown in Figure 4-33. The magnetic fields are recorded at the time when the tangential component of magnetic field Hy has maximum amplitude in that plane. An alternating magnetic field for the tangential components Hx and Hy are found in the plane of the source, having the same value of the peak amplitude.

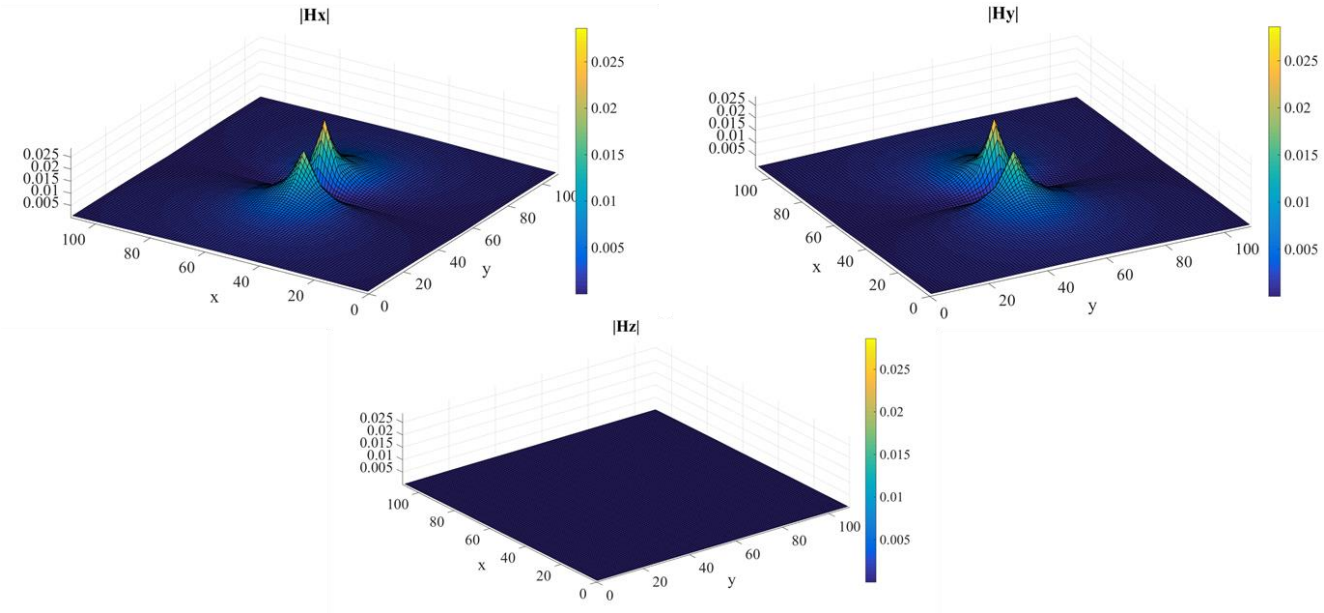

Figure 4-31 Simulated magnetic fields at 2mm above the monopole

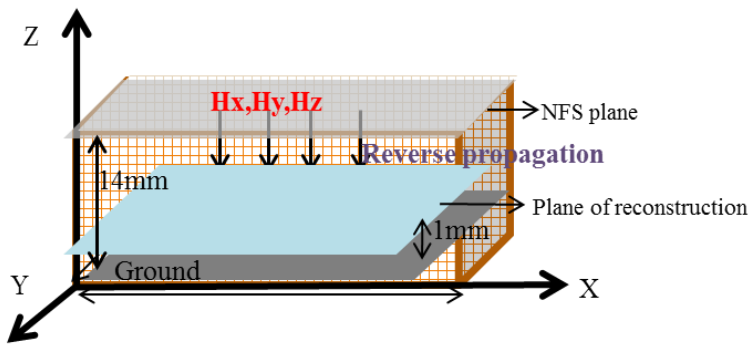

Figure 4-32 TLM cell for source reconstruction

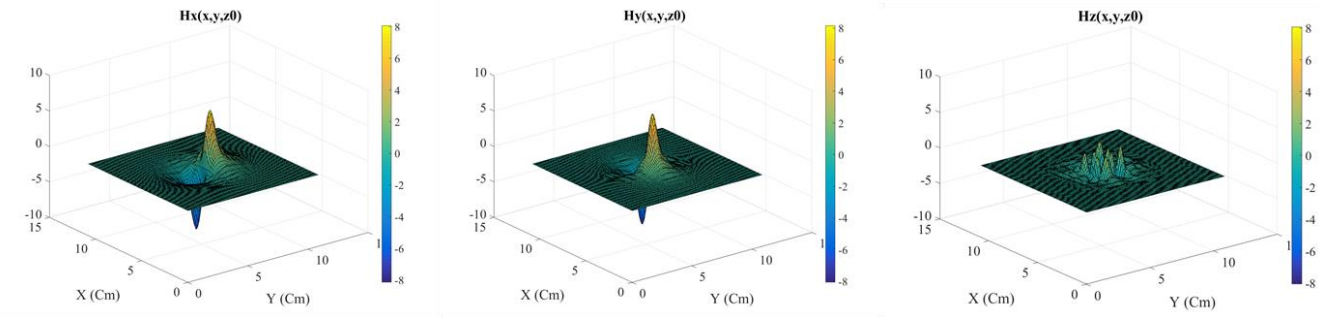

Figure 4-33 reconstructed magnetic fields in the XY plane at z=1

Now, it is required to find the position and orientation of the source or we need to calculate an equivalent source which gives the same far field as that of the device under test. As per Ampere's law, the integral of the magnetic field around a closed loop is related to the total current flowing across the surface enclosed by the loop (Figure 4-34).

$$\oint B.dl = \mu_0 I \qquad 4\text{-}28$$

Where B is the magnetic flux and μ_0 is the permeability of free space

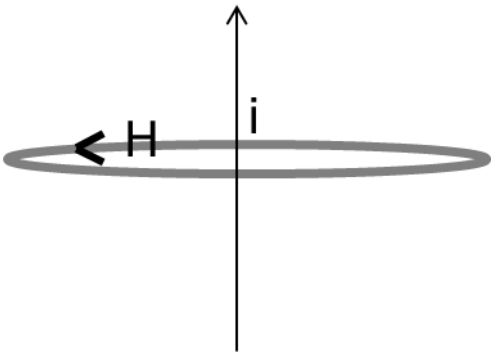

Figure 4-34 magnetic field of a current source

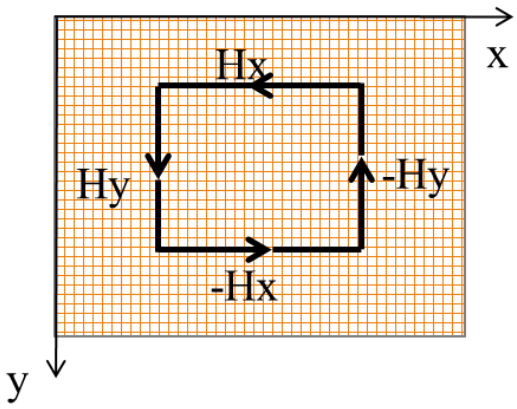

Figure 4-35Calculation of equivalent current

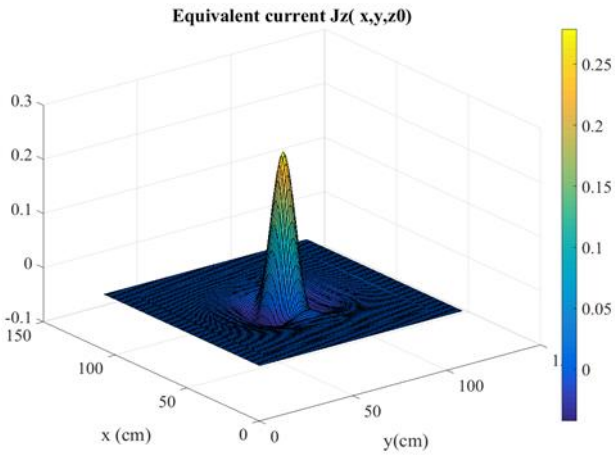

Figure 4-36 Calculated equivalent current of the monopole

So, the tangential magnetic field components correspond to the vertical current. In the XY plane, the circulation of the fields Hx and Hy is proportional to the current Jz (shown in Figure 4-35). The equivalent current calculated with this approach is shown in Figure 4-36. The position of the peak of the equivalent current is at (55, 55) which is exactly at the same position of the original monopole. The amplitude is proportional to the amplitude of the source, but it is not the exact amplitude. The position and orientation of the source are identified correctly.

4.3.7 Limitations of source reconstruction using Inverse TLM method

We have seen that with the inverse propagation of electromagnetic waves, we could reconstruct the fields at any plane below the NFS plane.

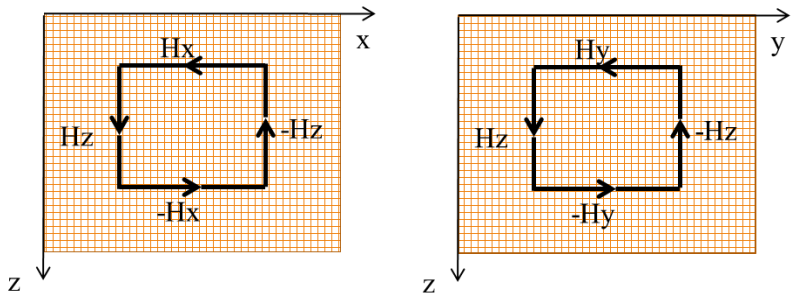

Figure 4-37 Circulation of magnetic field in the XZ and YZ plane (a) XZ plane (b) YZ plane

For a vertical current Jz, the circulation of the magnetic fields is in the XY plane. But the currents Jx and Jy have a circulating magnetic field in the YZ and XZ plane respectively as shown in Figure 4-37. As the distance from the source to the near field scanning plane is very small, it is not practical to calculate the circulating magnetic fields in these planes. Also, it takes a long time to compute the circulating fields in the XZ and YZ plane because the position and plane of the source

is unknown. Hence, it limits the calculation of the equivalent source for horizontal current sources i.e. current sources oriented along the x and y directions

4.4 Equivalent source by 2D cross-correlation method

4.4.1 2 D cross-correlation method

In the language of signal processing, cross-correlation is a measure of similarity of two series as a function of the displacement of one relative to the other. This is also known as a sliding dot product or sliding inner-product. The 2-D cross-correlation of an M-by-N matrix X and a P-by-Q matrix H is a matrix C of size M+P–1 by N+Q–1 given by

$$\mathrm{C}(\mathrm{k},\mathrm{l}) = \sum_{m=0}^{M-1} \sum_{\mathrm{n}}^{\mathrm{N}-1} X(m,n)\bar{H}(m-k,n-l) \qquad 4\text{-}29$$

Where, the bar over H denotes complex conjugation.

For example, consider the following 2-D cross-correlation:

$$X = \begin{matrix} 1 & 1 & 1 \\ 1 & 1 & 1 \end{matrix}$$

$$H = \begin{matrix} 1 & 4 \\ 2 & 5 \\ 3 & 6 \end{matrix}$$

The cross-correlation between X and H gives the matric C as follows

$$C = \begin{bmatrix} 6 & 9 & 9 & 3 \\ 11 & 16 & 16 & 5 \\ 9 & 12 & 12 & 3 \\ 4 & 5 & 5 & 1 \end{bmatrix}$$

The C(1,1) element in the output corresponds to C(1–3,1–2) = C(–2,–1) in the defining equation, which uses zero-based indexing. The C(1,1) element is computed by shifting H two rows upward and one column to the left. Accordingly, the only product in the cross-correlation sum is X(1,1)*H(3,2) = 6. Using the defining equation, we obtain

$$\mathrm{C}(-2,-1) = \sum_{m=0}^{1} \sum_{\mathrm{n}=0}^{2} X(m,n)\bar{H}(m+2,n+1) = \mathrm{X}(0,0)\bar{\mathrm{H}}(2,1) = 1 \times 6 = 6$$

with all other terms in the double sum equal to zero.

4.4.2 Formulation of the equations

The cross-correlation of the measured magnetic field with a magnetic field produced by a known current element will give the presence of that current element in the measured magnetic field. So, in equation 4-29 the function X can be referred to as the measured magnetic field and the function H can be referred to as a standard function.

As per equivalence theorem, any source of current can be determined from its tangential magnetic field components[30].

$$J = \hat{n} \times H \qquad 4\text{-}30$$

Where, H is the tangential magnetic field.

Then, the equation 4-29 can be modified as

$$\mathrm{C(k,l)} = \sum_{m=0}^{M-1} \sum_{\mathrm{n}}^{\mathrm{N}-1} X_{pt}(m,n)\bar{H}_{pt}(m-k,n-l) \qquad 4\text{-}31$$

Xpt is the tangential magnetic field radiated from the DUT. $\bar{H}_{pt}$is the complex conjugate of the standard function.

In a 3-D space, a current element has two tangential magnetic field components as the magnetic monopoles don't exist. The above equation can then be written as,

$$\mathrm{C(k,l)} = \sum_{m=0}^{M-1} \sum_{\mathrm{n}}^{\mathrm{N}-1} X_{pt1}(m,n)\bar{H}_{pt1}(m-k,n-l) \times \sum_{m=0}^{M-1} \sum_{\mathrm{n}}^{\mathrm{N}-1} X_{pt2}(m,n)\bar{H}_{pt2}(m-k,n-l) \qquad 4\text{-}32$$

Where,$\bar{H}_{pt1}$and$\bar{H}_{pt2}$ is the standard function for the two tangential magnetic field components. It is the complex conjugate of the tangential magnetic field calculated using 4-29. The suffix p indicates the orientation of the dipole (x y or z). The parameters t1 and t2stands for two tangential magnetic field components for each configuration of dipole. So, for a dipole oriented along z axis, the suffix pt1 and pt2 corresponds to x and y components. The individual summations terms in 4-32 are the 2-D cross correlation. The position of the equivalent source is the position at which the product of the cross correlation has a peak value.

4.4.2.1 *Derivation of the standard function*

Consider a short current filament illustrated in Figure 4-38. A current with amplitude I, angular frequency ω extends from –dl/2 to dl/2. Of course, a real current element couldn't start and stop abruptly like this, however realistic current distributions can be modeled by a superposition of current elements like this. The potential due to this current element at a point p can be expressed as [31].

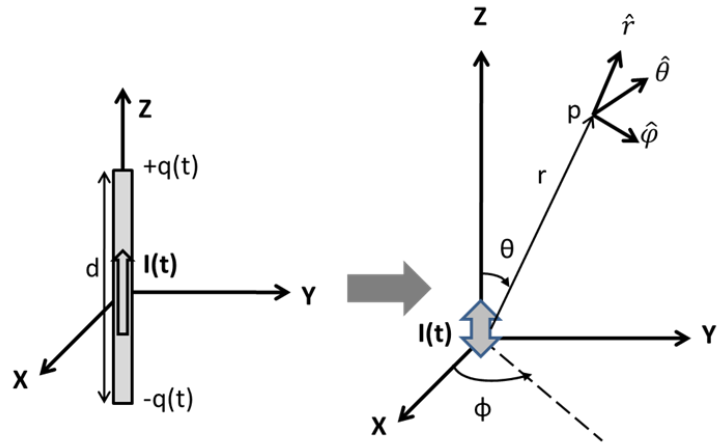

Figure 4-38 A current element oriented along the z axis

$$\overrightarrow{A_p} = \hat{z}\,\frac{\mu_0 d}{4\pi r} I e^{-jkr} \qquad 4\text{-}33$$

As the current is oriented along the z-axis, the above equation can be written in spherical coordinates as

$$\overrightarrow{A_p} = (\hat{r}\,cos(\theta) - \hat{\theta} sin(\theta))\frac{\mu_0 d}{4\pi r} I e^{-jkr} \qquad 4\text{-}34$$

Magnetic field is then calculated by applying the curl of the vector potential

$$H = \frac{\nabla \times \overrightarrow{A_p}}{\mu_0} = (\mu_0 r^2 sin\,\theta)^{-1} det \begin{vmatrix} \hat{r} & \hat{\theta} & \hat{\varphi} \\ \frac{\partial}{\partial r} & \frac{\partial}{\partial \theta} & \frac{\partial}{\partial \varphi} \\ A_r & A_\theta & A_\varphi \end{vmatrix} \qquad 4\text{-}35$$

$$\vec{H} = j(kId\eta_0/4\pi r)\, e^{-jkr}\left[1 + \frac{1}{jkr}\right]\sin\theta \qquad 4\text{-}36$$

The E field is then obtained by applying Faraday's law

$$\vec{E} = j(kId\eta_0/4\pi r)\, e^{-jkr}\left\{\hat{r}\left[\frac{1}{jkr} + \frac{1}{(jkr)^2}\right]2\cos\theta + \hat{\theta}\left[1 + \frac{1}{jkr} + \frac{1}{(jkr)^2}\right]\sin\theta\right\} \qquad 4\text{-}37$$

The standard function in rectangular coordinates can be calculated by applying spherical to Cartesian conversion.

4.4.3 Algorithm for finding the equivalent source

1. Obtain the near field scanned data, i.e. the magnetic fields (Hx, Hy, and Hz) at a distance 'd' above the DUT in the XY plane at a frequency f. The dimensions of the plane are m x n. The plane is divided into M points along the x-axis and N points along the y-axis. The distances between the points along the x and y-axis are dx and dy respectively.

$$dx = \frac{m}{M} \qquad 4\text{-}38$$

$$dy = \frac{n}{N} \qquad 4\text{-}39$$

Where m and n are the dimensions along x-axis and y-axis respectively.

Hx (x, y) , x=1…. M, y=1……N

Hy(x, y) , x=1…. M, y=1……N

Hz(x, y) , x=1…. M, y=1……N

2. Compute the standard function at the same plane at the position of the source. The source is assumed to be at (x0,y0)=((K+1)/2,(L+1)/2)

For a current source Jz calculate Hx1(x,y) and Hy1(x,y), x= 1 …….K, y =1…….L

For a current source Jx calculate Hy2(x,y) and Hz2(x,y), x=1 …….K, y= 1…….L

For a current source Jy calculate Hx3(x,y) and Hz3(x,y), x= 1 …….K, y= 1 …….L

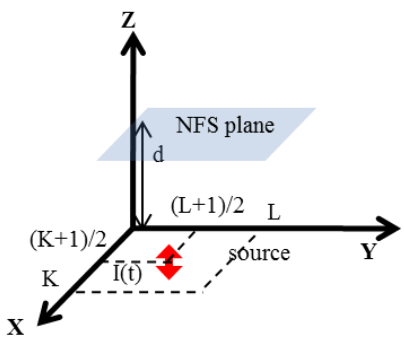

Figure 4-39 Parameters of the source in the standard function

3. Compute the 2D cross-correlation between the measured signal and the standard function

For a current source Jz

$$C1_Jz = H_x \times H_{x1} \qquad 4\text{-}40$$

$$C2_Jz = H_y \times H_{y1} \qquad 4\text{-}41$$

For a current source Jy

$$\mathrm{C1_Jy} = H_x \times H_{x2} \quad 4\text{-}42$$

$$\mathrm{C2_Jy} = H_z \times H_{z2} \quad 4\text{-}43$$

For a current source Jx

$$\mathrm{C1_Jx} = H_y \times H_{y3} \quad 4\text{-}44$$

$$\mathrm{C2_Jx} = H_z \times H_{z3} \quad 4\text{-}45$$

The resultant matrix after cross-correlation will be of size (M+K-1) (N+L-1).

The results of the cross-correlation will have a maximum value when the analytical function matches with the simulated field.

4. Fit the results of correlation to the scanning plane of the PCB.

   The size of the matrix after performing will be larger than the dimensions of the PCB. To locate the sources on the DUT, the size of the resultant matrix should be identical to that of the DUT.

   As the source is assumed to be at K+1/2, L+1/2 and the size of the standard function is (K, L), the first (K-1)/2 points and last (K-1)/2 points don't represent any sources. So, this part has to be eliminated from the matrix and the resultant matrix will have (M, N) points and each point corresponds to that of the device under test.

   so, the number of points in the matrix after subtraction is

$$\left((\mathrm{M}+\mathrm{K}-1) - 2\left(\mathrm{K} - {}^{1}/_{2}\right)\right) \times \left((\mathrm{N}+\mathrm{L}-1) - 2\left(\mathrm{L} - {}^{1}/_{2}\right)\right) = (\mathrm{M}, \mathrm{N}) \quad 4\text{-}46$$

5. Find the position of all the peaks for each correlation function, where the correlation function has maximum values.
6. A source Jz is found to exist at a position (Xp,Yp) if and only if both C1_Jz and C2_Jz has a peak at (Xp, Yp). Similarly, a current source Jy exist at (Xp,Yp) if and only if both the correlations C1_Jy and C2_Jy has a peak at (Xp,Yp). And a current source Jx exist at (Xp,Yp) if both the correlations C1_Jx and C2_Jx has a peak at (Xp,Yp).

4.4.4 Validation by application to elementary currents

In order to validate the proposed method, the algorithm is applied to 3 current sources oriented in 3 different directions. As it is a theoretical problem, the near field scanned data is simulated magnetic fields, instead of the measured magnetic field. The simulations here are carried out using the simulation software CST microwave studio. The procedure is explained in detail for a current source oriented along z-direction in the following section. And later, the results of the current sources along x and y directions after following the same procedure are given.

4.4.4.1 *Current source Jz*

A conductor of length 12mm is connected to the signal of a 50-Ohm coaxial cable. The coaxial cable is then excited by a current of 1A. The three components of magnetic fields are then recorded at the frequency 800 MHz.The distance between the top of the structure to the near field plane is 2mm. The inner dielectric of the coaxial cable is Teflon. The current carrying conductor is oriented in the z-direction as shown in Figure 4-40. The fields are recorded in XY plane in an area of 109mm x 109mm. The absolute values of the recorded magnetic fields above the source, Hx, Hy, and Hz are shown in Figure 4-41.

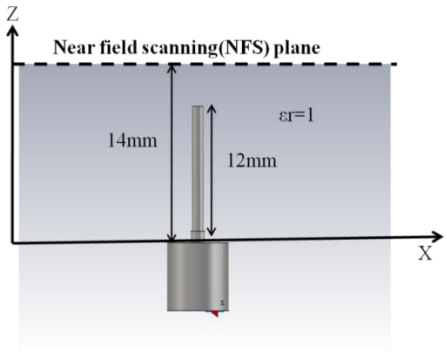

Figure 4-40 Simulated structure of the current source (Jz) from CST

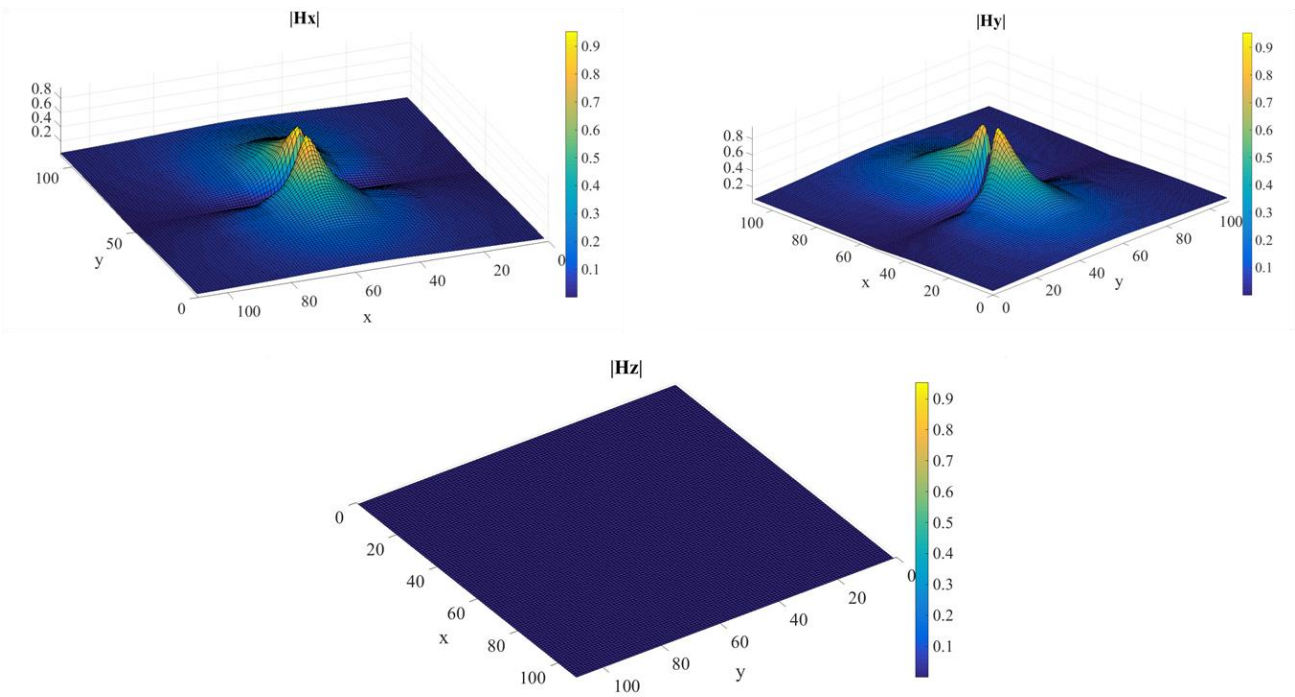

Figure 4-41 Simulated magnetic fields at 2 mm above the structure

The standard function at this same plan is then calculated using the equation 4-36. The standard function used here is only one dimensional (1-D) that is the magnetic fields are calculated either

along the x-direction or along the y-direction depending on the current source to be found. The position of the source used for the standard function is shown in Figure 4-42. The source is assumed to be at (5, 5). The window size of the standard function is chosen as 9mm along each direction. The fields at 14mm due to the current element are plotted in Figure 4-43 for all the three orientations, i.e., for a current source along x-direction (Jx), a current source along y-direction (Jy) and a current source along z-direction (Jz).

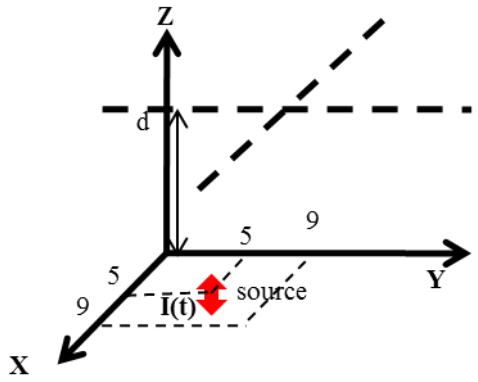

Figure 4-42 Position of the source used for standard function

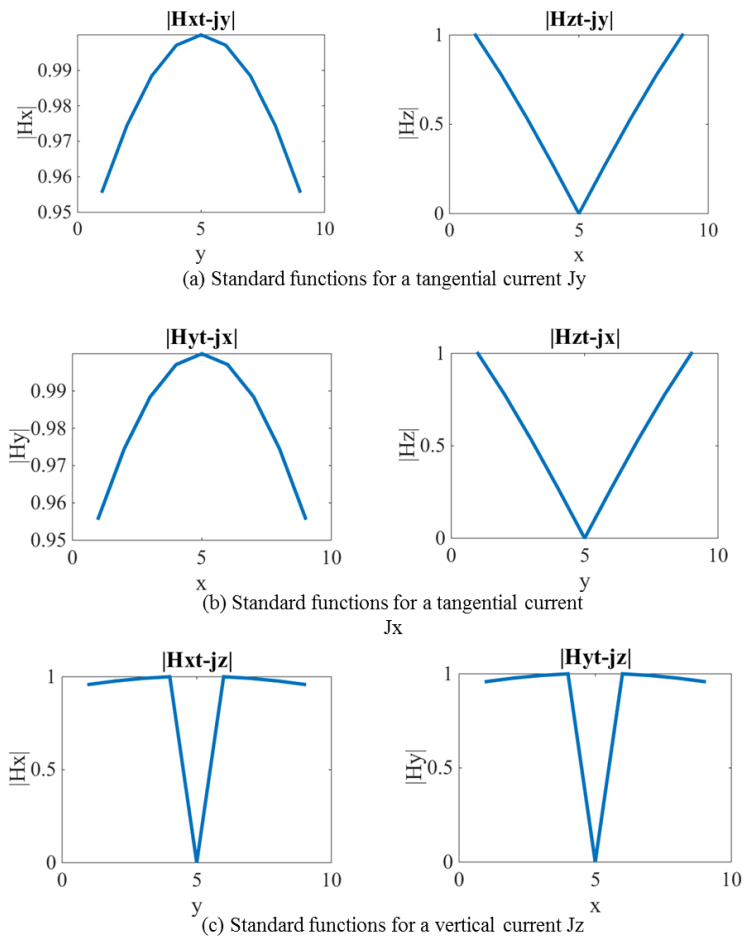

Figure 4-43Standard functions at 14mm above the source

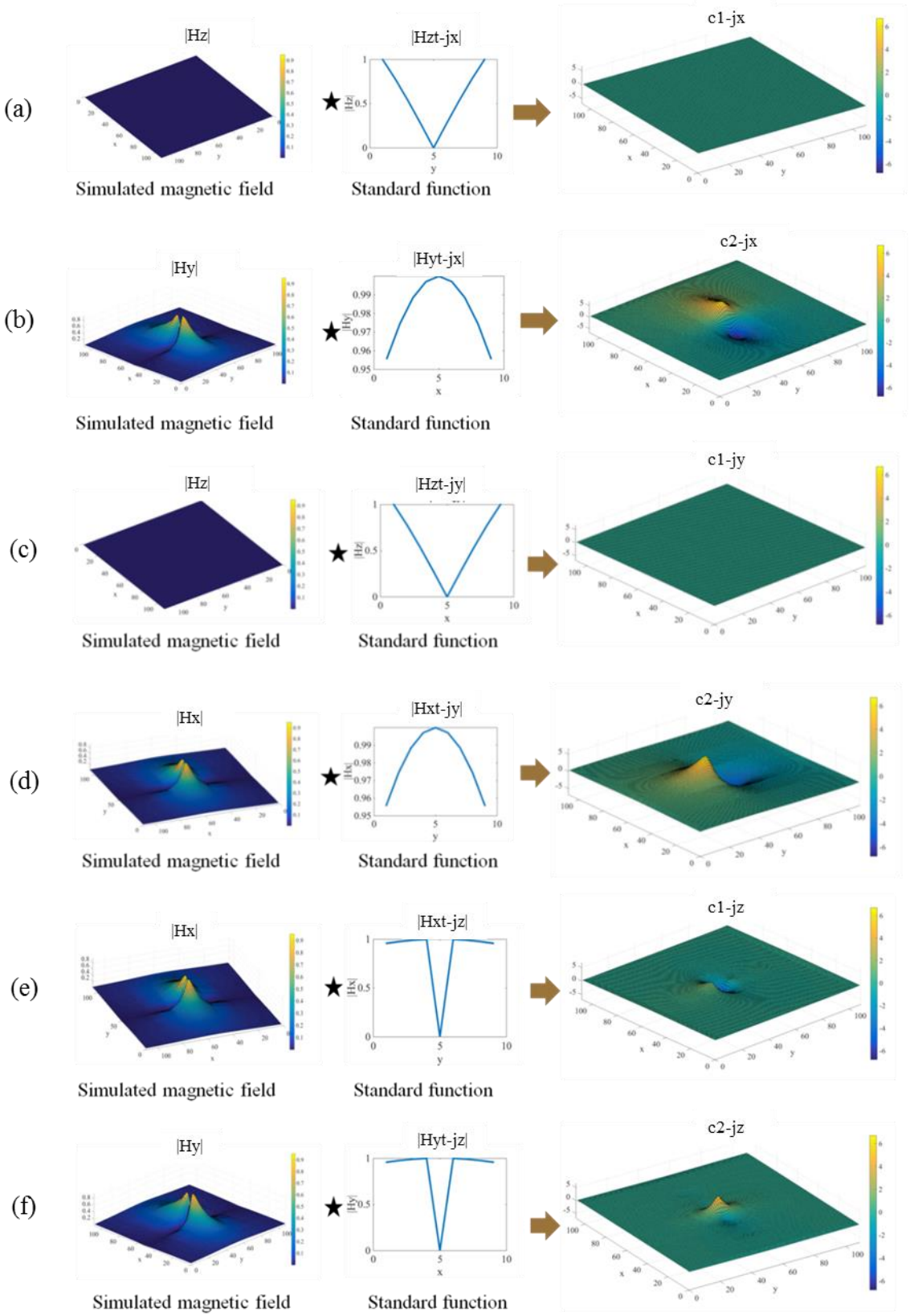

Figure 4-44 Results of 2D cross correlation

The magnetic fields are chosen either along the x-direction or y-direction depending on the polarization of the current. For a current along the z-direction, the magnetic fields are Hx and Hy. This magnetic field circulates in the xy plane. For the x component of magnetic field, the field

alternates in the y-direction. i.e., a positive and negative maximum of the field is only along the y-direction. The y component of magnetic field Hy alternates in the x-direction. The presence of these two alternating fields indicates the current source at the middle of the two maximums. For the current Jx, the tangential magnetic field components are Hy and Hz. But there is no circular magnetic field in the xy plane for this current. The Hz component is normal to the xy plane and will have an alternating maximum and minimum along the y-direction. The same is the case of a current Jy, except that the Hz component varies along the x-axis. These features of the current sources are taken in the standard function.

Now, cross-correlations are performed between the simulated data and the standard function. To identify the presence of each source, two cross-correlations have to be performed. Figure 4-44 shows the result of all the six cross-correlations. In the first plot Figure 4-44 (a), the correlation between the simulated Hz and the Hz of the standard function of Jx is performed, which is zero because there is no Hz component in the simulated field. The correlation between the simulated Hy and the standard function Hy of Jx gives two peaks in Figure 4-44(b), which doesn't correspond to two sources.

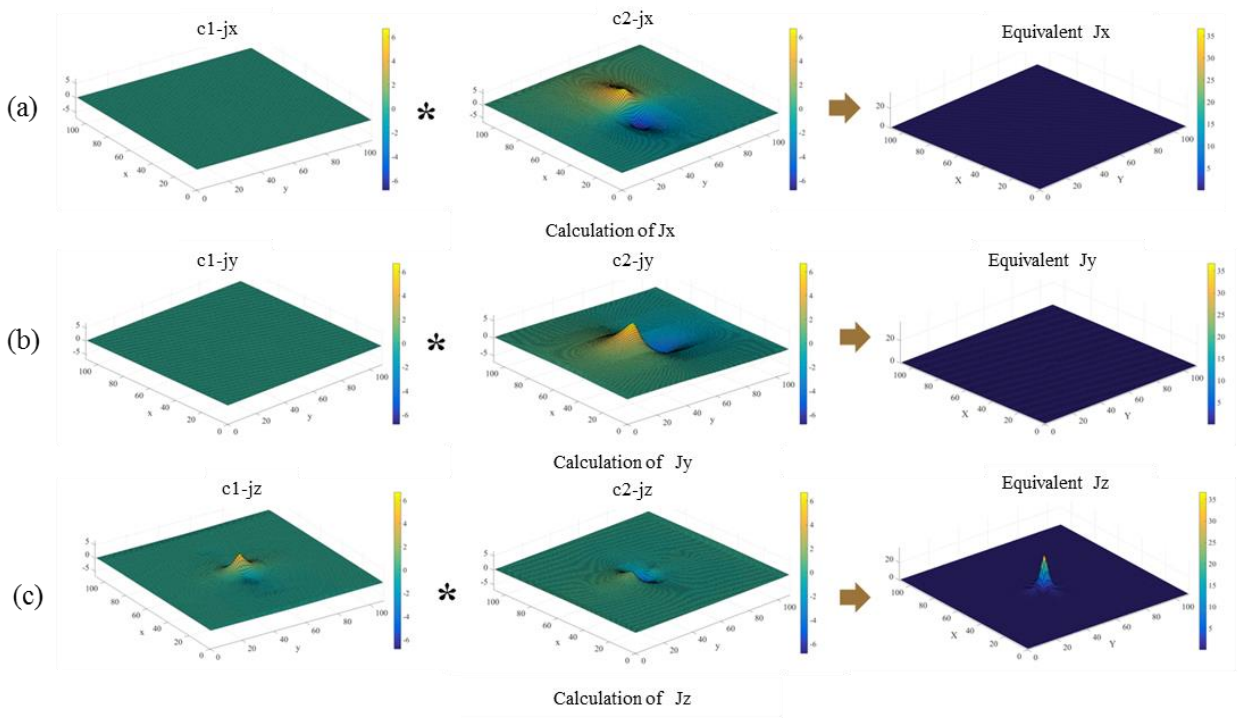

Figure 4-45 Calculated equivalent source

These two resultant cross-correlations when multiplied cancels all the peaks and results in zero as shown in Figure 4-45 (a), which means that the source is not equivalent to current source Jx. Similarly, Figure 4-44 (c) and (d) shows the cross-correlated results for the current source Jy. As the

normal component of Jy doesn't correspond to that of a current Jy, there is no common peaks at the cross correlation, and it results in zero in the equivalent current is Jy, as in Figure 4-45 (b). A peak is found in Figure 4-44 (e) and (f), and the peaks are in the same position. This indicates the source is equivalent to a current Jz and it gives a peak at the position of the source in Figure 4-45 (c).

4.4.4.2 Current source Jx

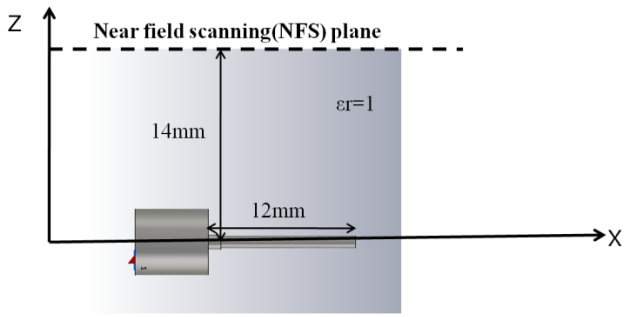

Figure 4-46 Simulated structure of the current source (Jx) from CST

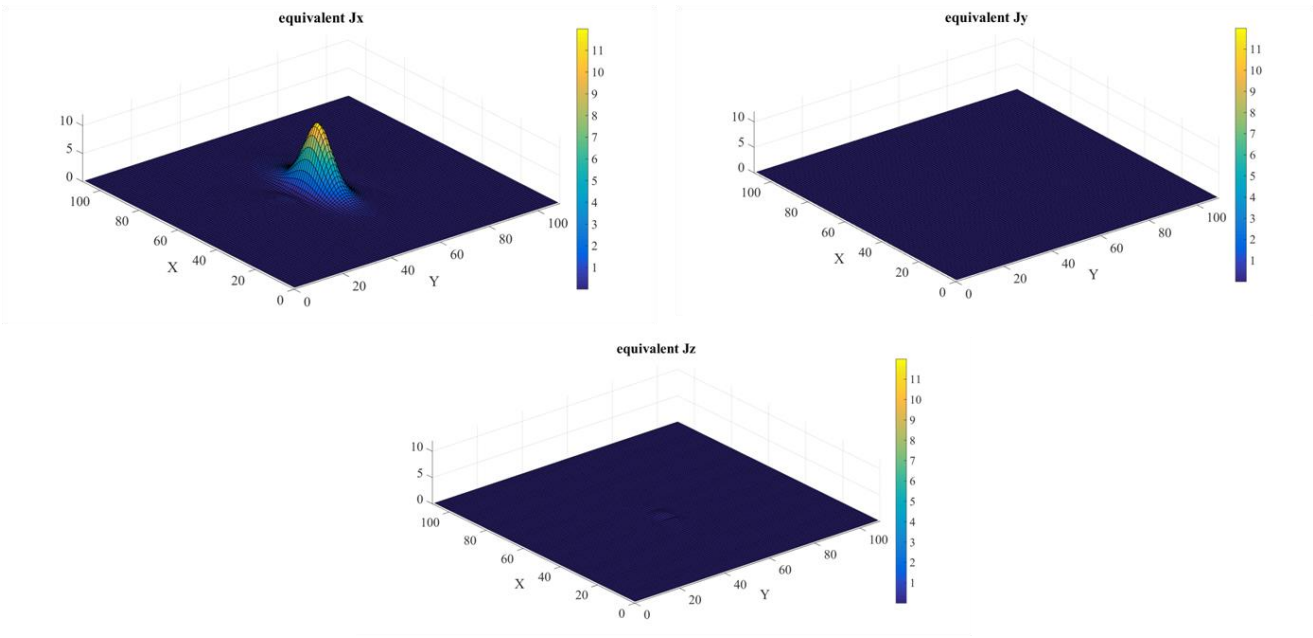

Figure 4-47 Equivalent source

In order to validate the algorithm for tangential currents, the same structure has simulated in CST, with the direction of the current element along the x-axis as shown in Figure 4-46. The three magnetic field components have recorded at 14mm above the structure from the centre of the coaxial connector. The magnetic fields have recorded in the same XY plane as before. The coaxial connector is excited with a current of magnitude 1A. As the current carrying conductor is oriented along the x-direction, the expected equivalent current is Jx. After applying the recorded magnetic field to the developed algorithm, the equivalent currents obtained has plotted in Figure 4-47. The

only peak observed is in in the equivalent current Jx, which is the same as the expected equivalent current.

4.4.4.3 Current source Jy

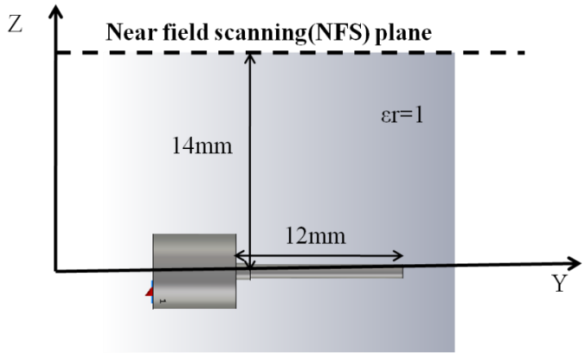

Figure 4-48 Simulated structure of the current source (Jy) from CST

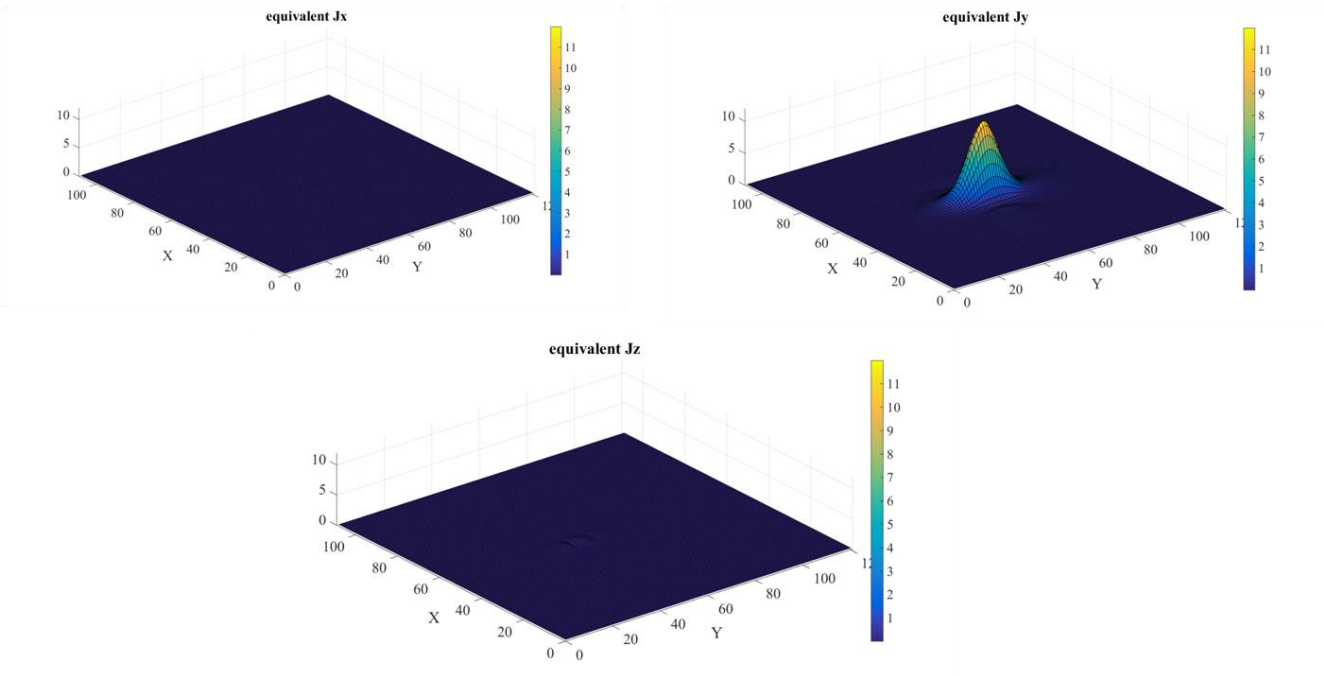

Figure 4-49 Calculated equivalent current

The direction of the above-discussed current source has made to be along the y-axis as shown in Figure 4-48. Therefore, the current is Jy. The three magnetic field components have recorded at 14mm above the structure using CST. The coaxial cable is excited with a current of 1A at 800MHz. The equivalent source obtained for this current after following the developed procedure has plotted in Figure 4-49. The equivalent currents Jx and Jz are zero and the only peak found is in equivalent current Jy, which is at the same position of the original source.

The developed algorithm is able to identify and localize the elementary current sources. As the method uses scalar multiplication, the phase of the detected current may not be the same as the

original current. But the polarization and the position of the elementary current sources are found accurately.

4.4.4.4 Two Current source

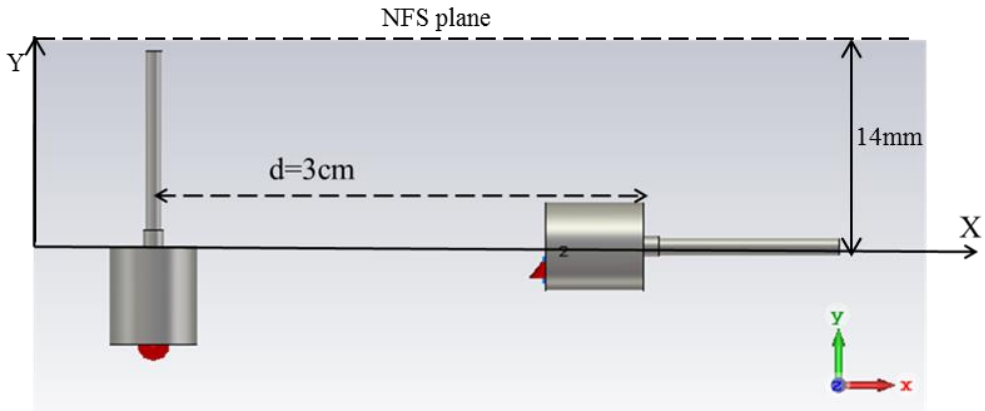

Figure 4-50 Two current sources separated by a distance of 3cm

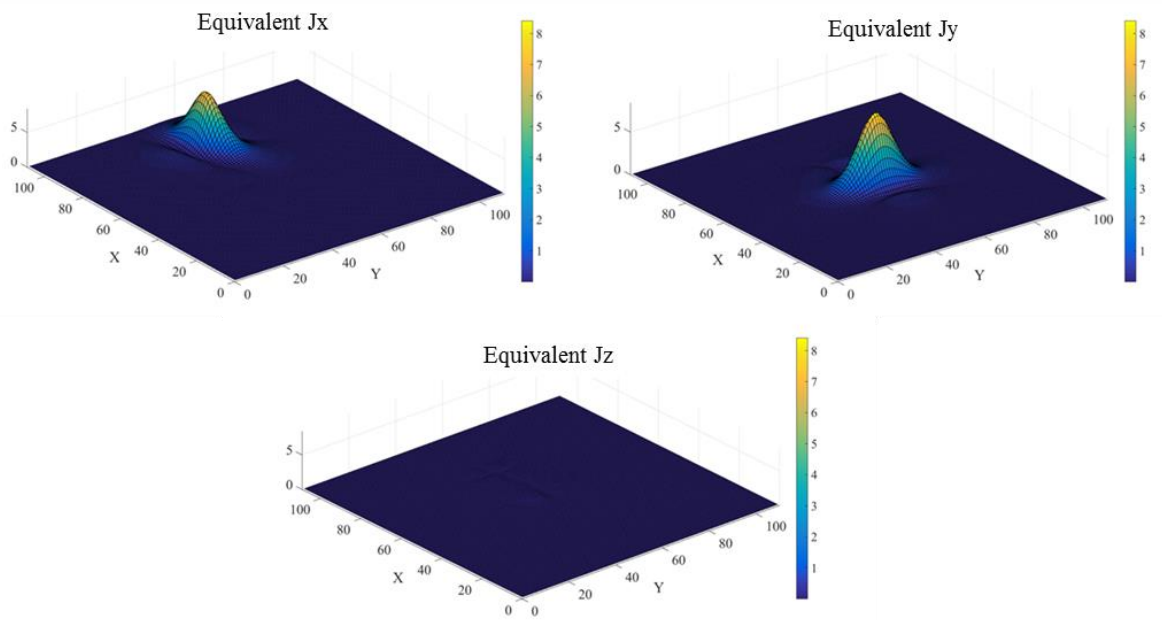

Figure 4-51 Calculated equivalent current of the two current sources

Two current sources Jy and Jx are placed at a distance 3 cm as shown in Figure 4-50. The magnetic field is again recorded in the XY plane at a height 14 mm (Z=14mm). The window size used in the standard function is the same as in Figure 4-43. Both the current sources are excited with a current of 1A. The calculated equivalent current shows that the source is plotted in Figure 4-51. It corresponds to an equivalent current Jx and Jy. The equivalent current Jx is oriented along the x-direction and equivalent current Jy is oriented along y-direction as in the original source.

4.4.4.5 *Effect of the window size of the standard function*

In order to understand the influence of the window size of the standard function of the developed algorithm, the example of two current sources discussed in the previous section is made under study. At First, a 2-D window of size 9mm x 9mm as shown in Figure 4-52 is taken for the standard function. It shows the normalized value of magnetic fields at 14mm above the ideal currents. In this case, the source is assumed to be at the center of the window (5, 5). The equivalent source obtained with this window is shown in Figure 4-53. It is able to detect the equivalent sources correctly, in the same position as that of the original sources. The amplitude of the equivalent source is very high compared to that of Figure 4-51, which is obviously due to the more number of cells taken for cross-correlation. Another important fact to be noted is that the width of the calculated equivalent source has increased.

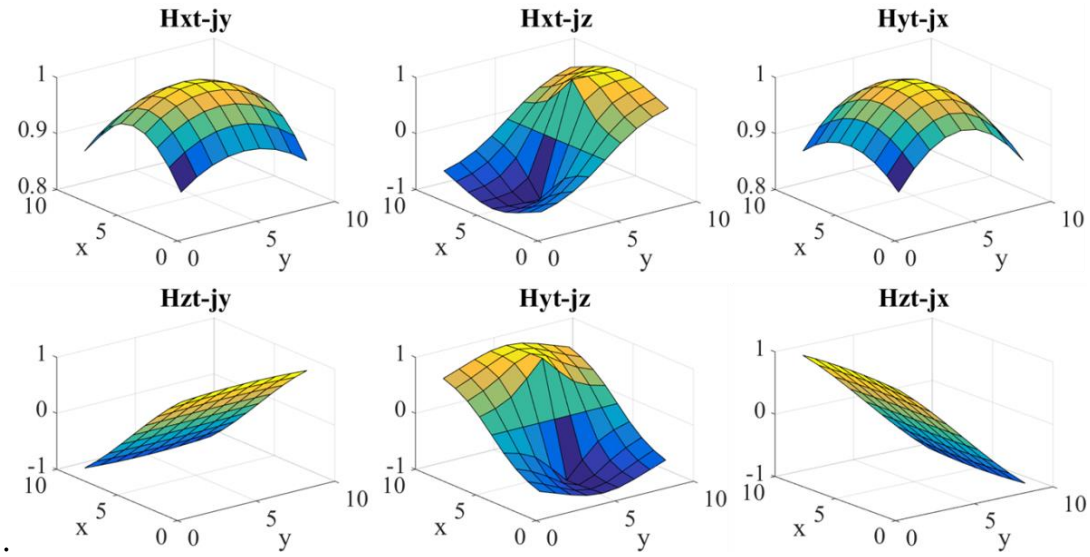

Figure 4-52 standard functions for a window size of 9mm x 9mm

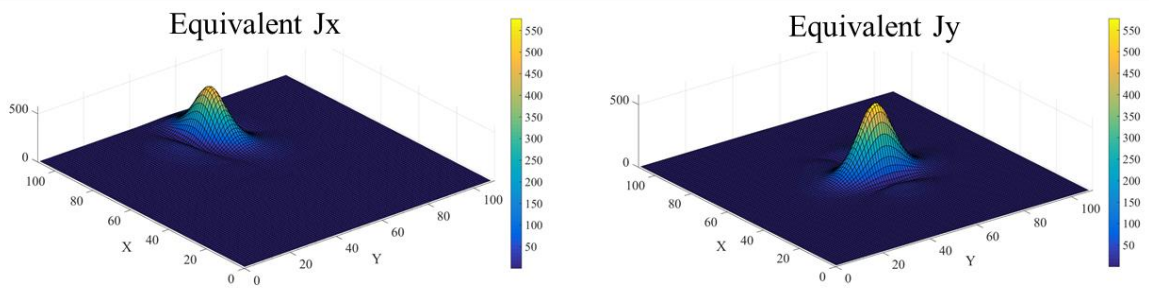

Figure 4-53 Equivalent currents obtained with a window size of 9mm x 9mm.

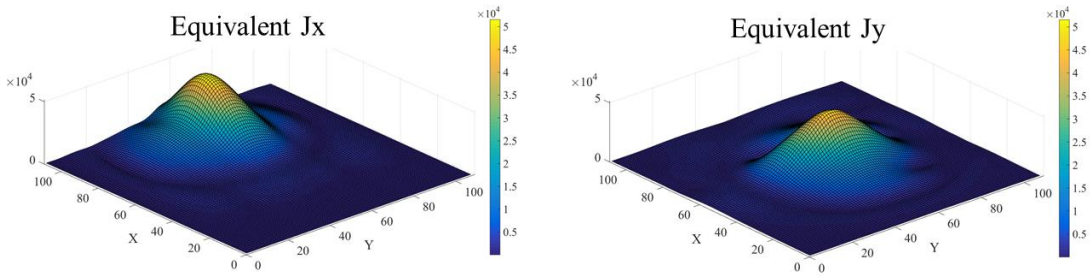

Figure 4-54 Equivalent currents obtained with a window size of 109mm x 109mm.

The window size is made equal to that of the size of the near field scanning plane i.e., 109 mm x109 mm. Figure 4-54 shows the equivalent currents obtained with this window size. The equivalent source is again identified correctly at the same positions. The amplitude is increased due multiplication as expected. The width of the equivalent current is broadened and is broader than the ones obtained with 9mm x 9mm. This may result in the wrong identification of the equivalent source when the sources are placed close to each other. Hence, it can be concluded that as the window size of the standard function increases the accuracy of the calculated equivalent source decreases. The 1D window size of 9mm along x-direction or along y-direction is optimized to give the accurate equivalent sources.

4.4.5 Application to PCBs on air

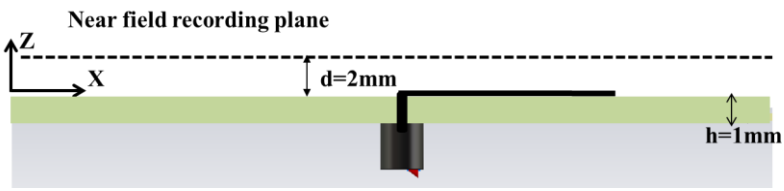

(a)

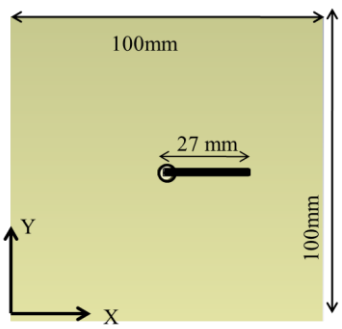

(b)

Figure 4-55 Structure and dimensions of the PCB with coaxial fed metallic strip (a)Cross-sectional view of the coaxial fed metal strip (bend monopole) (b) Top view of the coaxial fed metal strip (bend monopole)

In order to validate the feasibility of thee developed source reconstruction method, a bend in a monopole on an air substrate is taken as a PCB and is simulated using CST microwave studio. The structure is excited by 1 V through a coaxial cable below the PCB (Figure 4-55). The three components of magnetic field (Hx, Hy, Hz) is recorded at 2mm above the top of the PCB at a frequency 800 MHz (shown in Figure 4-56). The reconstructed equivalent currents are shown in Figure 4-57. The equivalent source is identified as a Jx and Jy, i.e. a current along x axis and a current along y axis. The amplitude of the reconstructed current is not the same as the original source current, but the position and orientation of the source is identified correctly. The two major peaks appear as equivalent current Jx and Jz. But there is also two small peaks found for the equivalent current Jy which don't correspond to the original source. In this case, it is required to incorporate the knowledge about the device under test in order to determine the equivalent sources correctly. The electric field radiated by this equivalent source at 1m is calculated in the next section.

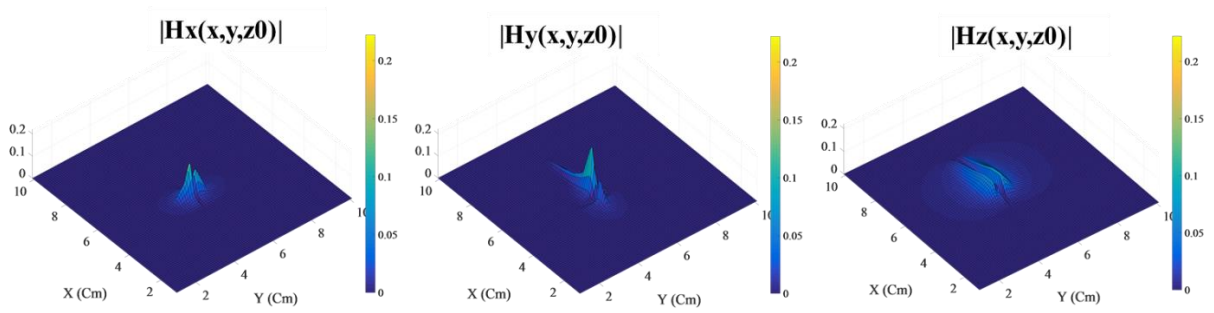

Figure 4-56 Simulated magnetic field at 2mm above the PCB

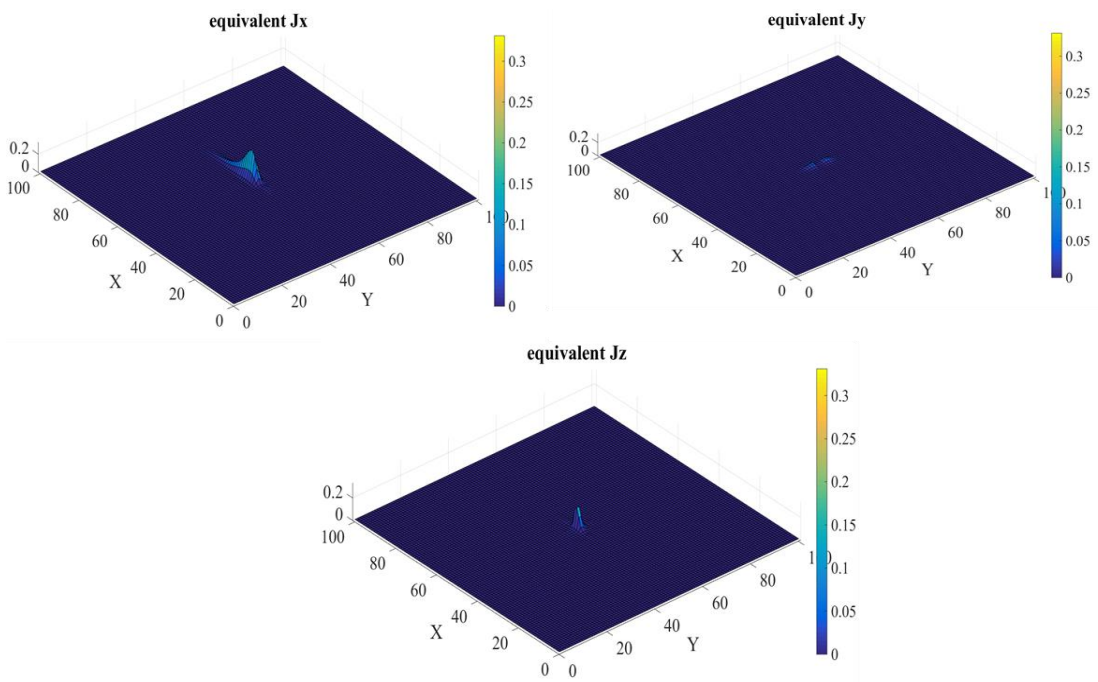

Figure 4-57 Calculated equivalent currents of the bent monopole

4.5 Prediction of the radiated field

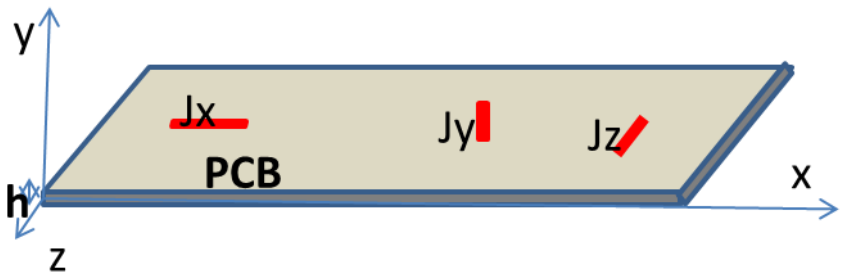

Figure 4-58 Equivalent sources on PCB

The equivalent source represents the source distribution which gives the same far field radiated by the original source. The equivalent sources are identified as either as current Jx, Jy, Jz or the combination of these currents as in Figure 4-58. Knowing the equivalent currents it is possible to calculate the fields radiated from the sources at any distance away from the source. In order to validate the reconstruct equivalent source, it is necessary to predict the radiated fields which involve the calculation of the far field radiated by the equivalent source. The radiated field is calculated from the current density using the far field integrals discussed in the following session.

4.5.1 Far field integral

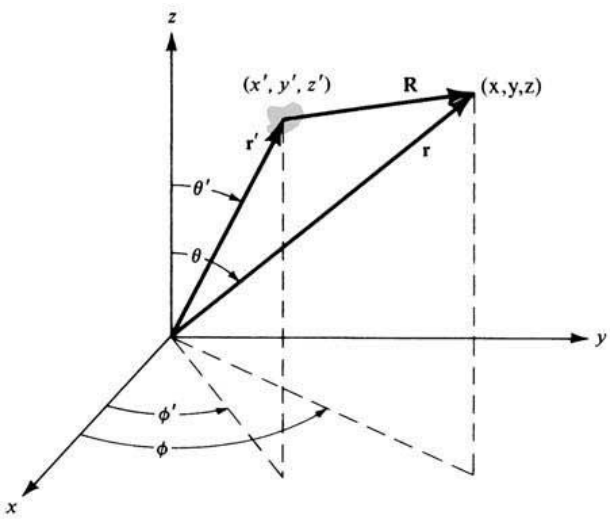

Figure 4-59 Coordinate system for far field calculation

The radiated far filed can be found using the far field approximations.

The far field approximations are

$$\frac{e^{-jk|r-r'|}}{4\pi|r-r'|} = \frac{e^{-jkr}}{4\pi r} \text{and } \nabla = -\text{jk} \qquad 4\text{-}47$$

Where $k = \text{k}\hat{\text{r}}$

The magnetic vector potential is

$$A(r) = \frac{\varepsilon e^{-jkr}}{4\pi r} F(\theta, \varphi) \qquad 4\text{-}48$$

Electric vector potential is given by

$$A_m(r) = \frac{\varepsilon e^{-jkr}}{4\pi r} F_m(\theta, \varphi) \qquad 4\text{-}49$$

$F(\theta, \varphi)$and$F_m(\theta, \varphi)$are called the radiation vectors.

The radiation vectors in discrete form are given by

$$F(\theta, \varphi) = \sum_{x=1}^{Nx} \sum_{y=1}^{Ny} \sum_{z=1}^{Nz} J(r')\, e^{jk.r'} dV' \qquad 4\text{-}50$$

$$F_m(\theta, \varphi) = \sum_{x=1}^{Nx} \sum_{y=1}^{Ny} \sum_{z=1}^{Nz} J_m(r')\, e^{jk.r'} dV' \qquad 4\text{-}51$$

Where, j(r') - electric current

J_m(r') - magnetic current

In the far field, j=jm=0. Using the approximation $\nabla = -\mathrm{jk} = -\mathrm{jk}\hat{r}$ and the relationship $\frac{k}{\varepsilon} = \omega\eta$

The radiated fields by considering only electric current are,

$$E = -\mathrm{jk}\eta \frac{e^{-jkr}}{4\pi r} (\hat{r} \times F) \times \hat{r} \qquad 4\text{-}52$$

$$H = -\mathrm{jk} \frac{e^{-jkr}}{4\pi r} \hat{r} \times F \qquad 4\text{-}53$$

The radiated E and H fields including electric and magnetic current are found as follows

$$E = -\mathrm{j}\omega[\hat{r} \times (A \times \hat{r}) - \eta\hat{r} \times A_m] = -\mathrm{jk} \frac{e^{-jkr}}{4\pi r} \hat{r} \times [\eta F \times \hat{r} - F_m] \qquad 4\text{-}54$$

$$H = -\frac{\mathrm{j}\omega}{\eta} [\eta\hat{r} \times (A_m \times \hat{r}) + \hat{r} \times A] = -\frac{\mathrm{jk}}{\eta} \frac{e^{-jkr}}{4\pi r} \hat{r} \times [\eta F + F_m \times \hat{r}] \qquad 4\text{-}55$$

Where,

$\hat{r} \times (\mathrm{F} \times \hat{\mathrm{r}}) = \hat{\theta} F_\theta + \hat{\varphi} F_\varphi$ and $\hat{r} \times \mathrm{F} = \hat{\varphi} F_\theta - \hat{\theta} F_\varphi$ and similarly for F_m The polar components can then be found as

$$E = -\mathrm{jk}\frac{\mathrm{e}^{-jkr}}{4\pi \mathrm{r}}\left[\hat{\theta}\left(\eta F_\theta + F_{m\varphi}\right) + \hat{\varphi}\left(\eta F_\varphi - F_{m\theta}\right)\right] \qquad 4\text{-}56$$

$$H = -\mathrm{jk}\frac{\mathrm{e}^{-jkr}}{4\pi \mathrm{r}}\left[-\hat{\theta}\left(\eta F_\varphi - F_{m\theta}\right) + \hat{\varphi}\left(\eta F_\theta + F_{m\varphi}\right)\right] \qquad 4\text{-}57$$

4.5.2 Radiation from monopole

To validate the procedure, the current source above a ground, discussed before is again considered here to be the device under test. The equivalent source is calculated by using the 2D cross-correlation method. Figure 4-60 (b) shows the calculated equivalent current of the structure shown in Figure 4-60(a) using the 2D cross-correlation method. The equivalent source corresponds to the current source Jz at the center of the ground plane. This equivalent source is the same as that of the equivalent source obtained using inverse TLM method.

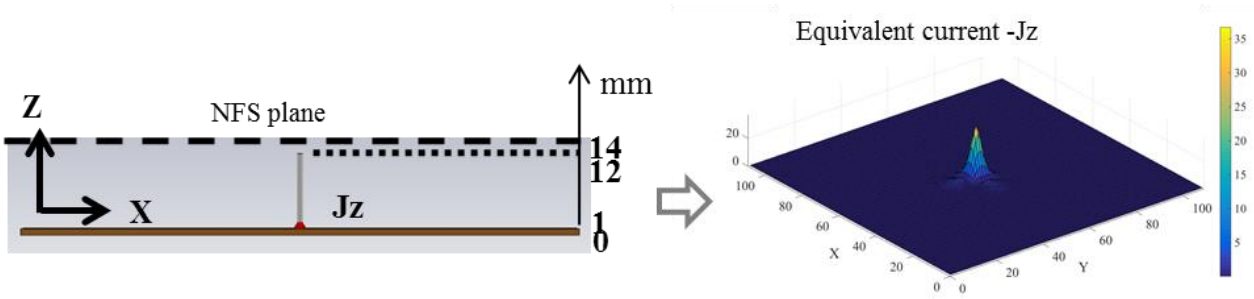

(a) (b)

Figure 4-60 Current source with ground plane (a) simulated current source (b) calculated equivalent current using 2D cross-correlation method

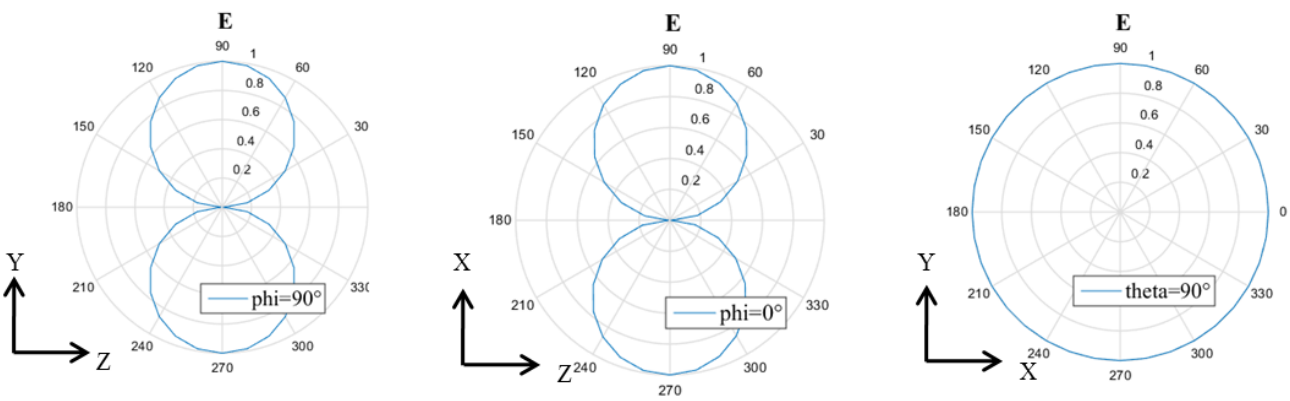

Figure 4-61 Calculated E field of the monopole at 1m

The radiated E field at 1m is plotted in Figure 4-61. The E field is normalized in each plane. The maximum radiation is in the XY plane. The radiation pattern is same as that of a dipole oriented

along z-direction. The pattern is omni directional and it has a shape of a figure of eight in the YZ and XZ plane.

4.5.3 Predicted field of bend monopole

Figure 4-62shows the electric fields radiated from the PCB at 1m away from the PCB, calculated using 4-52. The equivalent source is considered as a combination of only Jx and Jy. The E field radiated by this PCB at 1m is simulated with CST and is compared with the reconstructed field. The E fields at each plane are normalized with respect to its maximum value in that plane. The shape of the reconstructed field is in an acceptable agreement with the reference or the simulated field. The 10º difference in the XZ plane due to the fact that the amplitude of the reconstructed sources is not the same as that of the original source.

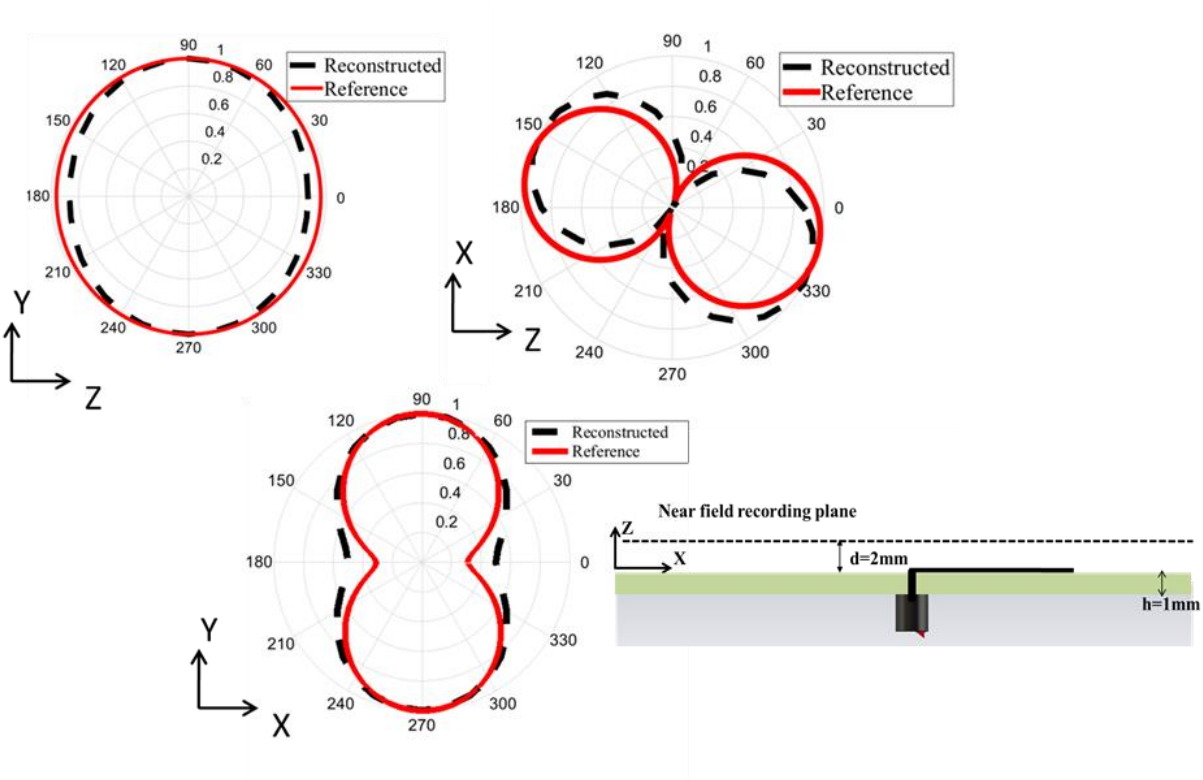

Figure 4-62 Comparison of the calculated magnetic field with the simulated magnetic field of a bent monopole

4.6 Conclusions

The inverse TLM method can be used to reconstruct the fields at any plane above the source and below the near field scanning plane. In the case of the known distribution of sources, this method can be used to identify the sources. In the case of the voltage sources, the source can be found from the maximum value of tee the normal component of the electric field. Ann alternating normal component of electric field is found only for a tangential voltage source. The orientation of the

voltage source is determined from the direction of alternation of the normal E field. In the case of the normal voltage source, the normal component of E will have a peak at the position of the source. The current source is determined from the magnetic field components.

In the case of the normal current, the equivalent current can be calculated by calculating the circulation of the magnetic field. But, in the case of the tangential current sources, the circulating current is not found in the reconstructed plane, because of the fact that the plane is tangential to the current source. Even though we will be able to identify the source positions from the near field scan data and the reconstructed fields, we need an algorithm which represents the radiations from devise under test with an equivalent source. In order to calculate the equivalent current in complex PCBs, it needs to have both the tangential components of the magnetic field.

So, the equivalent current can only be found accurately for a vertical current source in an arbitrary PCB, where there is no knowledge about the sources. The newly developed cross-correlation method could overcome this limitation of the inverse propagation method. The cross-correlation method is applied directly to the near field scan data. The method is not applied to the inverse propagated fields because the electric and magnetic fields become wider than the original filed after inverse propagation. The spatial resolution of the reconstruction depends on the mesh size and the wavelength. So, when a number of spatial points in the near field scan data increases, the more accurately we reconstruct the sources.

The developed cross-correlation method is validated for ideal current sources. It is found that the procedure could accurately determine the position and orientation of the source. The method is also validated for multiple current sources. The window size of the standard function is optimized to a one-dimensional window of size 9mm. The accuracy of the equivalent source decreases when the window size of the standard function increases.

The prediction of the far field requires both the magnitude and phase of the equivalent current. Even though the source position and orientation are correctly identified, it needs to have the accurate information about the exact amplitude and phase of the source in order to calculate the radiated far field.

4.7 References

[1] D. Cassereau and M. Fink, "Time-Reversal of Ultrasonic Fields—Part III: Theory of the Closed Time-Reversal Cavity," *IEEE Trans. Ultrason. Ferroelectr. Freq. Control*, vol. 39, no. 5, pp. 579–592, 1992.

[2] M. Fink, "Time Reversal of Ultrasonic Fields—Part I: Basic Principles," *IEEE Trans. Ultrason. Ferroelectr. Freq. Control*, vol. 39, no. 5, pp. 555–566, Sep. 1992.

[3] M. Fink and C. Prada, "Acoustic time-reversal mirrors," *Inverse Probl.*, vol. 17, no. 1, p. R1, 2001.

[4] M. Fink, "Time-reversal acoustics Time-Reversal Acoustics," 2008.

[5] R. Carminati, R. Pierrat, J. de Rosny, and M. Fink, "Theory of the time reversal cavity for electromagnetic fields.," *Opt. Lett.*, vol. 32, no. 21, pp. 3107–3109, Nov. 2007.

[6] N. Bleistein and J. K. Cohen, "Nonuniqueness in the inverse source problem in acoustics and electromagnetics," *J. Math. Phys.*, vol. 18, no. May 2016, pp. 194–201, 1977.

[7] J. De Rosny, G. Lerosey, and M. Fink, "Theory of electromagnetic time-reversal mirrors," *IEEE Trans. Antennas Propag.*, vol. 58, no. 10, pp. 3139–3149, Oct. 2010.

[8] G. Lerosey, J. De Rosny, A. Tourin, A. Derode, G. Montaldo, and M. Fink, "Time reversal of electromagnetic waves," *Phys. Rev. Lett.*, vol. 92, no. 19, pp. 193904–1, 2004.

[9] T. Strohmer, M. Emami, J. Hansen, G. Papanicolaou, and a. J. Paulraj, "Application of time-reversal with MMSE equalizer to UWB communications," *IEEE Glob. Telecommun. Conf. 2004. GLOBECOM '04.*, vol. 5, pp. 3123–3127, 2004.

[10] P. Kosmas and C. M. Rappaport, "Time reversal with the FDTD method for microwave breast cancer detection," *Microw. Theory Tech. IEEE Trans.*, vol. 53, no. 7, pp. 2317–2323, 2005.

[11] a B. Ruffin *et al.*, "Time reversal terahertz imaging," *IEEE J. Quantum Electron.*, vol. 38, no. 8, pp. 1110–1119, 2002.

[12] G. Micolau, M. Saillard, and P. Borderies, "DORT method as applied to ultrawideband signals for detection of buried objects," *IEEE Trans. Geosci. Remote Sens.*, vol. 41, no. 8, pp. 1813–1820, 2003.

[13] P. P. M. So and J. R. Wolfgang, "NUMERICAL MICROWAVE SYNTHESIS BY

INVERSION OF RHE PROCESS," *21st Eur. Microw. Conf. 1991*, pp. 1273–1277, Oct. 1991.

[14] R. D. P. Moreira, S. Member, and L. R. a X. De Menezes, "Direct Synthesis of Microwave Filters Using Inverse Scattering Transmission-Line Matrix Method," *IEEE Trans. Microw. Theory Tech.*, vol. 48, no. 12, pp. 2271–2276, 2000.

[15] I. Scott, A. Vukovic, and P. Sewell, "Reducing the computational requirements of time-reversal device optimizations," *Int. J. Numer. Model. Electron. Networks, Devices Fields*, vol. 23, no. 6, pp. 458–469, Nov. 2010.

[16] L. de Menezes, "New developments in the inverse scattering TLM (Transmission Line Matrix) method," in *SBMO/IEEE MTT-S International Microwave and Optoelectronics Conference IMOC*, 2001, vol. 1, pp. 403–406.

[17] G. Lerosey, J. de Rosny, A. Tourin, and M. Fink, "Focusing Beyond the Diffraction Limit with Far-Field Time Reversal," *Science (80-.).*, vol. 315, no. 5815, pp. 1120–1122, Feb. 2007.

[18] A. Ungureanu, Y. Fu, T. P. Vuong, and F. Ndagijimana, "Electromagnetic source synthesis by reversed-TLM method," *IEEE MTT-S Int. Microw. Symp. Dig.*, 2011.

[19] M. Fink, J. de Rosny, G. Lerosey, and A. Tourin, "Time-reversed waves and super-resolution," *Comptes Rendus Physique*, vol. 10, no. 5. Elsevier Masson, pp. 447–463, 01-Jun-2009.

[20] P. Saguet and E. Pic, "Utilisation d'un nouveau type de noeud dans la mÃ©thode TLM en 3 dimensions (Usage of a new type of node in the 3D TLM method)," *Electronics Letters*, vol. 18, no. 11. pp. 478–480, 1982.

[21] W. J. R. Hoefer, "The Transmission-Line Matrix Method--Theory and Applications," *IEEE Trans. Microw. Theory Tech.*, vol. 33, no. 10, pp. 882–893, Oct. 1985.

[22] P. B. Johns and R. L. Beurle, "Numerical solution of 2-dimensional scattering problems using a transmission-line matrix," *Proc. Inst. Electr. Eng.*, vol. 118, no. 9, p. 1203, 1971.

[23] M. Fink *et al.*, "Time-reversed acoustics," *Reports Prog. Phys.*, vol. 63, no. 12, pp. 1933–1995, Dec. 2000.

[24] R. Snieder, "Time-reversal invariance and the relation between wave chaos and classical chaos," *Imaging Complex Media with Acoust. Seism. Waves*, vol. 84, no. 1, pp. 1–15, 2002.

[25] W. J. R. Hoefer, "Computational Time Reversal-A Frontier in Electromagnetic Structure Synthesis and Design," *IEEE Trans. Microw. Theory Tech.*, vol. 63, no. 1, pp. 3–10, 2015.

[26] A. Ungureanu, T. P. Vuong, and F. Ndagijimana, “Electromagnetic point source reconstruction by reversed-TLM method,” *Appl. Comput. Electromagn. Soc. J.*, vol. 26, no. 9, pp. 754–759, 2011.

[27] M. Forest and W. J. R. Hoefer, “Novel synthesis technique for conducting scatterers using TLM time reversal,” *IEEE Trans. Microw. Theory Tech.*, vol. 43, no. 6, pp. 1371–1378, 1995.

[28] Z. D. Chen and M. M. Ney, “On the relationship between the time-domain and frequency-domain TLM methods,” *IEEE Antennas Wirel. Propag. Lett.*, vol. 7, pp. 46–49, 2008.

[29] H. Jin and R. Vahldieck, “The frequency-domain transmission line matrix method???a new concept,” *IEEE Trans. Microw. Theory Tech.*, vol. 40, no. 12, pp. 2207–2218, 1992.

[30] R. F. Harrington, *Time-harmonic electromagnetic fields*. IEEE Press, 2001.

[31] S. J. Orfanidis, *Electromagnetic Waves and Antennas Electromagnetic Waves and Antennas*. 2016.

5. Conclusions and perspectives

In this thesis, we have designed and validated magnetic probes based on microstrip line, CPW line, and printed shielded probes. The single loop probe is found to have higher selectivity than multiple loop probes and hence it has the highest frequency band of operation. The transmission connected to the loop has a significant influence on the performance of the probe. The voltage at the output of the probe contains not only the voltage due to the magnetic field but also, the common mode voltages induced by the electric field. As the length of the transmission line increases, the common mode voltages increases and the highest frequency of operation of the probe decreases. The shielded magnetic probes reduce the voltage due to the electric field and increase the frequency band of operation. For the frequency range between 1MHz-1GHz, the shielded magnetic probes with the stripline configuration are found to be the better choice than the conventional probes. It is necessary to use the shielded probes for frequencies above 100 MHz. As the aperture size of the loop is 800 µm x 800 µm the sensitivity of the probe is very poor and is not able to detect the magnetic field at all positions without an amplifier. The use of an external amplifier has increased the sensitivity of the probe. With an external amplifier of 37 dB, the probe could measure the magnetic field at all frequencies from 10 MHz-1GHz. It is found that the amplifier should not be placed very close to the probe because it causes noise at the output due to the probe.

The further enhancement of the spatial resolution requires having active probe with multistage amplifiers. The fabrication of the passive and active probes with spatial resolution of the order of 100µm is under progress. The apertures of the loop under fabrication are 500µm, 400µm and 200µm. The shielding of the probe and the impedance of the transmission line are also critical parameters, which determine the accuracy of the scanned profile. The fabrication of the both active and passive probes with impedance matching technique at the point of connection to the SMA is under progress. Layouts of some passive probes under fabrication are shown in Figure 5-1.

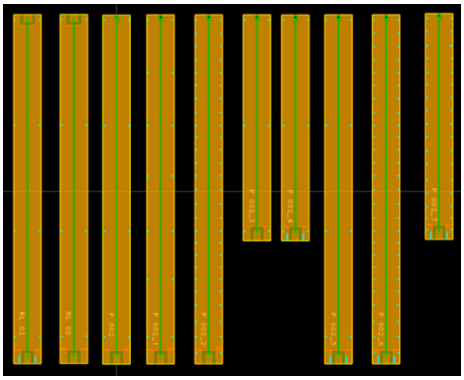

Figure 5-1 Layout of some passive probes under fabrication (view from ADS momentum)

The inverse TLM method can be used to reconstruct the fields at any plane above the source and below the near field scanning plane. With this method, the equivalent current could only be found accurately for a vertical current source in an arbitrary PCB, where there is no knowledge about the sources. The newly developed cross-correlation method could overcome this limitation of the inverse propagation method. The cross-correlation method is applied directly to the near field scan data. The method is not applied to the inverse propagated fields because the electric and magnetic fields become wider than the original filed after inverse propagation. The spatial resolution of the reconstruction depends on the mesh size and the wavelength. So, when a number of spatial points in the near field scan data increases, the more accurately we reconstruct the sources. This illustrates the need of having a probe with high spatial resolution.

The developed cross-correlation method is validated for ideal current sources. It is found that the procedure could accurately determine the position and orientation of the source. The method is also validated for multiple current sources. The window size of the standard function is optimized to a one-dimensional window of size 9mm. The accuracy of the equivalent source decreases when the window size of the standard function increases.

The final objective of the developed source reconstruction methods is to apply to real PCBs. In order to validate the procedure experimentally, we have designed few demonstrators. Two of them are shown in Figure 5-2. The demonstrator in Figure 5-2 (a) is a loop above a metallic ground plane and is fed by a coaxial cable at one end and terminated by 50 Ohm impedance at the other end. The 2D cross-correlation will not be able to distinguish between the positive and negative currents. So, the equivalent current source for this PCB may appear as two vertical dipoles with same phase (Jz) as one horizontal dipole. As the phases of the sources are the same, the current due to the vertical dipoles (+Jz and - Jz) will not be able to cancel in the calculation of the far field, which will lead to some errors in the predicted radiated field.

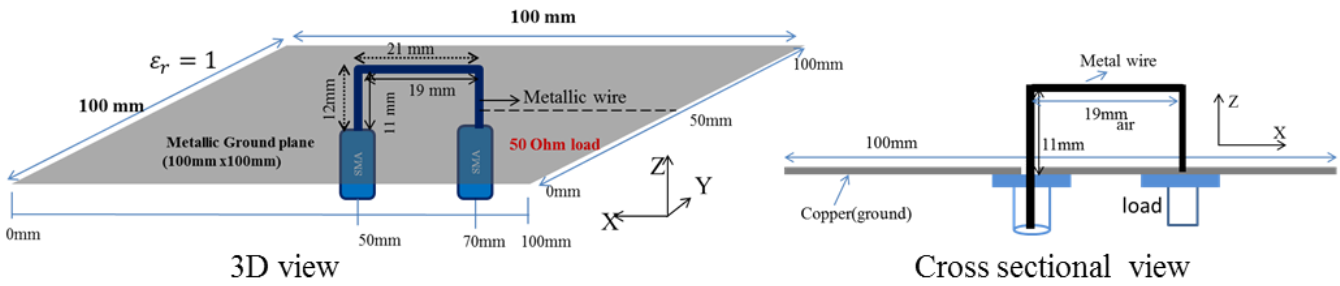

(a)

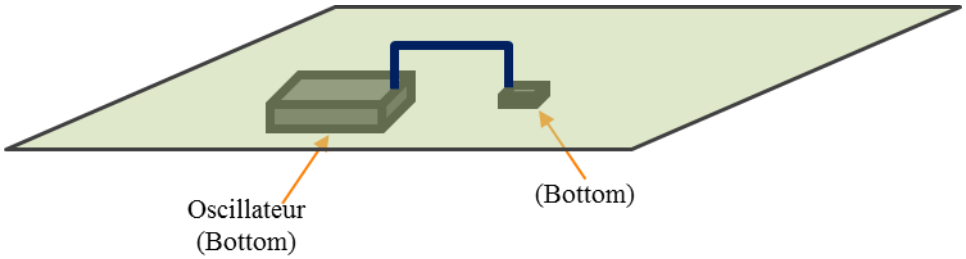

(b)

Figure 5-2 Validation circuits under fabrication 3D view (a) loop above a ground plane (b) PCB with an Oscillator

In reality, the PCBs are assumed to have more current loops. In order to have an accurate equivalent model of these loops, it is necessary to represent them in terms of the magnetic dipole current. So, modifying the developed method to represent the sources in terms of magnetic dipole current can accurately predict the behavior of these demonstrators. After validating the method for the demonstrator in Figure 5-2(a), we plan to apply to more complex PCBs containing oscillator circuits as shown in Figure 5-2 (b).

APPENDIX

Design equations of the transmission lines used in this thesis are provided below

A. CPW transmission line

Closed form expressions of effective dielectric constant and characteristic impedancefor zero strip thickness (t=0) are given below according to [1]

thickness (t=0) are given below according to [1]

$$\varepsilon_{eff} = 1 + \frac{\varepsilon_r - 1}{2}\frac{K(k')K(k_1)}{K(k)K(k_1{}')} \qquad 5\text{-}1$$

And

$$Z_0 = \frac{30\pi}{\sqrt{\varepsilon_{eff}}}\frac{K(k')}{K(k)} \qquad 5\text{-}2$$

where

$$k = \frac{a}{b}\ , \qquad k' = \sqrt{1-k^2}\ , \qquad k_1 = \frac{sinh\frac{\pi a}{2h}}{sinh\frac{\pi b}{2h}}\ , \qquad k_1{}' = \sqrt{1-k_1{}^2}$$

K represents the complete integration of the first kind, whose values can be determined from an integral or tabulated table. $\frac{\mathrm{K(k)}}{K(k')}$ can also be approximated by [2]

$$\frac{K(k)}{K(k')} = \begin{cases} \dfrac{\pi}{ln\left(2\frac{1+\sqrt{k'}}{1-\sqrt{k'}}\right)}, & 0 \le k \le 0.707 \\ \dfrac{1}{\pi}ln\left(2\dfrac{1+\sqrt{k}}{1+\sqrt{k}}\right), & 0.707 \le k \le 1 \end{cases} \qquad 5\text{-}3$$

The effective dielectric constant and the characteristic impedance of the CPW considering the thickness t of the strip (t>0) is calculated as follows [3].

$$\varepsilon_{eff}(t) = \varepsilon_{eff} - \frac{0.7\left(\varepsilon_{eff} - 1\right)\frac{t}{b-a}}{\frac{K(k)}{K(k')} + 0.7\frac{t}{b-a}} \qquad 5\text{-}4$$

And

$$Z_0 = \frac{30\pi}{\sqrt{\varepsilon_{eff}(t)}}\frac{K(k'_e)}{K(k_e)} \qquad 5\text{-}5$$

Where,

$$k_e = \frac{S_e}{S_e + 2W_e}, \qquad k_e{}' = \sqrt{1 - k_e{}^2}$$

$$S_e = 2a + \Delta \quad , \qquad W_e = b - a - \Delta \quad , \qquad \Delta = \left[1 + ln\left(\frac{8\pi a}{t}\right)\right]$$

B. Grounded CPW transmission line

The effective dielectric constant and characteristic impedance for the conductor-backed CPW is calculated as follows, for zero strip thickness (t=0)

$$\varepsilon_{eff} = \frac{1 + \varepsilon_r \frac{K(k')K(k_1)}{K(k)K(k_1{}')}}{1 + \frac{K(k')K(k_1)}{K(k)K(k_1{}')}} \qquad 5\text{-}6$$

And

$$Z_0 = \frac{60\pi}{\sqrt{\varepsilon_{eff}}}\frac{1}{\frac{K(k)}{K(k')} + \frac{K(k_1)}{K(k_1{}')}} \qquad 5\text{-}7$$

C. Stripline

Its characteristic impedance for a zero thickness strip is determined by the following conformal mapping formulas[4]

$$Z_0 = \frac{30\pi}{\sqrt{\varepsilon_r}}\frac{K(k')}{K(k)} \qquad 5\text{-}8$$

Where,

$$k = tanh\frac{\pi W_s}{4a}, \qquad k' = \sqrt{1 - k^2}$$

For a finite strip thickness t, the characteristic impedance is calculated as follows[5]

$$Z_0 = \frac{30}{\sqrt{\epsilon_r}} ln\left\{1 + \frac{4}{\pi}\frac{2a-t}{W_e}\left[\frac{8}{\pi}\frac{2a-t}{W_e} + \sqrt{\left(\frac{8}{\pi}\frac{2a-t}{W_e}\right) + 6.27}\right]\right\} \qquad 5\text{-}9$$

Where,

$$\frac{W_e}{2a-t} = \frac{W_s}{2a-t} + \frac{\Delta W_s}{2a-t}$$

$$\frac{\Delta W_s}{2a-t} = \frac{x}{\pi(1-x)}\left\{1 - \frac{1}{2} ln\left[\left(\frac{x}{2-x}\right)^2 + \left(\frac{0.0796}{\frac{W_s}{2a} + 1.1x}\right)^m\right]\right\}$$

$m = \frac{2}{1+\frac{2x}{3(1-x)}}$, $\qquad x = \frac{t}{2a}$

References

[1] G. Ghione and C. Naldi, “Analytical formulas for coplanar lines in hybrid and monolithic MICs,” *Electron. Lett.*, vol. 20, no. 4, p. 179, 1984.

[2] W. Hilberg, “From Approximations to Exact Relations for Characteristic Impedances,” *IEEE Trans. Microw. Theory Tech.*, vol. 17, no. 5, pp. 259–265, May 1969.

[3] C. Nguyen, “Introduction,” in *Analysis Methods for RF, Microwave, and Millimeter-Wave Planar Transmission Line Structures*, New York, USA: John Wiley & Sons, Inc., pp. 1–11.

[4] S. B. Cohn, “Problems in strip transmission lines,” *IRE Trans. Microw. Theory Tech.*, vol. MTT-3, no. 2, pp. 119–126, Mar. 1955.

[5] H. A. Wheeler, “Transmission-Line Properties of a Strip Line Between Parallel Planes,” *IEEE Trans. Microw. Theory Tech.*, vol. 26, no. 11, pp. 866–876, Nov. 1978.

List of publications

International conferences

1. **Nimisha Sivaraman** , Fabien Ndagijimana, Moncef Kadi, Zouheir Riah " Broad band PCB probes for near field measurements" EMC Europe, France, September 2017

2. **Nimisha Sivaraman**, Kassem Jomaa, Fabien Ndagijimana, "Three Dimensional Scanning System for Near-field Measurements" European Conference on antennas and propagation(EuCAP) , France, March 2017.

3. **Sivaraman Nimisha,** Ndagijimana Fabien,"A new approach to Identification and localization of current sources in a PCB," Applied Electro-Magnetic Conference, India, December 2017. (Accepted)

4. Sarah Jacob, **S. Nimisha,** P.V. Anila, P.Mohanan,"UWB antenna with reconfigurable band-notched characteristics using ideal switches," IEEE international microwave and RF conference, India, Feb. 2014.

5. Dinesh R, Vinod VKT, Anila PV, Vivek R Kurup, **Nimisha S** and P. Mohanan, "CPW Fed Dual Band Slot Antenna for WLAN Applications" International conference on Information science, India, 2014.

National conference

1. **N. Sivaraman,** K. Jomaa, Y. Fu, F.Ndagijimana, "sonde 3 axes pour la mesure de champs proches, JNM", France, May 2017.

2. **N. Sivaraman,** F. Ndagijimana , " Shielded magnetic probes with high electric field suppression", GDR ondes, France, 2015.

Workshops

1. **Sivaraman Nimisha,** Ndagijimana Fabien, Riah Zouheir, Kadi Moncef, "Methods for extrapolation of near field meaureemnts", EMC Europe, France, September 2017.

2. **Sivaraman Nimisha,** Ndagijimana Fabien, "Reverse method for source reconstruction from near field measurements", GDR ondes", France2017.

Résumé

Au fur et à mesure que le nombre de composants augmente, il existe une forte demande pour identifier les sources de rayonnement pour la prédiction de la compatibilité électromagnétique des circuits électroniques. Le balayage d'une sonde à proximité du circuit est une méthode générale d'identification des sources rayonnantes dans une PCB. La première partie de la thèse consiste à concevoir et à caractériser des sondes magnétiques à haute sensibilité et à haute résolution spatiale. Les sondes conventionnelles basées sur la ligne micro ruban et la configuration coplanaire sont étudiées. À mesure que la longueur de la ligne de transmission connectée à la sonde augmente, le bruit sur le signal de sortie augmente en raison de tensions de mode commun induites par le champ électrique. Afin de supprimer cette tension induite par le champ électrique, une sonde magnétique blindée est conçue et fabriquée à l'aide d'une technologie de circuit imprimé à faible coût (PCB). La performance de la sonde passive est validée dans la bande 1MHz - 1GHz. La sonde blindée est fabriquée sur un substrat FR4 d'une épaisseur de 0,8 mm et se compose de 3 couches avec le signal dans la couche intermédiaire et les couches supérieure et inférieure dédiées aux plans de masse. La taille d'ouverture de la boucle est de 800 µm x 800 µm, avec une résolution spatiale attendue de 400 µm. La haute sensibilité de la sonde est obtenue en intégrant un amplificateur à faible bruit à la sortie de la sonde, ce qui en fait une sonde active. La performance de la sonde blindée avec différentes longueurs de lignes de transmission est faite pour étudier. Une sonde à trois axes capable de mesurer les trois composantes du champ magnétique est également conçue et validée par un balayage en champs proches au-dessus d'une structure standard plan de masse.

Dans la deuxième partie, la méthode de la matrice de la ligne de transmission inverse (Inv-TLM) est utilisée, pour reconstruire la distribution source à partir des champs proches (NFS) mesurés au-dessus d'un plan sur la carte PCB. Même si, la résolution de la reconstruction dépend de la longueur d'onde et des paramètres du maillage, la propagation inverse augmente la largeur de l'onde reconstruite. Comme cette méthode corresponde à un problème « mal posé» et entraîne des solutions multiples, nous avons développé une nouvelle méthode basée sur la corrélation croisée bidimensionnelle, qui représente les données de balayage en champ proche sous forme de de dipôles équivalents. Avec cette nouvelle méthode, nous avions pu identifier et de localiser les sources actuelles dans le PCB et est représenté avec des sources équivalentes. La méthode est validée pour les sources avec des orientations différentes. Les données simulées des champs proches utilisant le logiciel commercial CST sont utilisées pour valider les deux méthodes. Le champ lointain prédit à partir de ces sources équivalentes est comparé aux champs simulés.